

# **GNSS-based Global Ionospheric Maps: real-time combination, time resolution and applications on space weather monitoring**



**Qi Liu** 

Supervisor: Prof. Dr. M. Hernández-Pajares 

Aerospace Science and Technology Doctoral Program  
Universitat Politècnica de Catalunya

Thesis submitted as a collection of published articles

April, 2022



## **Acknowledgements**

On 11 October 2019 when I took the flight from my hometown to Barcelona, I was young and naive. I am deeply grateful to thank my advisor Manuel Hernández-Pajares who provide invaluable advice, continuous support and inexhaustible patience. His enthusiasm and wisdom about scientific research and life have inspired me a lot.

I would like to thank the help from colleagues and visitors of the UPC-IonSAT research group. When I first come here, I am not familiar with almost everything. Thanks to the kind help from Haixia, Heng and Jiaojiao, I gradually got adapted to research and daily life here. The short talk and discussion with Haixia after work lead to thinking in multi-perspectives. And the discussion about research with Heng has helped me a lot. The kind suggestions and concerns from Enric are very helpful and thoughtful. I would also like to express my gratitude to David, Alberto and Germán for their kind advice and help. The discussion with Andreas and Gabriel is also inspiring.

The kind help from IGS real-time working group, IGS ionosphere working group and researchers from MoNEWIC project is highly appreciated. This thesis is partially supported by TEC4SpaW, MoNEWIC and PITHIA-NRF projects.

I would like to offer my special thanks to the financial support from China Scholarship Council (CSC). I would also like to extend my sincere thanks to my previous advisor Xingliang Huo who kindly provides kind suggestions and supports my application for CSC. And also many thanks to Yunbin Yuan, Xiaohua Xu, Zishen Li and Ningbo Wang for their kind recommendation and help.

Last but not least, I would like to thank my family and friends for their support and companionship.



## Abstract

**UNESCO codes:** 120321, 220209, 250118

The research of this paper-based dissertation is focused on the Global Ionospheric Maps (GIMs) based on Global Navigation Satellite System (GNSS) including real-time combination, validation, time resolution and applications. The novelty of these works can be summarized as follows:

The first contribution is to connect GIM assessment methods in post-processing and real-time mode including Jason-altimeter Vertical Total Electron Content (VTEC) assessment, GNSS differences of Slant Total Electron Content (dSTEC) assessment and real-time dSTEC (RT-dSTEC) assessment. With the RT-dSTEC assessment, we can assess the accuracy and calculate the weight of different real-time GIMs for combination in real-time mode. The Jason-altimeter VTEC assessment and dSTEC assessment can be used for evaluating GIMs over oceans and continental regions, respectively. In addition, the accurate GIMs shown in the GIM assessment methods can be regarded as reliable representations of global VTEC.

The second contribution is to apply the RT-dSTEC assessment in real-time mode for the combination of different International GNSS Service (IGS) real-time GIMs. The IGS combined real-time GIM is generated to provide robust ionospheric corrections for real-time GNSS positioning and reliable global VTEC distribution for earth observations. The current status of IGS real-time GIMs from different centers is summarized and compared. The Jason-altimeter VTEC assessment and dSTEC assessment in post-processing mode are used for the validation of IGS real-time GIMs. The sensibility of real-time weighting technique by RT-dSTEC assessment is also verified.

The third contribution is to investigate the influence of temporal resolution on the performance of GIMs. The variation of ionosphere is typically assumed as linear between two consecutive GIM TEC maps in a sun-fixed reference frame for up to few hours. However, the variation of ionospheric TEC is irregular due to the occurrence of space weather events. One and a half solar cycle of the IGS GIM with higher time resolution and accuracy (the UPC-IonSAT Quarter-of-an-hour time resolution Rapid GIM, UQRG) has been taken as a baseline to downsample them to all possible sub-daily temporal resolutions. The performance

of the resulting GIMs has been evaluated taking into account the geographical position, solar and geomagnetic activity by Jason-altimeter VTEC assessment and dSTEC assessment.

The fourth contribution is to propose a new way of estimating the spatial and temporal components of the VTEC gradient. The determination of ionospheric perturbation degrees can be helpful for guaranteeing the safety level of Satellite-Based Augmentation System (SBAS) and Ground-Based Augmentation System (GBAS) services. In order to estimate the spatial and temporal components of the VTEC gradient on a global scale, the accurate UQRG is selected. The VTEC gradient indices derived from UQRG GIMs (VgUG) allow users to obtain full (non-relative) values of TEC spatial gradients and temporal variations separately. The Regional VTEC spatial Gradient indices, based on UQRG (RVGU) and the Regional Ionospheric Disturbance index based on UQRG (RIDU), are proposed to estimate the regional ionospheric perturbation degree over selected regions. In addition, the spatial and temporal components of VTEC gradient at grid points of UQRG on a global scale are also introduced.

The fifth contribution is to define a new ionospheric storm scale. The ionospheric response to high geomagnetic activity, ionospheric storm, can enlarge GNSS positioning errors by the increase of ionospheric electron density and disable high-frequency communications by the decrease of ionospheric electron density. To characterize the ionospheric state on a global scale, reliable global VTEC distribution is essential. According to previous studies, UQRG is one of the most accurate GIM. In this regard, the new Ionospheric storm Scale based on UQRG, IsUG, is proposed.

## Resum

**Codis UNESCO:** 120321, 220209, 250118

La investigación de esta tesis doctoral se centra en los Mapas Ionosféricos Globales (GIMs) basados en el Sistema Global de Navegación por Satélite (GNSS), incluyendo la combinación en tiempo real, la validación, la resolución temporal y su aplicación. La novedad de los trabajos presentados puede resumirse como sigue:

La primera contribución consiste en conectar los métodos de evaluación de los GIM en modo de posprocesamiento y en tiempo real, incluyendo la evaluación VTEC gracias a las medidas de los altímetros Jason, la evaluación del contenido total de electrones diferencial (dSTEC) y la evaluación dSTEC en tiempo real (RT-dSTEC). Con la evaluación RT-dSTEC, podemos evaluar la precisión y calcular el peso de diferentes GIM en tiempo real para su combinación también en tiempo real. La evaluación VTEC del altímetro Jason y la evaluación dSTEC pueden utilizarse para evaluar los GIM sobre los océanos y las regiones continentales, respectivamente. Además, los GIM precisos mostrados en los métodos de evaluación de GIM pueden considerarse como representaciones fiables del contenido total de electrones vertical global (VTEC).

La segunda contribución consiste en aplicar la evaluación RT-dSTEC en tiempo real para la combinación de diferentes GIM del Servicio Internacional GNSS (IGS), todo ello en tiempo real. El GIM IGS combinado resultante proporciona correcciones ionosféricas robustas para el posicionamiento GNSS en tiempo real y una distribución global de VTEC fiable para las observaciones terrestres. Se resume y compara el estado actual de los GIM en tiempo real de diferentes centros IGS. La evaluación de VTEC respecto de los altímetros Jason y la evaluación de dSTEC en modo de posprocesamiento también se utilizan para la validación de los GIM en tiempo real del IGS. Y se verifica la sensibilidad de la técnica de ponderación en tiempo real mediante la evaluación RT-dSTEC.

La tercera contribución consiste en proponer una nueva forma de estimar las componentes espaciales y temporales del gradiente VTEC. La determinación de los grados de perturbación ionosférica puede ser útil para garantizar el nivel de seguridad de los servicios del Sistema de Aumento Basado en Satélites (SBAS) y del Sistema de Aumento Basado en Tierra (GBAS). Para estimar los componentes espaciales y temporales del gradiente de VTEC a escala global,

se selecciona el GIM UQRG debido a su exactitud y resolución temporal. Los índices de gradiente VTEC derivados de los GIM de UQRG (VgUG) permiten a los usuarios obtener valores completos (no relativos) de gradientes espaciales de VTEC y de las variaciones temporales por separado. Los índices de gradiente espacial VTEC regional, basados en UQRG (RVGU) y el índice de perturbación ionosférica regional basado en UQRG (RIDU), se proponen para estimar el grado de perturbación ionosférica regional sobre zonas de interés. Además también se introducen los componentes espaciales y temporales del gradiente VTEC en los puntos de la cuadrícula con valores proporcionados por UQRG a escala global.

La cuarta contribución consiste en definir una nueva escala de tormentas ionosféricas. La respuesta ionosférica a la alta actividad geomagnética, la tormenta ionosférica, puede aumentar los errores de posicionamiento del GNSS por el aumento de la densidad de electrones ionosféricos e inhabilitar las comunicaciones de alta frecuencia por la disminución y en general rápida variación de la densidad de electrones ionosféricos. Para caracterizar el estado de la ionosfera a escala global, es esencial contar con una distribución global fiable de VTEC. Según estudios anteriores, el UQRG es uno de los GIM más precisos. En este sentido se propone la nueva Escala de tormentas ionosféricas basada en UQRG, IsUG.

La quinta contribución consiste en investigar la influencia de la resolución temporal en el rendimiento de los GIM. La variación de la ionosfera se asume típicamente lineal entre dos mapas GIM TEC consecutivos separados hasta algunas horas, todo ello en el marco de referencia ligado al sol. Sin embargo la variación del TEC ionosférico es irregular debido a los sucesos de meteorología espacial. Se ha tomado como referencia un ciclo solar y medio del GIM con mayor resolución temporal y precisión en IGS, el GIM Rápido de resolución temporal de un cuarto de hora de UPC-IonSAT (UQRG), para reducirlo a todas las resoluciones temporales subdiarias posibles. El rendimiento de los GIM resultantes se ha evaluado teniendo en cuenta la posición geográfica y la actividad solar y geomagnética mediante la evaluación VTEC respecto de los altímetro Jason y la evaluación dSTEC respecto de estaciones GNSS independientes.



# Contents

<b>List of Figures</b>	<b>xi</b>
<b>List of Tables</b>	<b>xiii</b>
<b>Nomenclature</b>	<b>xv</b>
<b>1 Introduction</b>	<b>1</b>
1.1 Global Navigation Satellite System . . . . .	1
1.1.1 GNSS constellations . . . . .	2
1.1.2 GNSS measurements and error sources . . . . .	4
1.2 Ionosphere . . . . .	5
1.2.1 Ionospheric error in GNSS measurements . . . . .	5
1.2.2 Ionospheric error mitigation for GNSS measurements . . . . .	7
1.3 GNSS-based global ionospheric maps . . . . .	10
1.4 Space weather effects . . . . .	11
<b>2 Summary of the work performed</b>	<b>13</b>
2.1 The relationship between GIM assessment methods in post-processing and real-time mode . . . . .	13
2.2 Real-time GIM combination and validation . . . . .	15
2.3 Temporal resolution of GIM . . . . .	18
2.4 GIM applications on space weather monitoring . . . . .	25
2.4.1 Spatial and temporal components of VTEC gradient . . . . .	26
2.4.2 Ionospheric storms . . . . .	31
<b>3 Quality Indexes</b>	<b>35</b>
3.1 Peer-reviewed Journals . . . . .	35

<b>4</b>	<b>Conclusions and future work</b>	<b>37</b>
4.1	Conclusions . . . . .	37
4.2	Future work . . . . .	38
<b>5</b>	<b>Publications</b>	<b>41</b>
	<b>Bibliography</b>	<b>97</b>

# List of Figures

1.1	GNSS segments: space segment, control segment and user segment (from NovAtel Commons (2021)). . . . .	2
1.2	orbital height and period of GNSS constellations(from Wikimedia Commons (2021)). . . . .	3
1.3	The temperature of atmosphere, solar radiation depths and the structure of the electron density of ionosphere, from Teunissen and Montenbruck (2017).	5
1.4	Space weather effects. (reproduced from ESA Commons (2021)) . . . . .	12
2.1	The 25 common real-time stations for RT-dSTEC assessment (in green color) and 50 external GNSS stations for dSTEC-GPS assessment (in red color) .	17
2.2	Data flow for the IGS combined real-time GIM . . . . .	17
2.3	Daily standard deviation of GIM VTEC versus measured Jason3-VTEC (in TECU), from December 01 of 2020 to March 01 of 2021. . . . .	20
2.4	The daily standard deviation of the discrepancy of GIM VTEC vs. measured altimeter VTEC, in TECUs, is represented versus daily mean VTEC from day 26 of 2002 to day 335 of 2019, at different latitudinal bands. . . . .	22
2.5	The daily standard deviation of the discrepancy of GIM VTEC vs. measured altimeter VTEC, in TECUs, is represented versus daily Ap index from day 26 of 2002 to day 335 of 2019, at different latitudinal bands . . . . .	23
2.6	The evolution of RVGU at Europe (40°N-70°N, 20°W-40°E) during the geomagnetic quiet period 20-25 May 2015. . . . .	27
2.7	The evolution of RVGU at Europe (40°N-70°N, 20°W-40°E) during the Halloween storm 28 October to 1 November 2003. . . . .	28
2.8	The evolution of RVGU at Europe (40°N-70°N, 20°W-40°E) during the St. Patrick's Day storm 16-20 March 2015. . . . .	29
2.9	The global map of $\nabla V_x$ , $\nabla V_y$ and $\dot{V}_{i,j}$ for a latitudinal range of $[-75^\circ, 75^\circ]$ on 18 UT of 16-17 March 2015. The magenta dashed lines represent for the geomagnetic dip angles. . . . .	30

---

2.10	The evolution of RIDU at Europe (40°N-70°N, 20°W-40°E) on 28 October 2003 when a strong X-17.0 solar flare happened. . . . .	31
2.11	The IsUG global map of 7, 8 November in 2004. . . . .	33
2.12	The IsUG global map from 14:00 to 19:00 UTC of 7 November in 2004. . .	34

# List of Tables

2.1	The brief summary of different IGS real-time GIMs . . . . .	16
2.2	The Id. of contributing IGS real-time GIMs . . . . .	18
2.3	Standard deviation of GIM-VTEC minus Jason-VTEC in Jason-altimeter VTEC assessment (last two columns), and dSTEC assessment results of real-time GIMs on January 03 (second and third column) and January 05 (fourth and fifth column) in 2021. . . . .	19
2.4	RMS errors of real-time GIMs in RT-dSTEC assessment on January 03 and January 05 in 2021. . . . .	20
2.5	The analyzed GIM temporal resolutions, derived as 24-hour divisor time intervals and multiple of the 15-minutes time resolution of the baseline GIM uqrg. . . . .	21
2.6	Standard deviation of GIM versus Jason VTEC in TECUs, from day 26 of 2002 to day 335 of 2019, at different latitudinal bands in TECUs. . . . .	24
2.7	RMS of dSTEC assessment in TECUs with 59 global distributed receivers during four days in 2015: 082, 146, 280, 330, in TECUs. . . . .	25
2.8	The definition and occurrence probability of IsUG derived from UQRG during the period 1997-2014. . . . .	32
3.1	Journal information and ranking in its category based on the IF. . . . .	36



# Nomenclature

## Acronyms / Abbreviations

BDS BeiDou Navigation Satellite System

CAS Chinese Academy of Sciences

CNES Centre National d'Etudes Spatiales

CODE Center for Orbit Determination in Europe

DCB Differential Code Bias

dSTEC differential STEC

ESA European Space Agency

EUV Extreme ultraviolet lithography

GBAS Ground-Based Augmentation System

GEO Geosynchronous Earth Orbit

GIM Global Ionospheric Map

GLONASS Globalnaja Nawigazionnaja Sputnikowaja Sistema

GNSS Global Navigation Satellite System

GPS Global Positioning System

IAAC International Associated Analysis Centers

IAAC Ionospheric Associate Analysis Center

IGS International GNSS Service

IGSO Inclined GeoSynchronous Orbit

IONEX IONosphere map EXchange

Iono-WG Ionosphere Working Group

IRI International Reference Ionosphere

IRNSS Indian Regional Navigation Satellite System

JPL Jet Propulsion Laboratory

MEO Medium Earth Orbit

NRCan Canadian Geodetic Survey of Natural Resources Canada

QZSS Quasi-Zenith Satellite System

RIDU Regional Ionospheric Disturbance index based on UQRG

RMS Root Mean Square

RT-dSTEC Real-Time dSTEC

RTS Real-time service

RTWG Real-Time Working Group

RVGU Regional VTEC spatial Gradient indices based on UQRG

SBAS Satellite-Based Augmentation System

STEC Slant Total Electron Content

TECU Total Electron Content Unit

UPC Universitat Politècnica de Catalunya

UPC Universtat Politecutenica de Barcelona

UQRG UPC Quarter-of-an-hour time resolution Rapid GIM

VTEC Vertical Total Electron Content

WHU Wuhan University



# Chapter 1

## Introduction

### 1.1 Global Navigation Satellite System

Global Navigation Satellite System (GNSS) is a generic term encompassing different navigation satellite systems. Since the first launch of experimental navigation satellite in 1978, the Global Positioning System (GPS) from the United States has been developed and modernized. Due to the great success of GPS, a number of navigation satellite systems have been separately established by Russia (Globalnaja Nawigazionnaja Sputnikowaja Sistema, GLONASS), European Union (Galileo), People's Republic of China (BeiDou Navigation Satellite System, BDS), India (Indian Regional Navigation Satellite System, IRNSS), and Japan (Quasi-Zenith Satellite System, QZSS).

As shown in Fig 1.1, GNSS is composed of space segment, control segment and user segment. The space segment is mainly about the GNSS constellations orbiting the earth and broadcasting signals with ranging and navigation message. The control segment is monitoring the status of satellites, issuing commands and uploading data by different types of globally distributed stations. And the user segment receives the GNSS signals by corresponding equipment and processes the signals (Montenbruck et al., 2017; Teunissen and Montenbruck, 2017).

The occurrence of GNSS has brought about a revolution in human society. GNSS has been widely applied to location-based services, surveying, aviation, fishership, timing, ionosphere sensing, earthquake and tsunami warning, etc (Dow et al., 2009).

In this section, the GNSS constellations, measurements and error sources are briefly summarized.

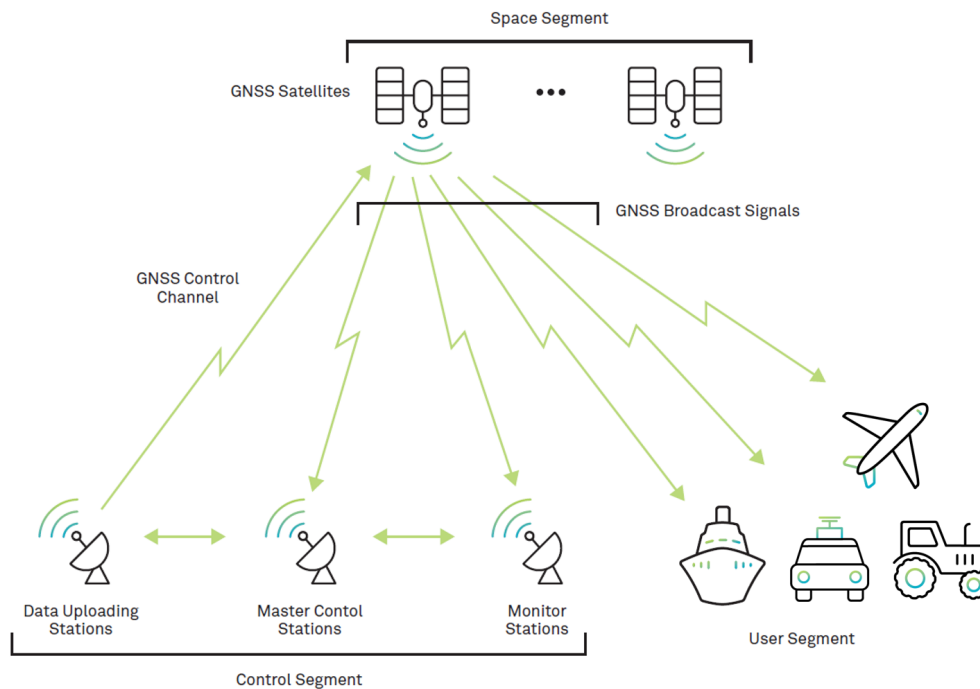


Figure 1.1 GNSS segments: space segment, control segment and user segment (from NovAtel Commons (2021)).

### 1.1.1 GNSS constellations

GPS constellation is composed of at least 24 Medium Earth Orbit (MEO) satellites in six orbital planes of  $56^\circ$  inclination with global coverage. The GPS satellites are able to transmit signals at L1 (1575.42 MHz) and L2 (1227.6 MHz) frequencies. Recently, a new frequency link L5 (1176.45 MHz) is introduced for modern civilian users. GLONASS constellation comprises 24 MEO satellites in three orbital planes of  $64.8^\circ$  inclination with global coverage. The GLONASS satellites transmit signals at L1 (1602-1615.5 MHz) and L2 (1246-1256.5 MHz) frequency bands. The L1 frequency band is spaced by 0.5625 MHz, while the L2 frequency band is spaced by 0.4375 MHz. Galileo constellation is composed of 30 MEO satellites in three orbital planes of  $56^\circ$  inclination with global coverage. The Galileo satellites broadcast signals at E1 (1575.42 MHz), E5a (1176.45 MHz), E5b (1207.14 MHz), and E6 (1278.75 MHz) frequencies. In addition, Galileo provides three kinds of positioning service on Galileo signals for GNSS users and also international satellite-based search and rescue service on E1 signal. BDS constellation consists of 27 MEO satellites, 3 Inclined GeoSynchronous Orbit (IGSO) satellites, and 5 Geostationary (GEO) satellites. 27 MEO satellites of BDS are distributed at three orbital places of  $55^\circ$  inclination with global coverage. BDS satellites transmit signals at B1 (1561.098 MHz), B2 (1207.14

MHz), and B3 (1268.52 MHz) frequencies. The special Beidou GEO constellations can provide significant contributions to GNSS users including broadcasting GNSS signals, short message communication between users and master control station, as well as satellite-based augmentation services. In addition, Beidou GEO satellites can be also useful for ionospheric monitoring due to the special orbits (Hu et al., 2017; Xiong et al., 2016). QZSS constellation comprises 3 IGSO and 1 GEO satellite with a regional coverage over East Asia (Yang et al., 2020). QZSS satellites broadcast signals at L1 (1575.42 MHz), L2 (1227.6 MHz), L5 (1176.45 MHz), and E6 (1278.75 MHz) frequencies. IRNSS constellation consists of 4 IGSO and 3 GEO satellites with a regional coverage over India. IRNSS satellites transmit signals at L5 (1176.45 MHz) and S (2492.028 MHz) frequencies (Teunissen and Montenbruck, 2017).

As shown in Figure 1.2, MEO satellites of GPS, GLONASS, Galileo, and BDS are orbiting around 20000 km height above sea level, while the IGSO and GEO are orbiting at 35786 km height above sea level.

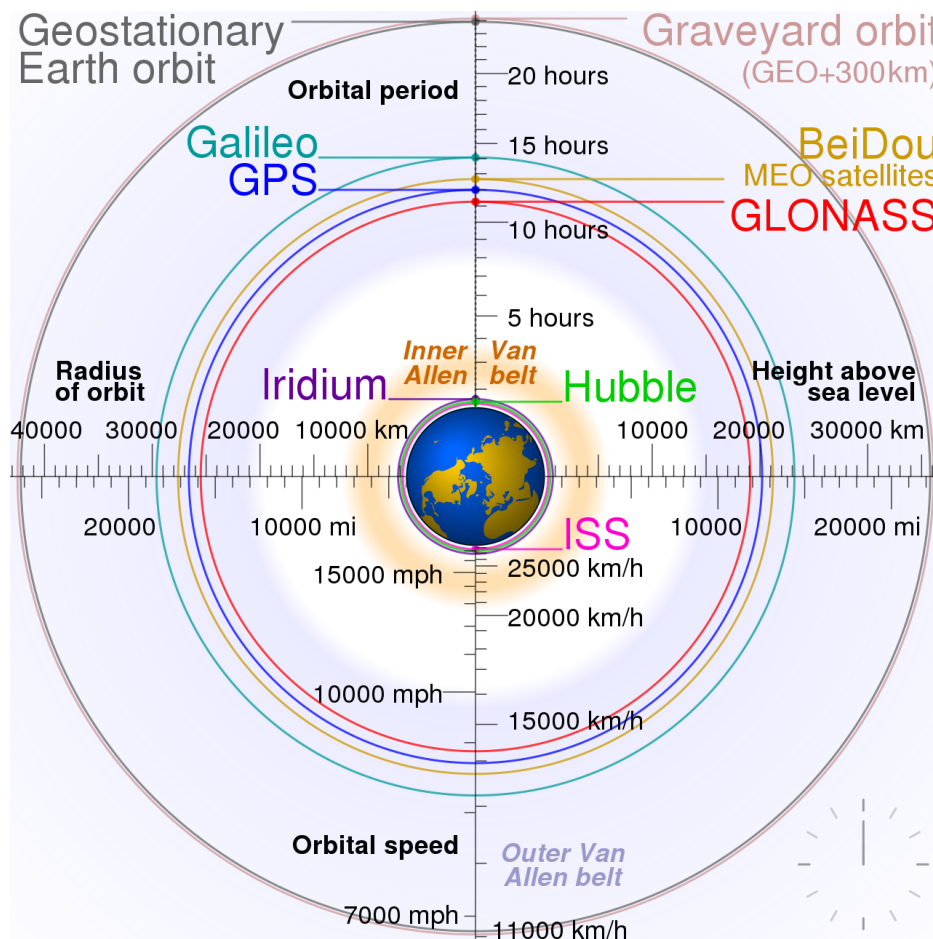


Figure 1.2 orbital height and period of GNSS constellations (from Wikimedia Commons (2021)).

### 1.1.2 GNSS measurements and error sources

The commonly used GNSS measurements are pseudorange and carrier phase observations. The pseudorange and carrier phase observations contain the measure of the geometric distance between any given pair of GNSS satellite and receiver, while they are also affected by different dependences (Teunissen and Montenbruck, 2017).

The pseudorange and carrier phase observations can be expressed as follows:

$$P_{i,k}^j = \rho_i^j + c(dt_i - dt^j) + R_i^j + I_{i,k}^j + T_i^j + D_{i,k} - D_k^j + M_{i,k}^j + \varepsilon_{i,k}^j \quad (1.1)$$

$$L_{i,k}^j = \rho_i^j + c(dt_i - dt^j) + R_i^j - I_{i,k}^j + T_i^j + \lambda_k N_{i,k}^j + b_{i,k} - b_k^j + W_k + m_{i,k}^j + \zeta_{i,k}^j \quad (1.2)$$

where:

- $i$  refers to the receiver.
- $j$  refers to the satellite
- $k$  represents the frequency.
- $P$  is obtained by multiplying the speed of light in the vacuum by the time difference between the signal reception time of receiver and signal transmission time of satellite.
- $\rho$  is the geometric distance between receiver and satellite.
- $dt_i$  and  $dt_j$  are clock error of receiver and satellite.
- $R$  is the general and special relativistic correction term.
- $I$  is the ionospheric delay.
- $T$  is the tropospheric delay.
- $D_i$  and  $D_j$  are the instrumental delays of receiver and satellite, respectively.
- $M$  and  $\varepsilon$  are the multipath and thermal noise of pseudorange observation.
- $L$  is the accumulated phase of carrier signal from the satellite.
- $N$  is the carrier phase ambiguity.
- $b_i$  and  $b_j$  are the phase bias of receiver and satellite, respectively.
- $W$  is wind-up effect related with right hand polarized signal.
- $m$  and  $\zeta$  are multipath and thermal noise of carrier phase observation.

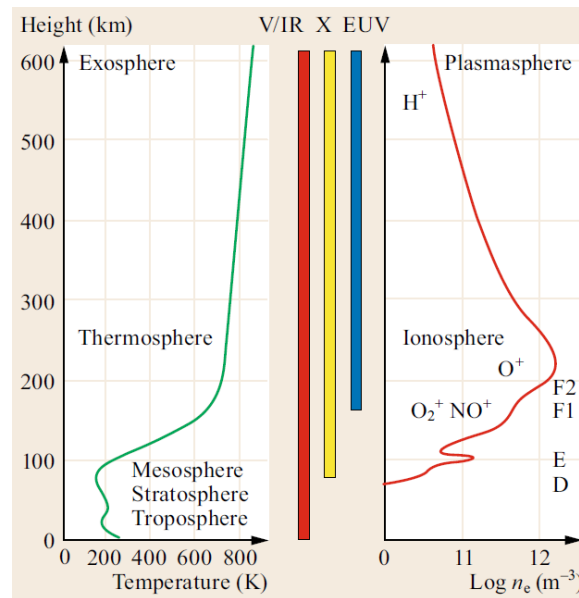


Figure 1.3 The temperature of atmosphere, solar radiation depths and the structure of the electron density of ionosphere, from Teunissen and Montenbruck (2017).

## 1.2 Ionosphere

Ionosphere is the upper atmosphere ranging from around 60 km to 1000 km above the earth surface. Neutral atmospheric gas atoms and molecules are partially ionized by solar radiation (mainly Extreme ultraviolet lithography, i.e. EUV, and X-ray emissions) and high-energy particles in ionosphere as shown in Figure 1.3. The resultant mixture of free electrons and ions constitutes the ionosphere plasma. The density of neutral atmospheric gas decreases with altitude and the solar radiation increases with altitude due to the atmosphere absorption. Hence the electron density of ionosphere reaches a peak around 200 to 400 km altitude (Hernández-Pajares et al., 2011).

### 1.2.1 Ionospheric error in GNSS measurements

The ionosphere plasma is a dispersive medium for GNSS signals which are electromagnetic waves. When the GNSS signals propagate through the ionosphere plasmas, both velocity and geometric ray path are affected. Since the frequencies of GNSS signals are high (more than 1 GHz), the geometric ray bending effect of ionosphere plasma is neglectable (mm level at low elevation). The velocity of GNSS signals in ionosphere can be derived as Eq 1.3 with the help of Appleton expression (Hernández-Pajares et al., 2010).

$$\left\{ \begin{array}{l} n_p \approx 1 - \frac{40.3Ne}{f^2} \\ n_g = \frac{\partial(n_p \cdot f)}{\partial f} = n_p + f \frac{dn_p}{df} \approx 1 + \frac{40.3Ne}{f^2} \\ v_p = \frac{c}{n_p} \approx c \left(1 + \frac{40.3Ne}{f^2}\right) \\ v_g = \frac{c}{n_g} \approx c \left(1 - \frac{40.3Ne}{f^2}\right) \end{array} \right. \quad (1.3)$$

where:

- $n_p$  is the first-order approximation of phase refractive index for carrier phase signal within ionosphere. It should be noted that the higher order phase refractive index only accounts for less than 0.1% of overall refractive index. And the peak value of higher order effect of refractive index for GNSS measurement is below 2 cm which can be negligible (Hernández-Pajares et al., 2014).
- $n_g$  is the group refractive index for pseudorange signal within ionosphere.
- $Ne$  is the electron density.
- $f$  is the frequency of the signal.
- $v_p$  is the propagating velocity of carrier phase signal within ionosphere.
- $v_g$  is the propagating velocity for pseudorange signal within ionosphere.
- $c$  is the speed of light in a vacuum

As it can be seen in Eq 1.3, the  $v_p$  is slightly larger than the light speed in the vacuum and  $v_g$  is slightly smaller since the electron density  $Ne$  and frequency  $f$  is positive. With the propagating velocity of GNSS pseudorange and carrier phase signals, the ionospheric error for GNSS measurements can be calculated as Eq 1.4 (considering only ionospheric effect).

$$\left\{ \begin{array}{l} \int_{r_j}^{\vec{r}_i} Neds = S \\ \Delta s_{i,g}^j \simeq P_i^j - \rho_i^j = c \left( \int_{r_j}^{\vec{r}_i} \frac{ds}{v_g} - \int_{r_j}^{\vec{r}_i} \frac{ds}{c} \right) = \int_{r_j}^{\vec{r}_i} (n_g - 1) ds = \frac{40.3}{f^2} \int_{r_j}^{\vec{r}_i} Neds = \frac{40.3 \cdot S}{f^2} \\ \Delta s_{i,p}^j \simeq L_i^j - \rho_i^j = c \left( \int_{r_j}^{\vec{r}_i} \frac{ds}{v_p} - \int_{r_j}^{\vec{r}_i} \frac{ds}{c} \right) = \int_{r_j}^{\vec{r}_i} (n_p - 1) ds = -\frac{40.3}{f^2} \int_{r_j}^{\vec{r}_i} Neds = -\frac{40.3 \cdot S}{f^2} \end{array} \right. \quad (1.4)$$

$$I = \frac{40.3 \cdot S}{f^2} \quad (1.5)$$

where:

- $s$  is the line-of-sight geometric distance between satellite and receiver.
- $\vec{r}^j, \vec{r}_i$  are the position vector of the receiver  $i$  and satellite  $j$ .
- $S$  is the integrated electron density along the line-of-sight geometric distance between satellite and receiver. And it is generally called Slant Total Electron Content (STEC).
- $\Delta s_{i,g}^j$  is the ionospheric error in the pseudorange observation for receiver  $i$  and satellite  $j$ .
- $\Delta s_{i,p}^j$  is the ionospheric error in the carrier phase observation for receiver  $i$  and satellite  $j$ .
- $I$  is the ionospheric delay introduced in Eq 1.1. Because the  $v_g < c$ , the pseudorange observation is delayed. Since the high-order ionospheric effect is minor, only the first-order ionospheric error is introduced to represent the ionospheric effect on GNSS measurements (Hernández-Pajares et al., 2014).

## 1.2.2 Ionospheric error mitigation for GNSS measurements

To date, three methods are commonly used by GNSS users to mitigate the ionospheric error: the combination of GNSS measurements, empirical ionospheric models, and ionospheric models based on GNSS measurements.

### Combination of GNSS measurements

Combining Eq 1.1, Eq 1.2 and Eq 1.5, ionospheric-free combinations can be formed to remove the ionospheric effect on GNSS measurements as follows:

$$\begin{aligned} P_c^j &\equiv \frac{f_1^2 P_{i,1}^j - f_2^2 P_{i,2}^j}{f_1^2 - f_2^2} \\ &= \rho_i^j + c(dt_i - dt^j) + R_i^j + T_i^j \\ &\quad + \frac{1}{f_1^2 - f_2^2} [f_1^2 (D_{i,1} - D_1^j + M_{i,1}^j + \epsilon_{i,1}^j) - f_2^2 ((D_{i,2} - D_2^j + M_{i,2}^j + \epsilon_{i,2}^j))] \end{aligned} \quad (1.6)$$

$$\begin{aligned}
Lc_i^j &\equiv \frac{f_1^2 L_{i,1}^j - f_2^2 L_{i,2}^j}{f_1^2 - f_2^2} \\
&= \rho_i^j + c(dt_i - dt^j) + R_i^j + T_i^j + \frac{c(f_1 N_{i,1}^j - f_2 N_{i,2}^j)}{f_1^2 - f_2^2} \\
&\quad + \frac{1}{f_1^2 - f_2^2} [f_1^2 (b_{i,1} - b_1^j + W_1 + m_{i,1}^j + \zeta_{i,1}^j) - f_2^2 (b_{i,2} - b_2^j + W_2 + m_{i,2}^j + \zeta_{i,2}^j)]
\end{aligned} \tag{1.7}$$

$$\begin{aligned}
O_{i,GRA}^j &\equiv \frac{1}{2} (P_{i,k}^j + L_{i,k}^j) \\
&= \rho_i^j + c(dt_i - dt^j) + R_i^j + T_i^j + \\
&\quad \frac{1}{2} (\lambda N_i^j + D_{i,k} - D_k^j + M_{i,k}^j + \varepsilon_{i,k}^j + b_{i,k} - b_k^j + W_k + m_{i,k}^j + \zeta_{i,k}^j)
\end{aligned} \tag{1.8}$$

Eq 1.6 and Eq 1.7 are typically used for dual-frequency GNSS receivers while single-frequency GNSS receiver can utilize Eq 1.8 to remove the ionospheric effect. However, after removing the ionospheric effect by these combinations of GNSS measurements, the larger pseudorange multipath and measurement noise are introduced in the observation equations.

### Empirical ionospheric model

Empirical ionospheric models including Bent model, International Reference Ionosphere (IRI) model, and Klobuchar model are generally derived from historic ionospheric sounding data (for example, ionosonde, incoherent scatter radars) to characterize ionosphere. Bent model characterizes the ionospheric electron density as a function of latitude, longitude, time, season, and solar radio flux, while IRI model describes monthly averages of electron density in the altitude range 50–2000 km on a global scale (Bent et al., 1975; Rawer et al., 1978). In addition, the widely used ionospheric correction model for single-frequency GPS users is the broadcast model (Klobuchar model) describing the ionospheric errors as constant values during night and positive cosine function during the day (Klobuchar, 1987). And Beidou-2 broadcasts a ionospheric correction model similar to Klobuchar model for BDS users. GNSS users can obtain STEC from empirical ionospheric models and use the obtained STEC for ionospheric correction in Eq 1.5. However, the accuracy of most empirical ionospheric models for GNSS ionospheric correction is limited and can mitigate around 50% to 70% ionospheric error (Orús et al., 2002; Wang et al., 2018, 2017).



NeQuick Galileo (NeQuick-G) broadcast model driven by the effective ionization level parameters is selected for Galileo single-frequency users (Angrisano et al., 2013; Prieto-Cerdeira et al., 2014). And NeQuick-G broadcast model can reduce more than 30% ionospheric errors during the long period assessment (Montenbruck and Rodríguez, 2020; Perez et al., 2018).

### GNSS-based ionospheric model

To focus on the ionospheric STEC correction for GNSS users, GNSS-based ionospheric models are mostly used. Currently, three methods are commonly used to derive STEC for GNSS-based ionospheric models. Taking advantage of dual-frequency GNSS measurements as a geometry-free combination, the STEC can be extracted and projected into Vertical Total Electron Content (VTEC) as shown in Eq. 1.9, Eq. 1.10 and Eq. 1.11. The multipath effect of pseudorange observations can be few meters, while the multipath effect of carrier phase observations is typically around few millimeters and in any case below few centimeters. The carrier-to-code leveling method is used to mitigate the multipath effect of pseudorange observations (Ciraolo et al., 2007). The geometry-free combination of pseudorange and carrier phase observations with carrier-to-code leveling method is formed to extract STEC and instrumental delays by fitting an ionospheric VTEC model (Liu et al., 2021c). The second method is to only use carrier phase observations from Eq. 1.10 and estimate the carrier ambiguity together with ionospheric model (Hernández-Pajares et al., 1997, 1999). In addition, the ionospheric model can be global or regional depending on the situation. And the third method employs Precise Point Positioning (PPP) technique relying on precise satellite orbits and clocks information to derive STEC (Liu et al., 2018; Zhang et al., 2012, 2019).

$$\begin{aligned}
 PI_i^j &\equiv P_{2i}^j - P_{1i}^j \\
 &= 40.3 \left( \frac{1}{f_2^2} - \frac{1}{f_1^2} \right) \text{STEC}_i^j + (D_{i,2} + D_{i,1} - D_{i,1}^j - D_{i,2}^j) \\
 &+ (M_{i,2}^j - M_{i,1}^j) + (\varepsilon_{2,i}^j - \varepsilon_{1,i}^j)
 \end{aligned} \tag{1.9}$$

$$\begin{aligned}
 LI_i^j &\equiv L_{1i}^j - L_{2i}^j \\
 &= 40.3 \left( \frac{1}{f_2^2} - \frac{1}{f_1^2} \right) \text{STEC}_i^j + (\lambda_2 N_{i,2}^j - \lambda_1 N_{i,1}^j) \\
 &+ (m_{i,2}^j - m_{i,1}^j) + (W_{i,2}^j - W_{i,1}^j) + (\zeta_{i,2}^j - \zeta_{i,1}^j)
 \end{aligned} \tag{1.10}$$

$$\begin{cases} VTEC = STEC/MF \\ MF = [1 - \sin^2 z / (1 + H_{ion}/R_E)^2]^{-\frac{1}{2}} \end{cases} \quad (1.11)$$

- $MF$  is one of the commonly used mapping functions.
- $z$  is the satellite zenith angle.
- $H_{ion}$  is the height of the ionospheric single-layer assumption.
- $R_E$  is the radius of the earth.

Accurate STEC from GNSS-based ionospheric models has been widely used by GNSS users. Beidou-3 designs a new broadcast ionospheric model with nine parameters of spherical harmonic expansion based on GNSS data (Wang et al., 2021; Yang et al., 2020; Yuan et al., 2019). There are also many global ionospheric models based on GNSS data with different algorithms (Teunissen and Montenbruck, 2017). And the accuracy of STEC from most global ionospheric models is around 2-8 TEC Unit (TECU, equivalent to  $10^{16} el/m^2$ ) (Hernández-Pajares et al., 2009, 2017a; Orús et al., 2002).

### 1.3 GNSS-based global ionospheric maps

GNSS-based Global Ionospheric Maps (GIMs) are generally global ionospheric models based on only TEC from GNSS. Established in 1998, the ionosphere working group of International GNSS Service (IGS) agreed on generating, assessing, and combining routine global ionospheric maps in IONosphere map EXchange (IONEX) format (Hernández-Pajares et al., 2009; Schaer et al., 1998). The IGS-GIMs in IONEX format describe TEC distribution at separated grid points with a spatial resolution of  $5^\circ \times 2.5^\circ$  on a global scale and a standard time resolution of 2 hours.

The initial Ionospheric Associate Analysis Centers (IAACs) were the Center for Orbit Determination in Europe (CODE), European Space Agency (ESA), Jet Propulsion Laboratory (JPL), Canadian Geodetic Survey of Natural Resources Canada (NRCan), and Universitat Politècnica de Catalunya (UPC) (Feltens, 2007; Ghoddousi-Fard, 2014; Hernández-Pajares et al., 1999, 1998; Komjathy et al., 2005; Mannucci et al., 1998; Schaer, 1999; Schaer et al., 1996). Chinese Academy of Sciences (CAS) and Wuhan University (WHU) were accepted as new IAACs in 2015 (Li et al., 2015; Yuan and Ou, 2004; Zhang et al., 2013; Zhang and Zhao, 2019). For different purposes, IGS IAACs commonly generate final, rapid,

real-time, and predicted GIMs. The latencies of final, rapid GIMs are 1-2 weeks and 1-2 days respectively, while the latency of real-time GIMs is around few minutes. And the 1-day and 2-day predicted GIMs can provide TEC maps with lower accuracy (Hernández-Pajares et al., 2009; Li et al., 2020; Liu et al., 2021c; Monte Moreno et al., 2018; Yang et al., 2021; ?).

As one of IGS IAACs, UPC gathers ambiguous STEC measurements from more than one hundred dual-frequency GNSS receivers and estimates TEC distribution of each voxel every 15 minutes with Kriging interpolation technique by assuming a tomographic two-layer voxel model solved by means of a Kalman filter in a sun-fixed geomagnetic reference frame on a global scale (Hernández-Pajares et al., 1999, 1998; Orús et al., 2005). The resultant rapid GIM of UPC is called UPC Quarter-of-an-hour time resolution Rapid GIM (UQRG). According to previous assessments, UQRG is one of the most accurate GIMs (Hernández-Pajares et al., 2017a; Roma-Dollase et al., 2018b). Furthermore, the performance of UQRG on the most troublesome polar regions with very few GNSS receivers has been reported. UQRG is able to obtain reliable TEC estimates and captures the TEC structures even in the most troublesome polar regions (Hernández-Pajares et al., 2020; Monte-Moreno et al., 2021).

## 1.4 Space weather effects

Space weather refers to the environmental conditions of space encompassing the earth affected by the solar system. The varying radiation from space weather environments can be harmful to astronauts, satellite components, passengers in airplanes. And the irregular variation of electron density in ionosphere can affect radio systems propagating through ionosphere (including telecommunications, GNSS, altimeters, radar) due to space weather events (Buonsanto, 1999; Demyanov and Yasyukevich, 2021; Hernández-Pajares et al., 2012; Monte-Moreno and Hernández-Pajares, 2014; Schwenn, 2006).

For GNSS users, different space weather events can degrade the performance of GNSS services. The common space weather events affecting GNSS users are as follows:

- Solar radio burst might cause the reduction of signal-to-noise ratio, loss of track, and impairment of GNSS positioning (Sato et al., 2019).
- Ionospheric irregularities can affect GNSS signals propagating through irregularities. They can cause ionospheric scintillations with fluctuations in amplitude and phase of GNSS signal (Pi et al., 1997).
- Ionospheric perturbations might degrade GNSS positioning (Jakowski and Hoque, 2019).

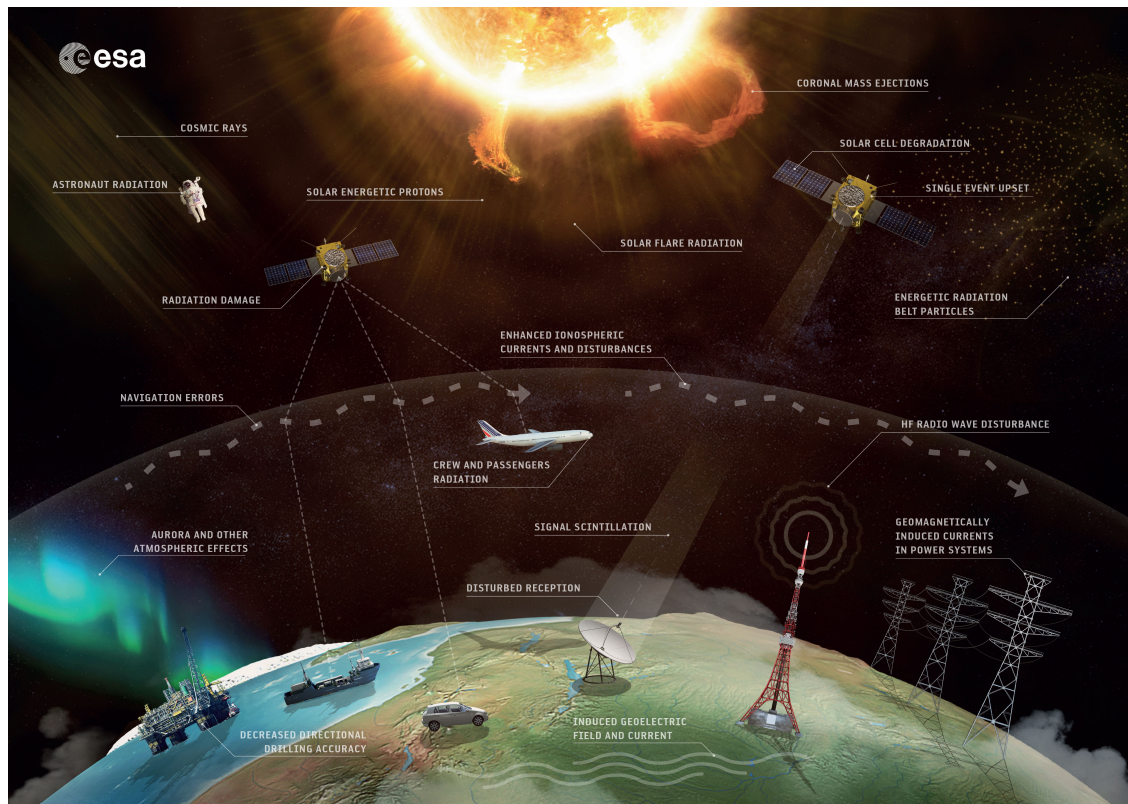


Figure 1.4 Space weather effects. (reproduced from ESA Commons (2021))

- Ionospheric storms with increasing TEC can also impair GNSS positioning (Nishioka et al., 2017).

# Chapter 2

## Summary of the work performed

The present chapter summarizes the main contributions provided by this Ph.D. study. The results presented in the following sections have been validated by the international scientific community through the assessment of papers published in peer-reviewed journals. A selection of quality indexes for each journal can be found in Chapter 3 and the original manuscripts are appended at Chapter 5.

### 2.1 The relationship between GIM assessment methods in post-processing and real-time mode

The commonly used GIM assessment reference observations are Jason-altimeter VTEC measurements, differences of GNSS STEC (dSTEC) measurements in post-processing mode and Real-Time dSTEC (RT-dSTEC) measurements (Hernández-Pajares et al., 2017b; Roma-Dollase et al., 2018a,b):

- Jason-altimeter observations can provide direct VTEC measurements including a small system bias (few TECU level) but excluding the plasmaspheric electron content above 1300 km height in the assessment. The plasmaspheric electron content variation is up to a few TECU and is relatively a small part when compared with the GIM errors over the oceans. As a consequence, the GIM validation based on dual-frequency Jason-altimeter measurements is sensitive to the actual error of the GIMs on the oceans where are the most challenging regions for GIMs (containing few nearby receivers in such regions) and typically far from permanent GNSS receivers potentially contributing to the GIM.
- The dSTEC observations consist of the difference of ionospheric combination of carrier phases ( $L1 - L2$ ) within a continuous phase-arc and regarding the line-of-

the-sight with the highest elevation involving different geometries but avoiding the highest mapping function errors by applying an elevation mask of 15 degrees. And the mapping function is used by GNSS users to convert GIM-VTEC to GIM-STECC for GNSS positioning or the reversal for ionospheric modelers. Therefore, the dSTECC observations, containing different geometries and mapping function values, are accurate and direct measurements for evaluating along ray path GIM-STECC which is commonly used by GNSS users to calculate ionospheric correction. In addition, the common agreed ionospheric thin layer model is commonly adopted to be 450 km height in the generation of GIM to provide VTECC in a consistent way for different ionospheric analysis centers. And in this way the GNSS users are able to consistently recover a most accurate STECC from GIM-VTECC by the commonly agreed mapping function.

- The RT-dSTECC assessment is based on Root Mean Square (RMS) of the dSTECC error in real-time. In order to adapt to the real-time processing mode, the ambiguous reference STECC measurement is set to be the first elevation angle higher than  $10^\circ$  within a continuous phase arc to enable the RT-dSTECC calculation in the elevation-ascending arc.

The relationship between GIM assessment methods in post-processing and real-time mode is as follows:

- The GIM error versus Jason-VTECC measurements has a high correlation with the GIM error versus dSTECC-based measurements, although the Jason-VTECC measurements are vertical and the dSTECC measurements are slant. As demonstrated in Hernández-Pajares et al. (2017b), the Jason-altimeter VTECC assesment and dSTECC assessment are independent and consistent for GIM evaluation. In other words, the slant ray path geometry changes does not affect the capability of dSTECC reference data to rank the GIM, and the plasmaspheric component does not significantly affect the assessment of GIMs based on Jason-VTECC data.
- The dSTECC assessment and RT-dSTECC assessment are both targeted on the direct measurements of the difference of STECC within a continuous phase-arc involving different geometries.

The ambiguous reference STECC measurement of dSTECC assessment is set to be the highest elevation angle, while the ambiguous reference STECC measurement of RT-dSTECC assessment is set to be the first elevation angle higher than  $10^\circ$  within a continuous phase arc due to the limitation of real-time mode. In this regard, RT-dSTECC assessment is supposed to be influenced by the reference STECC measurement within a

continuous phase arc.

To be independent from the TEC used in GIM computation, the GNSS stations used for dSTEC assessment should be not located close to the stations used in GIM computations. And due to the limit of real-time available GNSS stations, the RT-dSTEC assessment chooses the common GNSS stations used in GIM computations. Therefore, the typical dSTEC assessment is providing external post-fit residuals of GIMs, while RT-dSTEC assessment is presenting internal post-fit residuals of real-time GIMs.

## 2.2 Real-time GIM combination and validation

The Real-Time Working Group (RTWG) of IGS was established to fulfill the demand for real-time GNSS positioning and other applications. Real-time service (RTS) of RTWG was officially started from 2013 (Caissy et al., 2012; Elsobeiey and Al-Harbi, 2016). In the frame of RTWG, the first official version of IGS combined real-time GIM is generated with the help of colleagues from UPC-IonSAT research group, RTWG and Ionosphere Working Group (Iono-WG). IGS real-time GIMs have already been used in real-time GNSS positioning service and might also be able to contribute to ionospheric monitoring.

Currently, there are four IGS centers providing real-time GIMs: CAS, Centre National d'Etudes Spatiales (CNES), UPC, and WHU. A brief summary of real-time GIMs from different IGS centers is shown in Table 2.1.

The IGS combined real-time GIM is based on the weighted mean value of VTEC from different IGS centers. To calculate the weight of different real-time GIMs, the RT-dSTEC assessment is adopted in real-time mode. The real-time stations used for RT-dSTEC assessment are located (green points) in Figure 2.1. And the generation of IGS combined real-time GIM can be seen in Figure 2.2.

To evaluate the performance of IGS real-time GIMs, the Jason-2 altimeter VTEC assessment, dSTEC assessment in post-processing mode and RT-dSTEC assessment in real-time mode are involved (Liu et al., 2021c). The 3-month data from 1 December 2020 to 1 March 2021, containing the two significant events (new contributing WHU real-time GIM from 3 January 2021 and the transition of the interpolation technique of UPC real-time GIM on 4 January 2021), have been selected to study the performance of different IGS real-time GIMs. The temporal resolutions of received real-time GIMs can be the 20 minutes and the original one. And the temporal resolution of IGS combined real-time GIM is 20 minutes. In this regard, the following research focuses on the comparison of 20 minutes time resolution among IGS real-time GIMs. It should be noted that it is also interesting to compare the performance of different real-time GIMs between 20 minutes and the original temporal

Table 2.1 The brief summary of different IGS real-time GIMs

Agency /GIM	Runing date	Extra ionospheric information	Differential Code Biases (DCB) computation	GIM computation
CAS	Mid-2017 to present	2-day predicted GIM as background information	Estimated at the same time with local VTEC, and corrected by three-day aligned code bias	Observations with predicted GIMs are used to generate 15-degree spherical harmonic expansion GIM in solar-geographic frame
CNES	End-2014 to present (with an evolution of the spherical harmonic degree)	No	Expected in a forthcoming version	12-degree spherical harmonic expansion GIM which is generated in solar-geographic frame
UPC /URTG	2011-02-06 to 2019-09-08	1-2 day rapid GIM UQRG as background information	optional	Tomographic model with kriging interpolation method and frozen rapid GIM (UQRG) as a priori model, which generates real-time GIM in sun-fixed geomagnetic frame
UPC /USRG	2019-09-08 to present	1-2 day rapid GIM UQRG as background information	optional	Tomographic model with spherical harmonic interpolation method and frozen rapid GIM (UQRG) as a priori model, which generates real-time GIM in sun-fixed geomagnetic frame
UPC /UADG	2021-01-04 to present	historical UQRG (since 1996) as databases	optional	Tomographic model adopting atomic decomposition and LASSO solution for the global interpolation with the help of historical GIMs (UQRG), which generates GIM in sun-fixed geomagnetic frame
WHU	2020-11-09 to present	2-day predicted GIM as background information	Directly use the previous satellite and receiver DCB estimated simultaneously with WHU rapid GIM	Observations with predicted GIMs yield 15-degree spherical harmonic expansion GIM in solar-geomagnetic frame



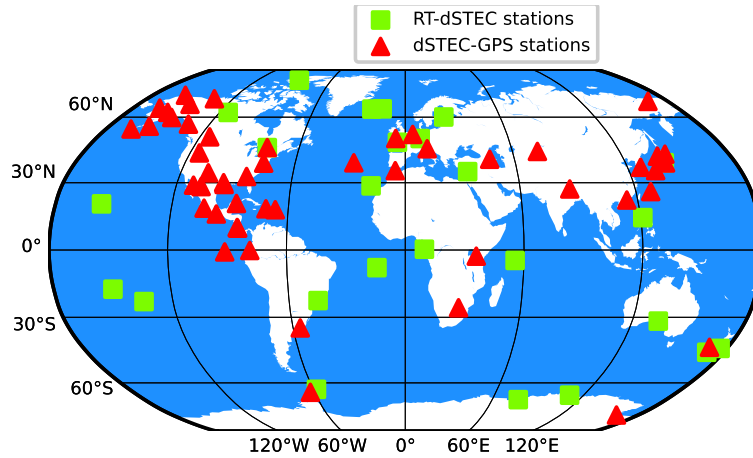


Figure 2.1 The 25 common real-time stations for RT-dSTEC assessment (in green color) and 50 external GNSS stations for dSTEC-GPS assessment (in red color)

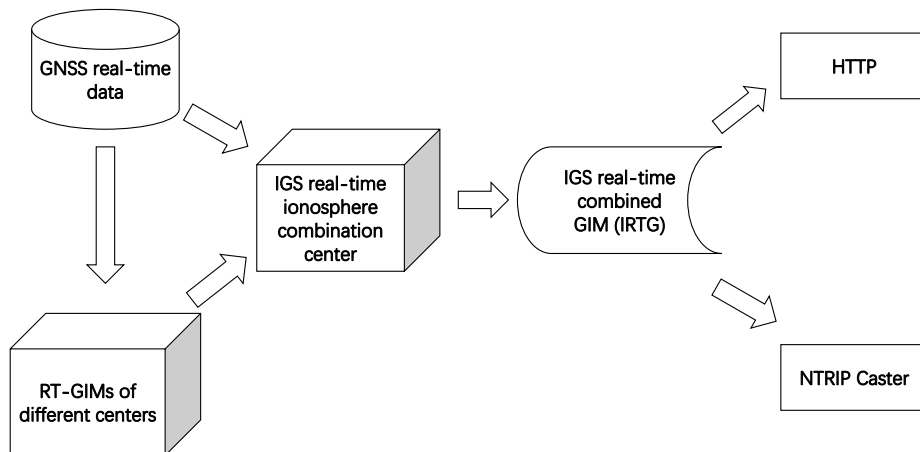


Figure 2.2 Data flow for the IGS combined real-time GIM

resolution (see details in the next section). The names of compared IGS combined real-time GIMs can be seen in Table 2.2.

Table 2.2 The Id. of contributing IGS real-time GIMs

Agency	20-minute real-time GIM	real-time GIM with full temporal resolution
CAS	crtg	crfg
CNES	cnes	cnfs
UPC	upc1	upf1
WHU	whu0	whf0
IGS	irtg	irfg <sup>a</sup>

<sup>a</sup> irfg and irtg are the same.

As shown in Figure 2.3 and Table 2.3, the UPC real-time GIM (upc1) obtained a obvious improvement after the transition of interpolation technique on 4 January 2021. Accordingly, the accuracy of IGS combined real-time GIM (irtg) was also increased. Compared with IGS rapid GIMs (corg, ehrg, emrg, esrg, igrg, jprg, uhrg, uprg, uqrg, whrg) and IGS final combined GIM (igsg), the upc1 and irtg are equivalent to the post-processed GIMs and even better than some rapid GIMs. The accuracy of CAS real-time GIM (crtg) and CNES real-time GIM (cnes) is close to the post-processed GIMs, while WHU real-time GIM (whu0) is slightly worse than the other GIMs. And in Table 5, the rank of real-time GIMs in the RT-dSTEC assessment is similar to the dSTEC assessment. The large RMS error of RT-dSTEC assessment coincides with the low elevation angle of the reference STEC measurement in the RT-dSTEC assessment.

## 2.3 Temporal resolution of GIM

The temporal resolution of different IAAC GIMs ranges from 15 minutes to 2 hour (Roma-Dollase et al., 2018b). However, the variation of ionospheric electron density can be highly affected by many factors such as solar radiation, as well as plasma transport. In addition, the irregular variation of electron density under different space weather events including geomagnetic storms and traveling ionospheric disturbance can present a challenge for ionospheric modelling (Hernández-Pajares et al., 2006; Kivelson, 1995). Therefore, the error associated with the assumption that TEC varies linearly between consecutive VTEC maps during a long period (for example, 2 hours) in a sun-fixed reference frame, might not be neglectable for the time interpolation of GIM.

To investigate the influence of temporal resolution, different GIMs derived from 15 minutes UQRG by direct downsampling of the daily UQRG to all the multiples of 15 minutes

Table 2.3 Standard deviation of GIM-VTEC minus Jason-VTEC in Jason-altimeter VTEC assessment (last two columns), and dSTEC assessment results of real-time GIMs on January 03 (second and third column) and January 05 (fourth and fifth column) in 2021.

GIM	RMS error of January 03 in dSTEC assessment (TECU)	Relative error of January 03 in dSTEC assessment (%)	RMS error of January 05 in dSTEC assessment (TECU)	Relative error of January 05 in dSTEC assessment (%)	Overall standard deviation of the GIM-VTEC versus Jason-VTEC from December 01 of 2020 to January 03 of 2021 in Jason-altimeter VTEC assessment (TECU)	Overall standard deviation of GIM-VTEC versus Jason-VTEC from January 04 of 2021 to March 01 of 2021 in Jason-altimeter VTEC assessment (TECU)
corg	2.90	45.07	3.35	49.20	3.1	2.9
ehrg	2.54	39.55	2.81	41.23	3.0	2.8
emrg	2.62	40.75	2.73	40.08	3.2	2.9
esrg	2.70	41.98	3.06	44.99	3.2	3.0
igrg	2.60	40.40	3.06	44.99	2.9	2.8
jprg	2.73	42.46	2.86	41.98	2.8	2.7
uhrg	1.91	29.69	2.21	32.43	3.9	2.8
uprg	2.04	31.80	2.41	35.39	3.9	2.8
uqrg	1.89	29.44	2.19	32.24	3.5	2.8
whrg	2.42	37.63	2.65	38.94	3.0	2.8
igsg	2.33	36.25	2.57	37.74	2.6	2.5
crtg	3.36	52.25	3.86	56.67	3.6	3.2
crfg	4.29	66.67	3.92	57.56	3.7	3.2
cnes	<b>3.35</b>	52.13	3.74	54.86	3.5	3.4
cnfs	3.58	55.73	4.62	67.88	3.5	3.4
upc1	3.85	59.91	<b>2.80</b>	41.06	4.3	<b>2.7</b>
upf1	3.87	60.20	2.81	41.26	4.5	<b>2.7</b>
whu0	5.19	80.69	5.45	79.84	4.3	4.4
whf0	5.31	82.61	5.54	81.28	4.3	4.4
whu1	4.37	67.97	4.40	64.55	4.3	3.8
irtg	<u>4.11</u>	63.86	<u>3.37</u>	49.47	<b>3.3</b>	<u>2.8</u>

value in bold font means the corresponding real-time GIM has the best performance among the remaining real-time GIMs in each column, and values of irtg are underlined for comparison.

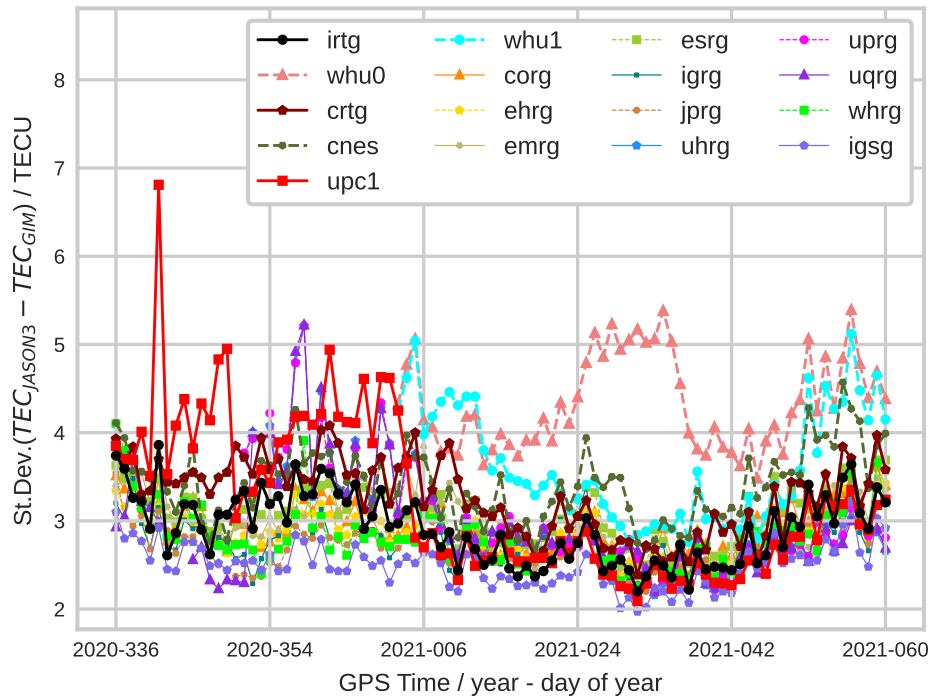


Figure 2.3 Daily standard deviation of GIM VTEC versus measured Jason3-VTEC (in TECU), from December 01 of 2020 to March 01 of 2021.

within a day are involved (Liu et al., 2021a). The derived GIMs were named 'uxxg', being 'xx' the integer multiple. The names of involved GIMs are listed in the first column with corresponding temporal resolution in the second column, and the common multiples for each GIM are indicated in the third column in Table 2.5. Then the performance of involved GIMs is compared with Jason altimeter data at different latitudes as well as various solar and geomagnetic activities from 2002 to 2019 (one and a half solar cycles) over the oceans. Another complementary assessment, the dSTEC assessment was conducted by 59 GNSS receivers during two solstice and two equinox days in 2015 over continents.

Table 2.4 RMS errors of real-time GIMs in RT-dSTEC assessment on January 03 and January 05 in 2021.

GIM	RMS error of January 03 (TECU)	RMS error of January 05 (TECU)
upc1	4.24	<b>3.91</b>
crtg	4.25	4.98
cnes	<b>3.98</b>	4.07
whu0	5.94	5.81

value in bold font means the corresponding real-time GIM has the best performance among the remaining real-time GIMs in each column.

Table 2.5 The analyzed GIM temporal resolutions, derived as 24-hour divisor time intervals and multiple of the 15-minutes time resolution of the baseline GIM uqrg.

GIM Id.	temporal resolution	common multiple
uqrg	15 minutes	$2^0 \cdot 3^0 = 01$
u02g	30 minutes	$2^1 \cdot 3^0 = 02$
u03g	45 minutes	$2^0 \cdot 3^1 = 03$
u04g	1 hour	$2^2 \cdot 3^0 = 04$
u06g	1 hour 30 minutes	$2^1 \cdot 3^1 = 06$
u08g	2 hours	$2^3 \cdot 3^0 = 08$
u12g	3 hours	$2^2 \cdot 3^1 = 12$
u16g	4 hours	$2^4 \cdot 3^0 = 16$
u24g	6 hours	$2^3 \cdot 3^1 = 24$
u32g	8 hours	$2^5 \cdot 3^0 = 32$
u48g	12 hours	$2^4 \cdot 3^1 = 48$
u96g	24 hours	$2^5 \cdot 3^1 = 96$

In Figure 2.4, the standard deviation of the difference between GIM-VTEC and Jason-VTEC was linearly related except for some fluctuations (mostly coincident with geomagnetic activity and associated Ap index variation) and the error of the twelve GIMs tends to be larger at higher mean VTEC. The discrepancy among high-resolution GIMs (uqrg to u08g) was more apparent in the northern hemisphere than in the southern hemisphere and was larger at the lower latitudinal band. As shown in the figure of the 20-degree latitudinal band, the difference among u06g, u08g, and high-resolution GIMs (uqrg, u02g, u03g, u04g) was obvious. However, that relative discrepancy was smaller at the equator, coinciding with its higher standard deviation values of the GIM VTEC discrepancy vs. the altimeter, compared with other latitudinal bands.

When the Ap index increases in Figure 2.5, the standard deviation of the difference between GIM-VTEC and Jason-VTEC tends to present a high variability. After the daily Ap index increased to 42, the response of this evolution to the variation of solar flux (F10.7) and daily mean VTEC became obvious. And most fluctuations of standard deviation were coincident with solar flux and daily mean VTEC fluctuations. In addition, the peak value of standard deviation kept increasing under intense geomagnetic activity. The magnitude of the standard deviation of GIM-VTEC versus Jason-VTEC at the southern hemisphere appeared to be slightly higher than in the northern hemisphere, and this may be related to the poor accuracy of GIM at the southern hemisphere (Hernández-Pajares et al., 2009).

The assumption of linear variation of TEC maps with different time resolution is assessed and quantified in Table 2.6 and Table 2.7. However, the ionosphere dynamics are complex

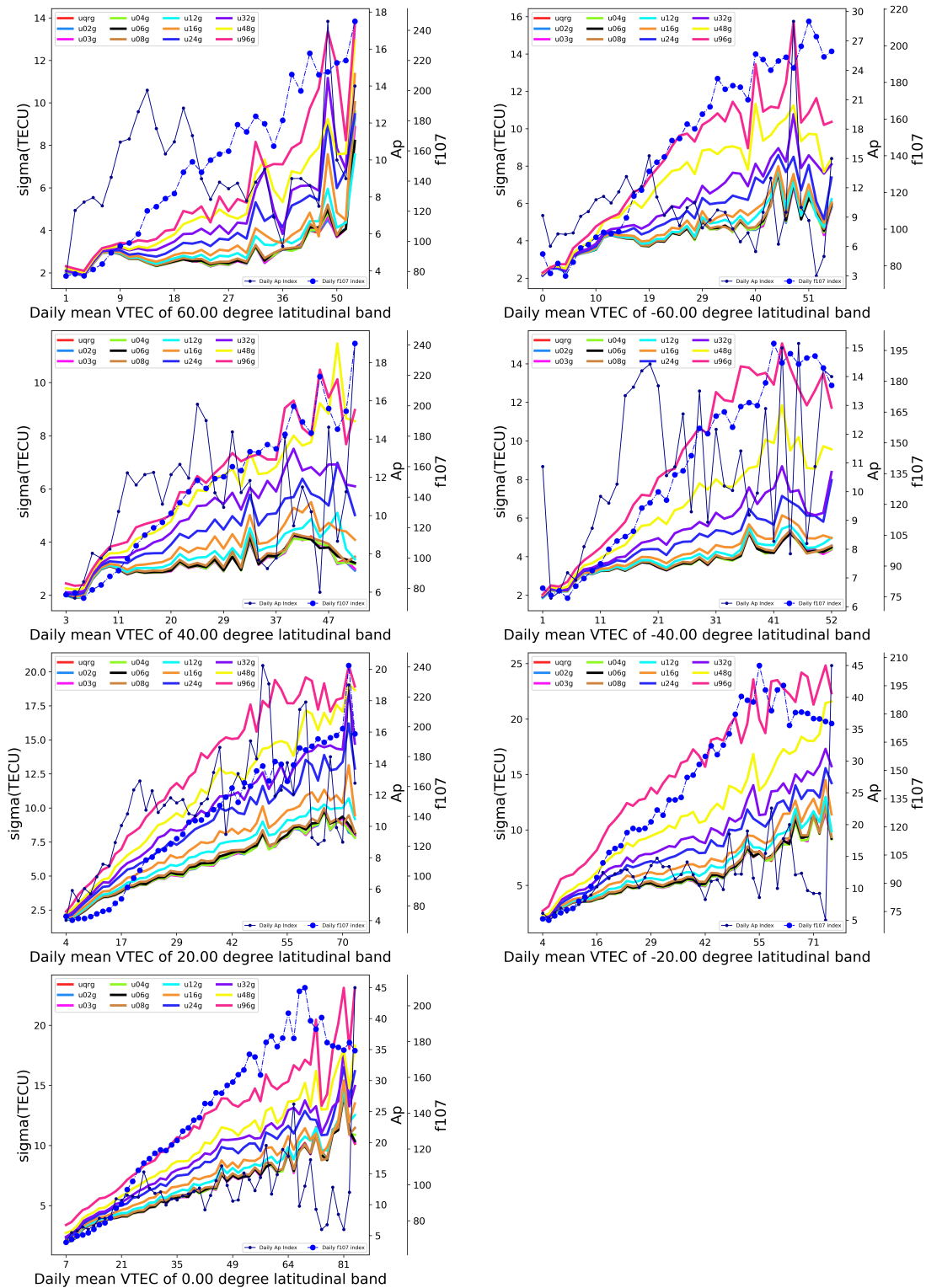


Figure 2.4 The daily standard deviation of the discrepancy of GIM VTEC vs. measured altimeter VTEC, in TECUs, is represented versus daily mean VTEC from day 26 of 2002 to day 335 of 2019, at different latitudinal bands.

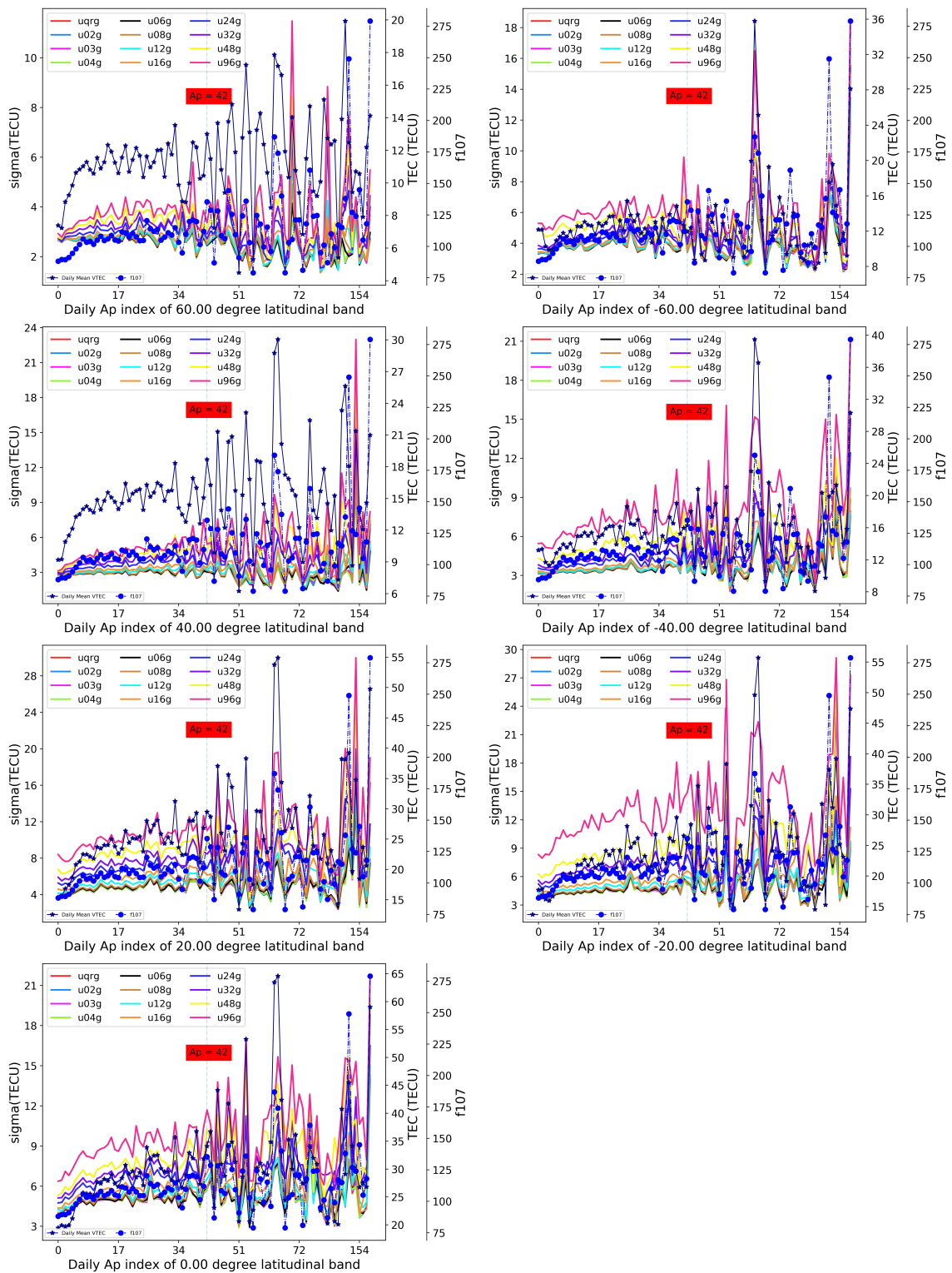


Figure 2.5 The daily standard deviation of the discrepancy of GIM VTEC vs. measured altimeter VTEC, in TECUs, is represented versus daily Ap index from day 26 of 2002 to day 335 of 2019, at different latitudinal bands

and may cause variations in electron density. This is reflected in the values from the bold value up, in each latitudinal band, which started to increase. The accuracy of GIMs with high temporal resolution (uqrg, u02g, u03g, u04g) in dSTEC assessment is quite consistent with the VTEC assessment.

Table 2.6 Standard deviation of GIM versus Jason VTEC in TECUs, from day 26 of 2002 to day 335 of 2019, at different latitudinal bands in TECUs.

GIM	-60°	-40°	-20°	0°	20°	40°	60°	Overall
uqrg	3.7	3.3	4.2	4.7	4.4	2.9	2.7	3.9
u02g	3.7	3.3	4.2	4.7	4.4	2.9	2.7	3.9
u03g	3.7	3.3	4.2	4.7	4.4	2.9	2.7	3.9
u04g	3.7	3.3	4.2	4.7	4.4	2.9	2.7	3.9
u06g	3.7	3.3	4.2	4.7	<b>4.5</b>	2.9	2.7	3.9
u08g	3.7	3.3	<b>4.3</b>	<b>4.8</b>	4.6	2.9	2.7	3.9
u12g	3.7	<b>3.4</b>	4.6	5.0	4.9	<b>3.0</b>	<b>2.8</b>	<b>4.1</b>
u16g	<b>3.8</b>	3.5	4.9	5.3	5.3	3.1	2.8	4.3
u24g	4.0	3.7	5.7	5.9	6.1	3.4	3.0	4.8
u32g	4.2	4.0	6.3	6.3	6.8	3.7	3.1	5.2
u48g	4.9	4.6	7.3	6.8	7.6	4.0	3.3	5.9
u96g	5.5	6.1	10.3	8.1	9.2	4.3	3.5	7.4

the values up to the bold value in each band remained the same at 0.1 TECU level

From Table 2.6 and Table 2.7, a time resolution of 1 hour or higher (uqrg, u02g, u03g and u04g GIMs in this study) keep the accuracy of high-rate GIM (15 minutes) at 0.1 TECU level. And the high-rate GIM (15 minutes), uqrg, is one of the most accurate GIM. As shown in Table 2.3, the lower accuracy of GIMs with full temporal resolution (2 or 5 minutes) might be related to the uneven distribution of ionospheric observations, the weight between predicted GIMs and real-time observations. The performance of real-time GIMs with the full temporal resolution is slightly worse than 20 minutes real-time GIMs. Furthermore, the full temporal resolution real-time GIM is even worse than the GIM obtained by linear interpolation of the 20minutes real-time GIM in a sun-fixed reference frame. This might be related to the low number and sparse distribution of ionospheric observations at short timescales. In this regard, it would be better to find a more suitable temporal resolution for the generation of GIM in the sun-fixed reference frame.



Table 2.7 RMS of dSTEC assessment in TECUs with 59 global distributed receivers during four days in 2015: 082, 146, 280, 330, in TECUs.

GIM	-60°	-40°	-20°	0°	20°	40°	60°	Overall
uqrg	3.00	3.60	5.69	6.91	5.61	2.42	2.16	4.25
u02g	2.97	3.59	5.71	6.88	5.62	2.42	2.15	4.25
u03g	2.96	3.60	5.76	<b>7.00</b>	5.67	2.45	2.16	4.29
u04g	2.98	3.66	<b>5.90</b>	7.03	<b>5.76</b>	2.49	2.19	<b>4.36</b>
u06g	<b>3.09</b>	<b>3.80</b>	6.25	7.47	6.14	<b>2.67</b>	<b>2.25</b>	4.62
u08g	3.24	4.07	6.83	7.81	6.60	2.90	2.38	4.96
u12g	3.73	4.88	8.07	9.10	7.97	3.51	2.57	5.89
u16g	4.22	5.67	9.08	10.23	9.23	4.11	2.80	6.73
u24g	4.70	6.68	10.65	12.68	11.22	5.16	3.20	8.14
u32g	5.48	8.26	12.23	14.85	13.37	5.97	3.70	9.56
u48g	6.57	10.18	13.72	15.66	14.59	6.46	3.91	10.47
u96g	7.77	11.25	18.75	18.97	17.30	7.44	4.49	12.80

The values showing a first increase of 0.1 TECU in the RMS in each given latitudinal band are presented in bold.

## 2.4 GIM applications on space weather monitoring

Space weather events including ionospheric perturbations and ionospheric storms might affect high-frequency communications and GNSS positioning which are closely related to our daily life. In addition, the ionospheric perturbations with high spatial and temporal components of VTEC gradient might also enlarge GNSS positioning errors and even incapacitate Satellite-Based Augmentation System (SBAS) and Ground-Based Augmentation System (GBAS) services. The ionospheric storms have adverse effects on the radio communications, satellite communications and also on the GNSS applications. It is important to monitor the ionospheric conditions during space weather events for the purpose of allowing users to assess the impact of space weather events (Buonsanto, 1999; Jakowski and Hoque, 2019; Nishioka et al., 2017). UQRG is derived from GNSS carrier phase measurements assuming a two-layer tomographic TEC model and interpolated by Kriging technique with a spatial resolution of 5° and 2.5° in longitude and latitude, respectively. The temporal resolution of UQRG is 15 minutes (Orús et al., 2005). And UQRG is one of the most accurate GIM, which can provide global realistic VTEC distribution even in polar regions where few GNSS receivers are installed (Hernández-Pajares et al., 2020).

In order to characterize ionospheric storms and spatial and temporal components of VTEC gradient on a global scale, UQRG with reliable VTEC distribution is selected for a new

ionospheric storm scale and a new way of estimating the spatial and temporal components of the VTEC gradient.

### 2.4.1 Spatial and temporal components of VTEC gradient

In order to obtain full (non-relative) values of TEC spatial gradients and temporal variations separately, the Regional VTEC spatial Gradient indices based on UQRG (RVGU) and Regional Ionospheric Disturbance index based on UQRG (RIDU) are proposed to estimate regional ionospheric perturbation degree over selected regions. In addition, the spatial and temporal components of VTEC at grid points of UQRG on a global scale are also introduced (Liu et al., 2022).

The level of regional VTEC spatial gradients during a quiet ionospheric state over Europe region (40°N-70°N, 20°W-40°E) from 20 May to 25 May of 2015 in Figure 2.6 can be regarded as a reference.  $\nabla V_x$  and  $\nabla V_y$  are the zonal and meridional component of VTEC spatial gradient at grid point.  $\nabla V$  is the module of  $\nabla V_x$  and  $\nabla V_y$ .  $\bar{\nabla V}$  is the average of  $\nabla V_{i,j}$  over the selected region.  $\sigma_{\nabla V}$  is the standard deviation of VTEC spatial gradient over the selected region. The  $\nabla V_{P_{95}}$  is the 95th percentile value of  $\nabla V_{i,j}$  over the selected region.  $\nabla V_{x,P_{95+}}$  and  $\nabla V_{x,P_{95-}}$  represent 95th percentiles of positive VTEC spatial gradient values (eastward) and negative VTEC spatial gradient values (westward), respectively. And  $\nabla V_{y,P_{95+}}$  and  $\nabla V_{y,P_{95-}}$  represent 95th percentiles of positive VTEC spatial gradient values (northward) and negative VTEC spatial gradient values (southward), respectively.

As shown in Figure 2.6, the VTEC spatial gradient indices, RVGU, range from around -10 to 10 during the quiet ionospheric state from 20 May to 25 May of 2015. Compared with quiet ionospheric state of Figure 2.6, the VTEC spatial gradient indices are able to capture the variations of VTEC spatial gradient during the disturbed ionospheric state. In Figure 2.7 and Figure 2.8, the  $\nabla V_{P_{95}}$ ,  $\nabla V_{x,P_{95\pm}}$  and  $\nabla V_{y,P_{95\pm}}$  are more sensitive than other regional indices ( $\bar{\nabla V}$ ,  $\sigma_{\nabla V}$ ,  $\bar{\nabla V}_x$ ,  $\bar{\nabla V}_y$ ) during these two severe geomagnetic storms in Europe.

The global map of VTEC spatial and temporal gradients of UQRG can be derived at each grid point. Compared with the previous quiet day (16 March 2015), the high southward VTEC gradients at Europe (40°N-70°N, 20°W-40°E) and the high VTEC gradients of zonal, meridional, and temporal components around grid point [75°S, 60°W] on 18 UT of 17 March 2015 are obvious in Figure 2.9(b), Figure 2.9(d) Figure 2.9(f).

As it can be seen in Figure 2.10, the regional index of VTEC temporal variation, RIDU, has a rapid increase during the very strong X-17.0 class solar flare on 28 October 2003. Nevertheless, the RIDU values are not sensitive to solar flares weaker than the one shown in Figure 2.10, due to the intrinsic temporal resolution of the GIMs (15 minutes). The smaller RIDU values are related to the temporal resolution of UQRG. Currently, the performance of

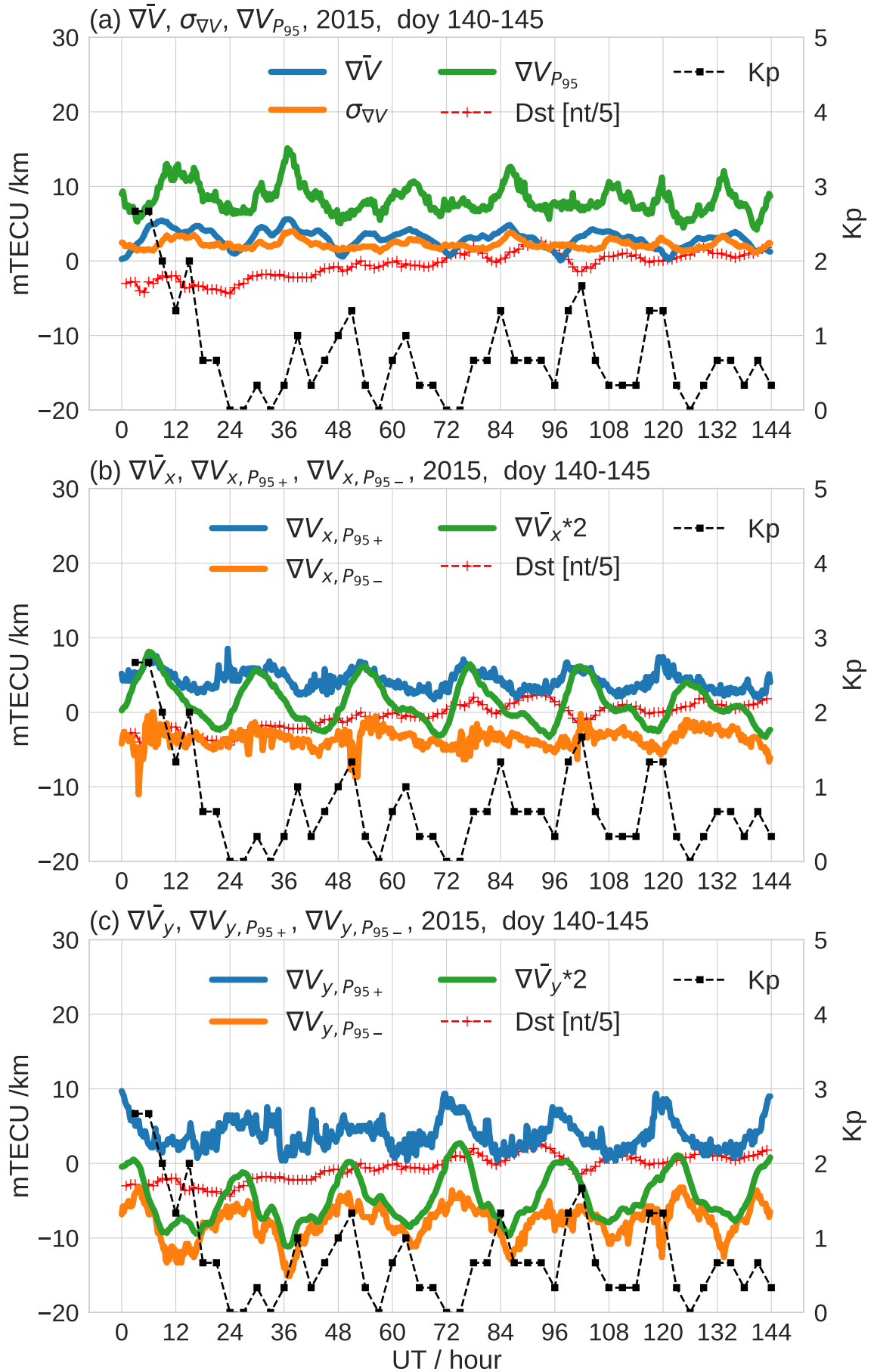


Figure 2.6 The evolution of RVGU at Europe (40°N-70°N, 20°W-40°E) during the geomagnetic quiet period 20-25 May 2015.

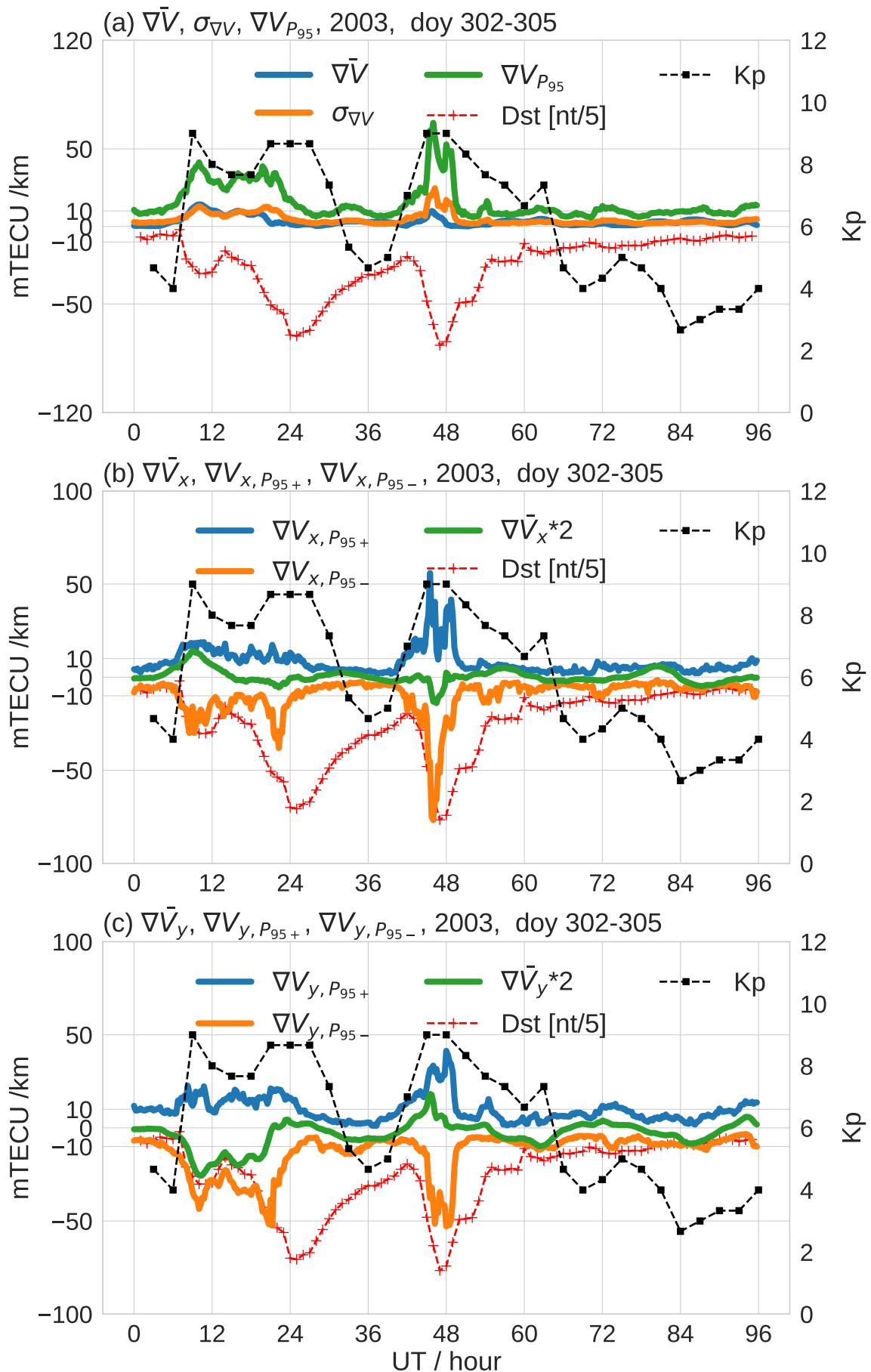


Figure 2.7 The evolution of RVGU at Europe ( $40^{\circ}\text{N}$ - $70^{\circ}\text{N}$ ,  $20^{\circ}\text{W}$ - $40^{\circ}\text{E}$ ) during the Halloween storm 28 October to 1 November 2003.

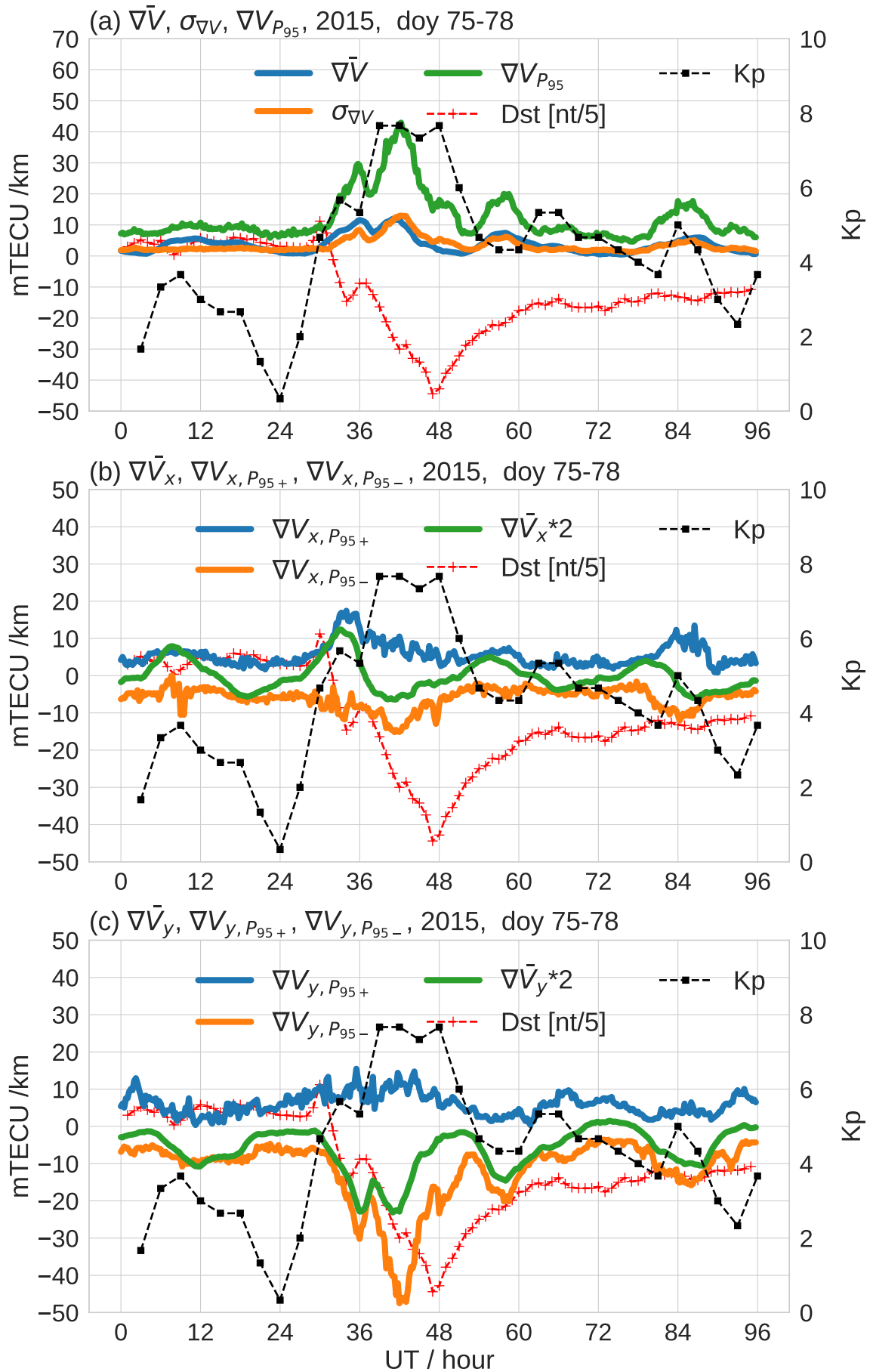


Figure 2.8 The evolution of RVGU at Europe (40°N-70°N, 20°W-40°E) during the St. Patrick's Day storm 16-20 March 2015.

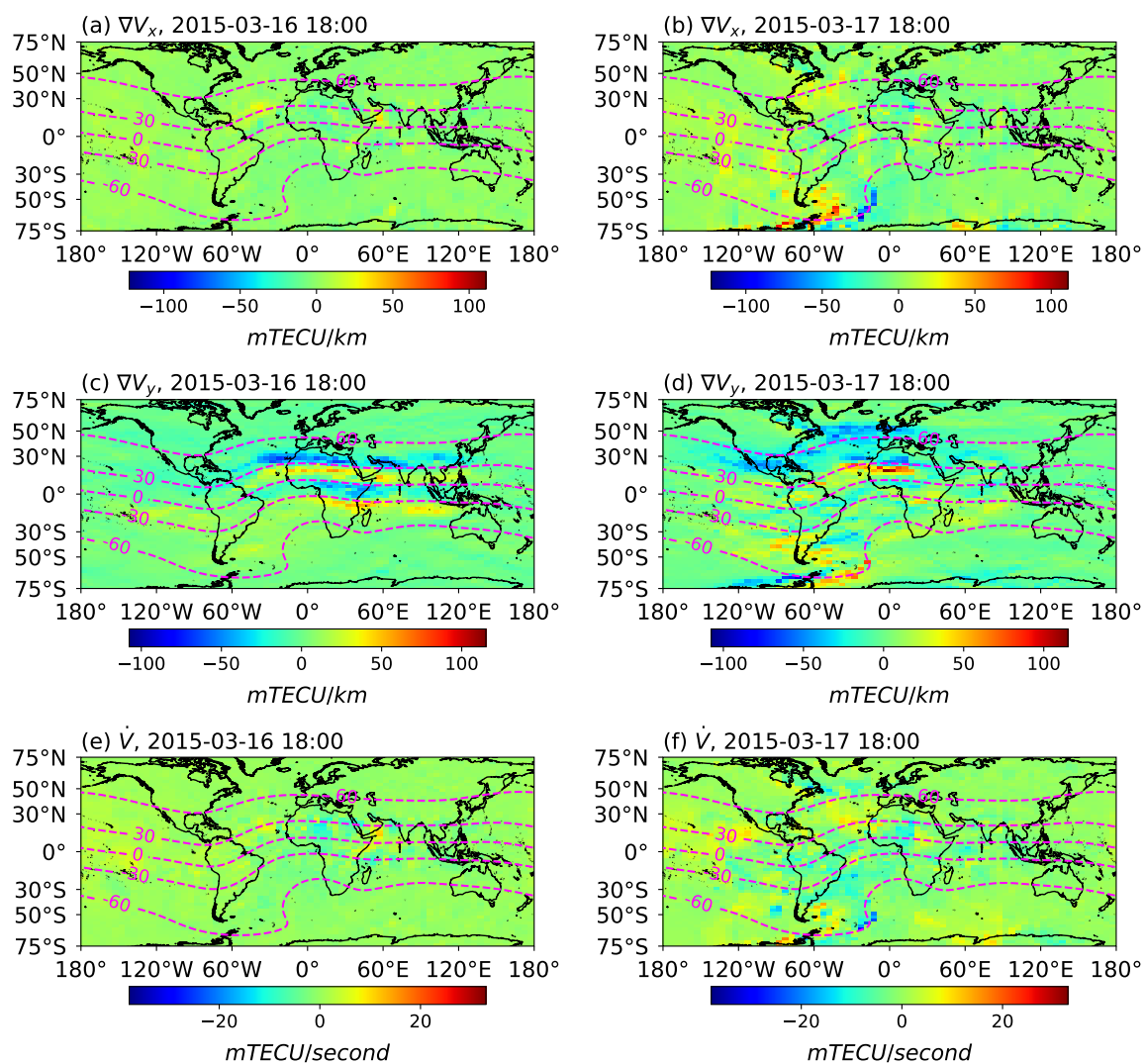


Figure 2.9 The global map of  $\nabla V_x$ ,  $\nabla V_y$  and  $\dot{V}_{i,j}$  for a latitudinal range of  $[-75^\circ, 75^\circ]$  on 18 UT of 16-17 March 2015. The magenta dashed lines represent for the geomagnetic dip angles.

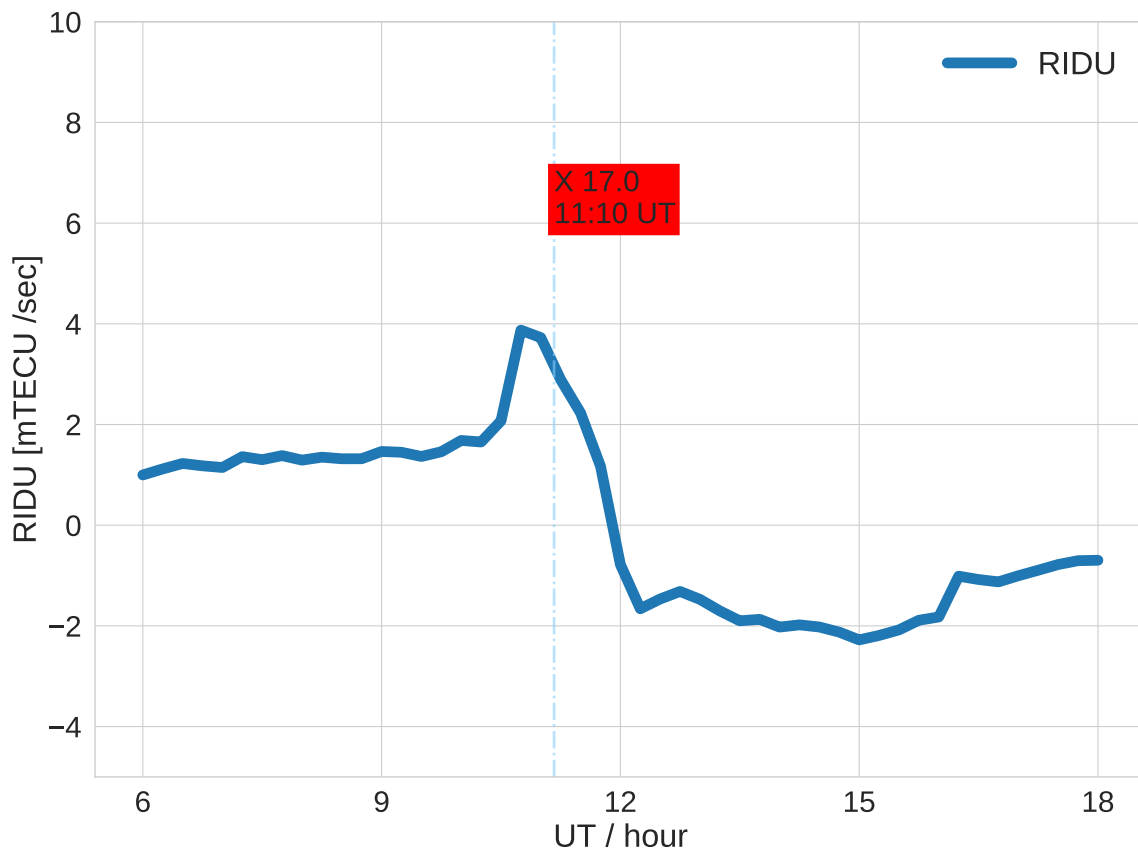


Figure 2.10 The evolution of RIDU at Europe ( $40^{\circ}\text{N}$ - $70^{\circ}\text{N}$ ,  $20^{\circ}\text{W}$ - $40^{\circ}\text{E}$ ) on 28 October 2003 when a strong X-17.0 solar flare happened.

RIDU is subject to the GIM time resolution. And this is related to the 15-minute temporal resolution of UQRG. The UQRG can hardly capture the temporal variation of VTEC at shorter time scales. Besides spatial gradients, rapid temporal changes of the ionospheric ionization may also cause problems in navigation and positioning. Thus, the availability of a separate index describing the strength of sudden ionospheric disturbances would be useful for estimating risks concerning safety and accuracy in the navigation and positioning applications of GNSS. And since the temporal resolution might be improved in the future, the corresponding improvement of RIDU resolution can be anticipated by the future upgrades of the GIM.

### 2.4.2 Ionospheric storms

Ionospheric storms are composed of a positive phase with increased TEC and a negative phase with decreased TEC. To remove the dependence of VTEC variations on the season,

Table 2.8 The definition and occurrence probability of IsUG derived from UQRG during the period 1997-2014.

IsUG	Description	Definition	Probability on a global scale (%)
IP3	Severe positive storm	$5 < \hat{P}_{TEC}$	0.17
IP2	Strong positive storm	$3 < \hat{P}_{TEC} \leq 5$	0.72
IP1	Moderate positive storm	$1 < \hat{P}_{TEC} \leq 3$	12.43
I0	Quiet	$-1 < \hat{P}_{TEC} \leq 1$	73.96
IN1	Moderate negative storm	$-2 < \hat{P}_{TEC} \leq -1$	11.72
IN2	Strong negative storm	$-3 < \hat{P}_{TEC} \leq -2$	0.95
IN3	Severe negative storm	$\hat{P}_{TEC} < -3$	0.06

local time, and geographical location on a global scale, percentage deviations of hourly median VTEC extracted at each grid point of historical UQRG (from 1997 to 2014) are normalized (subtract the mean and divide by the corresponding standard deviation). The normalized percentage deviations of hourly median VTEC is denoted as  $\hat{P}_{TEC}$  (Liu et al., 2021b). As summarized in Table 2.8, the definitions of the proposed ionospheric storm scale based on UQRG are given in the first, second, and third columns, for different ionospheric states. And corresponding occurrence probability found on a global scale is provided in the fourth column.

The reported TEC enhancement in previous studies (Maruyama, 2006; Maruyama et al., 2013; Nishioka et al., 2017) starting from 23 UT of 7 November 2004 at [130°E, 30°N] (Japan) is coincident with the evolution of severe ionospheric positive storm ( $\hat{P}_{TEC} > 5$ ) at [130°E, 30°N] in Figure 2.11(a) and Figure 2.11(b). Coincident with the increase of  $\hat{P}_{TEC}$  the right bottom corner (77.9°S, 166.8°E) of Figure 2.11(c) and Figure 2.11(d), strong TEC enhancement was found in a GNSS station (77.9°S, 166.8°E) located at Antarctica (Sulaiman et al., 2007).

The level of ionospheric positive storm ( $\hat{P}_{TEC}$ ) started to increase since 14 UT and gradually expanded toward low latitude of Europe in panels (a)-(f) of Figure 2.12. The evolution of  $\hat{P}_{TEC}$  of Europe in panels (a)-(f) of Figure 2.12 is consistent with the reported TEC variation (Sori et al., 2019).



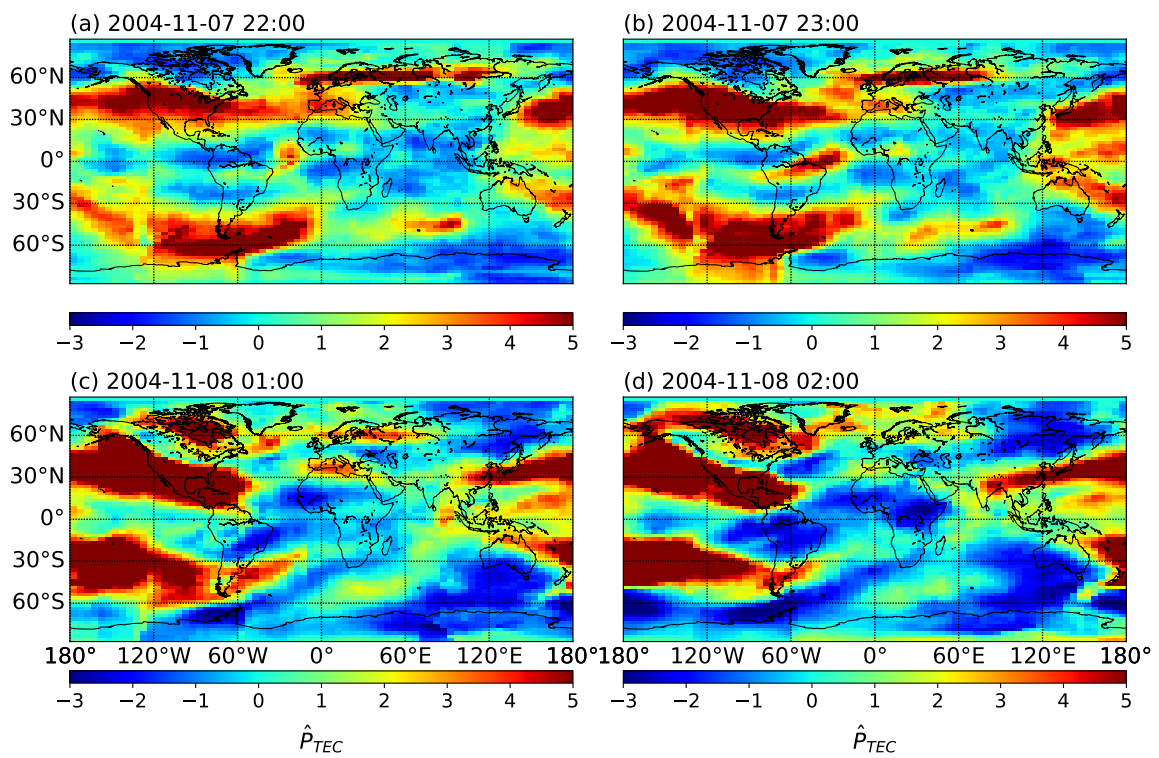


Figure 2.11 The IsUG global map of 7, 8 November in 2004.

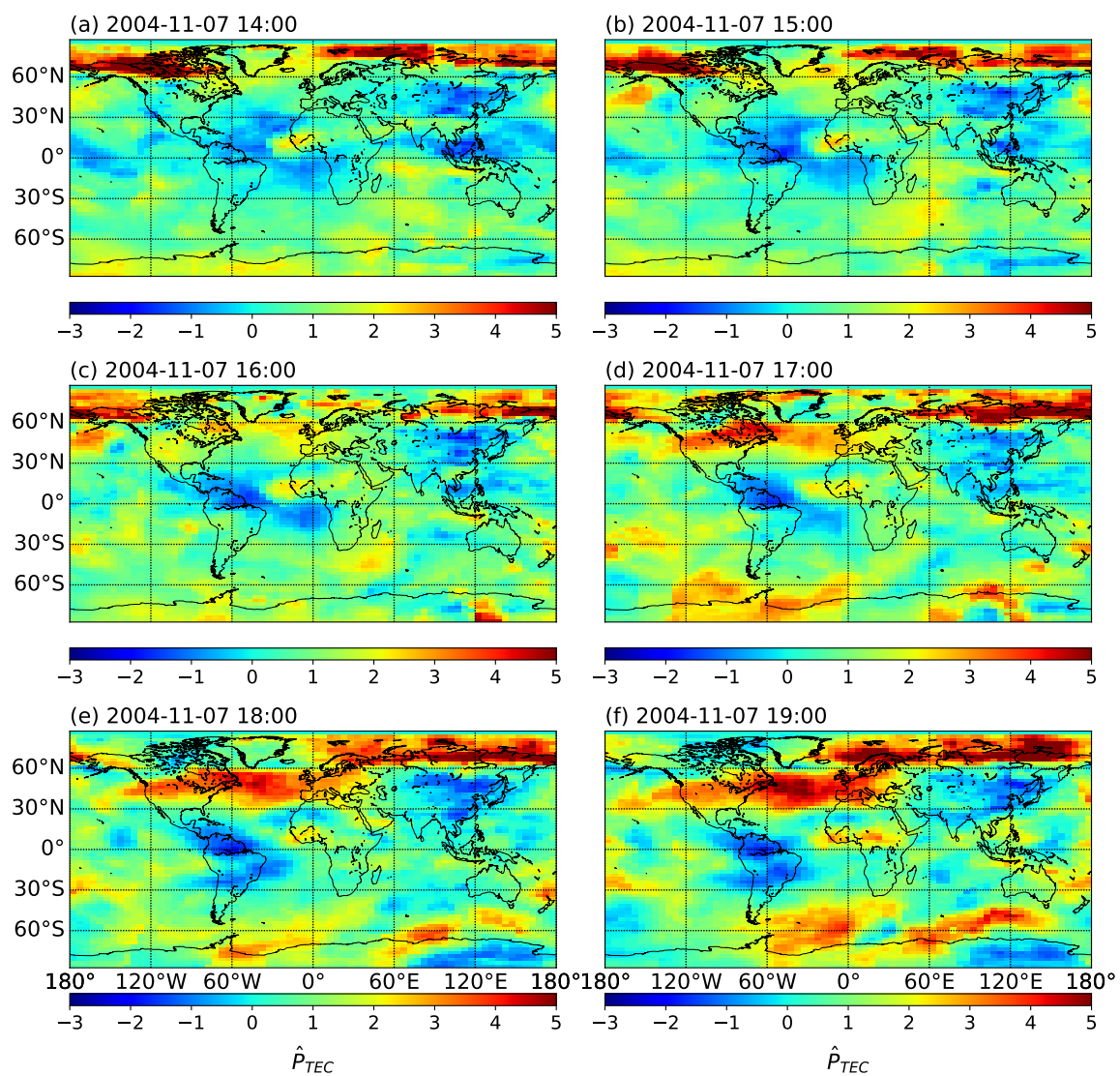


Figure 2.12 The IsUG global map from 14:00 to 19:00 UTC of 7 November in 2004.

# Chapter 3

## Quality Indexes

This chapter is aimed at providing evidence of the quality of the research developed in the context of this Ph.D. study. The work supporting this thesis has been presented to a number of peer-reviewed journals, where experts have provided valuable comments that have improved the quality and clarity of the research. The list of papers can be found in the following section.

### 3.1 Peer-reviewed Journals

- Liu, Q., Hernández-Pajares, M., Yang, H., Monte-Moreno, E., Roma-Dollase, D., García-Rigo, A., Li, Z., Wang, N., Laurichesse, D., Blot, A., Zhao, Q., Zhang, Q., Hauschild, A., Agrotis, L., Schmitz, M., Wübbena, G., Stürze, A., Krankowski, A., Schaer, S., Feltens, J., Komjathy, A., and Ghoddousi-Fard, R. (2021c). The cooperative IGS RT-GIMs: a reliable estimation of the global ionospheric electron content distribution in real time. *Earth System Science Data*, 13(9):4567–4582
- Liu, Q., Hernández-Pajares, M., Lyu, H., and Goss, A. (2021a). Influence of temporal resolution on the performance of global ionospheric maps. *Journal of Geodesy*, 95(34):34
- Liu, Q., Hernández-Pajares, M., Yang, H., Monte-Moreno, E., García-Rigo, A., Lyu, H., Olivares-Pulido, G., and Raül, O.-P. (2022). A new way of estimating the spatial and temporal components of the Vertical Total Electron Content gradient based on UPC-IonSAT Global Ionosphere Maps. *Space Weather*, 20(2):e2021SW002926
- Liu, Q., Hernández-Pajares, M., Lyu, H., Nishioka, M., Yang, H., Monte-Moreno, E., Gulyaeva, T., Béniguel, Y., Wilken, V., Olivares-Pulido, G., and Raül, O.-P. (2021b).

Ionospheric Storm Scale Index Based on High Time Resolution UPC-IonSAT Global Ionospheric Maps (IsUG). *Space Weather*, 19(11):e2021SW002853

The importance of each journal where the research has been published is proven in Table 3.1, by means of presenting the latest Impact Factor (IF) and quartile available at the time of writing this dissertation, according to Thomson Reuters. As we can see, all the previous listed journals are in the first quartile (Q1).

Journal	ISSN	Quartile	Impact Factor	5 year Impact Factor
Journal of Geodesy	0949-7714	Q1	4.260	4.781
Space Weather	1542-7390	Q1	4.456	4.267
Earth System Science Data	1866-3508	Q1	11.333	11.909

Table 3.1 Journal information and ranking in its category based on the IF.

# Chapter 4

## Conclusions and future work

The present chapter brings together the conclusions achieved in this dissertation. In addition, future research work is explained.

### 4.1 Conclusions

The first contribution shown in Chapter 2 is to connect GIM assessment methods in post-processing and real-time mode. The three common GIM assessment methods (Jason-altimeter VTEC assessment, dSTEC assessment, RT-dSTEC assessment) can be used according to different purposes. Mostly, the RT-dSTEC assessment related to dSTEC assessment, is used for the validation and combination of real-time GIMs also in real-time. In post-processing mode, Jason-altimeter VTEC assessment, and dSTEC assessment are able to evaluate the performance of GIMs over oceans and continental regions, respectively. The Jason-altimeter VTEC assessment and dSTEC assessment are independent and consistent for GIM evaluation. According to previous studies, UQRG is one of the best GIM both in Jason-altimeter VTEC assessment and dSTEC assessment. Therefore, the global VTEC from UQRG is reliable and can be used for ionospheric monitoring.

The second contribution is to combine different real-time GIMs of IGS centers by means of RT-dSTEC assessment in real-time mode. As shown in the results of Jason-altimeter VTEC assessment and dSTEC assessment in post-processing mode, the performance of IGS real-time GIMs is close to IGS post-processed GIMs. And results of the RT-dSTEC assessment are consistent with dSTEC assessment. In this regard, the IGS real-time GIMs can be reliable sources of real-time global VTEC information and have great potential for real-time applications including range error correction for transionospheric radio signals, the monitoring of space weather on a global scale among others.

The third contribution is to study the behavior of downsampled UQRG with different time resolutions (ranges from 15 minutes to 24 hours) during 1.5 solar cycles. In the Jason- altimeter VTEC assessment, the standard deviation of the difference between GIM-VTEC and Jason-VTEC is subject to the variation of geomagnetic activity when the solar activity is high. The variation of standard deviation appears to be intense under high geomagnetic activity. It turns out that the accuracy of GIM with time resolution lower than 1 hour can be degraded. Accordingly, high time resolution (including 15, 30, 45, and 60 minutes) is recommended for GIM generation.

The fourth contribution is to introduce the new gradient indices including RVGU, RIDU, and the spatial and temporal components of VTEC at grid points of UQRG on a global scale. Compared with previous studies, the new VTEC gradient indices based on UQRG, VgUG, are able to capture the variations of VTEC spatial and temporal gradient during the disturbed ionospheric state. The regional gradient indices based on UQRG open a new way to estimate the ionospheric perturbation degree at regions where few GNSS receivers are available. And the spatial and temporal components of the VTEC gradient at each grid point of UQRG allow the representation of ionospheric perturbations on a global scale.

The fifth contribution is to propose a new ionospheric storm scale based on UQRG which is reliable and suitable for ionospheric representation which has been demonstrated in previous studies. The IsUG global maps are consistent with previous studies during the severe geomagnetic storm focusing on the regions of Japan, Antarctica, and Europe. IsUG global map has a great potential for the scientific study of ionospheric storms from a global perspective and also for space weather warnings considering the recently developed real-time GIMs.

## 4.2 Future work

The future work might include following:

- Real-time GIM: The dissemination of real-time RMS maps and high-temporal-resolution real-time GIMs with high accuracy can be useful for the positioning users. In addition, higher maximum spherical harmonic degrees might be adopted to increase the accuracy and spatial resolution of broadcasted real-time GIMs. With the growth of real-time GNSS receivers, the dSTEC weighting might be improved by replacing the “internal” with the “external” receivers (i.e., not used by any real-time analysis centers).
- Spatial and temporal components of VTEC gradient: With the newly developed real-time GIMs, the possibility and reliability of monitoring the ionospheric perturbation

degree can be investigated in real-time. The resolution of GIM might be improved by the better coverage station and multi-GNSS measurements (not just GPS).

- Ionospheric storm: Since the IGS real-time GIMs are available and the accuracy of real-time GIMs is presently close to the accuracy of the UQRG, the generation of real-time IsUG might be the next step. In addition, the real-time ionospheric storm warning system based on real-time IsUG might be also available for space weather monitoring.





# Chapter 5

## Publications

The present chapter includes a copy of three published papers of the compendium and one extra published paper in peer-reviewed journals realized in the context of this Ph.D. study. Three published papers that form the compendium of articles are:

- The cooperative IGS RT-GIMs: a reliable estimation of the global ionospheric electron content distribution in real time.
- Influence of temporal resolution on the performance of global ionospheric maps.
- A new way of estimating the spatial and temporal components of the Vertical Total Electron Content gradient based on UPC-IonSAT Global Ionosphere Maps.

And the extra published paper is:

- Ionospheric Storm Scale Index Based on High Time Resolution UPC-IonSAT Global Ionospheric Maps (IsUG)



# The cooperative IGS RT-GIMs: a reliable estimation of the global ionospheric electron content distribution in real time

Qi Liu<sup>1</sup>, Manuel Hernández-Pajares<sup>1,2</sup>, Heng Yang<sup>3,1</sup>, Enric Monte-Moreno<sup>4</sup>, David Roma-Dollase<sup>2</sup>, Alberto García-Rigo<sup>1,2</sup>, Zishen Li<sup>5</sup>, Ningbo Wang<sup>5</sup>, Denis Laurichesse<sup>6</sup>, Alexis Blot<sup>6</sup>, Qile Zhao<sup>7,8</sup>, Qiang Zhang<sup>7</sup>, André Hauschild<sup>9</sup>, Loukis Agrotis<sup>10</sup>, Martin Schmitz<sup>11</sup>, Gerhard Wübbena<sup>11</sup>, Andrea Stürze<sup>12</sup>, Andrzej Krankowski<sup>13</sup>, Stefan Schaer<sup>14,15</sup>, Joachim Feltens<sup>16</sup>, Attila Komjathy<sup>17</sup>, and Reza Ghoddousi-Fard<sup>18</sup>

<sup>1</sup>Department of Mathematics, Universitat Politècnica de Catalunya (UPC-IonSAT), Barcelona, Spain

<sup>2</sup>Institut d'Estudis Espacials de Catalunya (IEEC), Barcelona, Spain

<sup>3</sup>School of Electronic Information and Engineering, Yangtze Normal University, 408100 Chongqing, China

<sup>4</sup>Department of Signal Theory and Communications, TALP, Universitat Politècnica de Catalunya, 08034 Barcelona, Spain

<sup>5</sup>Aerospace Information Research Institute (AIR), Chinese Academy of Sciences (CAS), Beijing, China

<sup>6</sup>Centre National d'Etudes Spatiales, Toulouse, France

<sup>7</sup>GNSS Research Center, Wuhan University, No. 129 Luoyu Road, Wuhan 430079, China

<sup>8</sup>Collaborative Innovation Center of Earth and Space Science, Wuhan University, No. 129 Luoyu Road, Wuhan 430079, China

<sup>9</sup>German Aerospace Center (DLR), German Space Operations Center (GSOC), 82234 Weßling, Germany

<sup>10</sup>European Space Operations Center, European Space Agency, Darmstadt, Germany

<sup>11</sup>Geo++ GmbH, Steinriede 8, 30827 Garbsen, Germany

<sup>12</sup>BKG, Federal Agency for Cartography and Geodesy, Frankfurt, Germany

<sup>13</sup>Space Radio-Diagnostics Research Centre, University of Warmia and Mazury in Olsztyn, 10-719 Olsztyn, Poland

<sup>14</sup>Astronomical Institute, the University of Bern, Sidlerstrasse 5, Bern 3012, Switzerland

<sup>15</sup>Federal Office of Topography (swisstopo), Wabern, Switzerland

<sup>16</sup>Navigation Support Office, Telespazio Germany GmbH c/o European Space Agency/European Space Operations Centre, Robert-Bosch-Straße 5, 64293 Darmstadt, Germany

<sup>17</sup>Near Earth Tracking Systems Group (335S), NASA – Jet Propulsion Laboratory, California Institute of Technology, 4800 Oak Grove Drive, M/S 138-317, Pasadena, CA 91109, USA

<sup>18</sup>Canadian Geodetic Survey, Natural Resources Canada, Ottawa, Canada

**Correspondence:** Manuel Hernández-Pajares (manuel.hernandez@upc.edu)

Received: 22 April 2021 – Discussion started: 4 May 2021

Revised: 17 July 2021 – Accepted: 19 August 2021 – Published: 23 September 2021

**Abstract.** The Real-Time Working Group (RTWG) of the International GNSS Service (IGS) is dedicated to providing high-quality data and high-accuracy products for Global Navigation Satellite System (GNSS) positioning, navigation, timing and Earth observations. As one part of real-time products, the IGS combined Real-Time Global Ionosphere Map (RT-GIM) has been generated by the real-time weighting of the RT-GIMs from IGS real-time ionosphere centers including the Chinese Academy of Sciences (CAS), Centre National d'Etudes Spatiales (CNES), Universitat Politècnica de Catalunya (UPC) and Wuhan University (WHU). The performance of global vertical total electron content (VTEC) representation in all of the RT-GIMs has been assessed by VTEC from Jason-3 altimeter for 3 months over oceans and dSTEC-GPS technique with 2 d observations over

continental regions. According to the Jason-3 VTEC and dSTEC-GPS assessment, the real-time weighting technique is sensitive to the accuracy of RT-GIMs. Compared with the performance of post-processed rapid global ionosphere maps (GIMs) and IGS combined final GIM (igsg) during the testing period, the accuracy of UPC RT-GIM (after the improvement of the interpolation technique) and IGS combined RT-GIM (IRTG) is equivalent to the rapid GIMs and reaches around 2.7 and 3.0 TECU (TEC unit,  $10^{16} \text{ e l m}^{-2}$ ) over oceans and continental regions, respectively. The accuracy of CAS RT-GIM and CNES RT-GIM is slightly worse than the rapid GIMs, while WHU RT-GIM requires a further upgrade to obtain similar performance. In addition, a strong response to the recent geomagnetic storms has been found in the global electron content (GEC) of IGS RT-GIMs (especially UPC RT-GIM and IGS combined RT-GIM). The IGS RT-GIMs turn out to be reliable sources of real-time global VTEC information and have great potential for real-time applications including range error correction for transionospheric radio signals, the monitoring of space weather, and detection of natural hazards on a global scale. All the IGS combined RT-GIMs generated and analyzed during the testing period are available at <https://doi.org/10.5281/zenodo.5042622> (Liu et al., 2021b).

## 1 Introduction

The global ionosphere maps (GIMs), containing vertical total electron content (VTEC) information at given grid points (typically with a spatial resolution of  $2.5^\circ$  in latitude and  $5^\circ$  in longitude), have been widely used in both scientific and technological communities (Hernández-Pajares et al., 2009). Due to the high quality and global distribution of VTEC estimation, GIM has been applied to investigating the behavior of the ionosphere, such as the climatology of mean total electron content (TEC), potential ionospheric anomalies before earthquakes, semiannual variations in TEC in the ionosphere, the VTEC structure of the polar ionosphere under different cases and W index for ionospheric disturbance warning (e.g., Liu et al., 2009, 2006; Zhao et al., 2007; Jiang et al., 2019; Hernández-Pajares et al., 2020; Gulyaeva and Stanislawski, 2008; Gulyaeva et al., 2013). In addition, the high accuracy of GIM enables precise range corrections for transionospheric radio signals including radar altimetry, radio telescopes and Global Navigation Satellite System (GNSS) positioning (e.g., Komjathy and Born, 1999; Fernandes et al., 2014; Sotomayor-Beltran et al., 2013; Le and Tiberius, 2007; Zhang et al., 2013a; Lou et al., 2016; Chen et al., 2020). The Center for Orbit Determination in Europe (CODE), European Space Agency (ESA), Jet Propulsion Laboratory (JPL), Canadian Geodetic Survey of Natural Resources Canada (NRCan) and Universitat Politècnica de Catalunya (UPC) agreed on the computation of individual GIMs in IONosphere map EXchange (IONEX) format and created the Ionosphere Working Group (Iono-WG) of the International GNSS Service (IGS) in 1998 (Schaer et al., 1996, 1998; Feltens and Schaer, 1998; Feltens, 2007; Mannucci et al., 1998; Hernández-Pajares et al., 1998, 1999). In the IGS 2015 workshop, the Chinese Academy of Sciences (CAS) and Wuhan University (WHU) became new Ionospheric Associate Analysis Centers (IAACs) (Li et al., 2015; Ghoddousi-Fard, 2014; Zhang et al., 2013b). Currently, there are three types of post-processed IGS GIMs at different latencies:

final, rapid and predicted GIMs. With the contribution from different IAACs, the final and rapid GIMs are assessed and combined by corresponding weights and uploaded to File Transfer Protocol (FTP) or Hypertext Transfer Protocol (HTTP) servers with the latency of 1–2 weeks and 1–2 d, respectively. The 1 and 2 d predicted GIMs can provide valuable VTEC information in advance for ionospheric activities and corrections. However, the accuracy of predicted GIMs is limited due to the nonlinear variation in ionosphere and the lack of real-time ionospheric observations (Hernández-Pajares et al., 2009; García-Rigo et al., 2011; Li et al., 2018).

In order to satisfy the growing demand for real-time GNSS positioning and applications, the Real-Time Working Group (RTWG) of IGS was established in 2001 and officially started to provide real-time service (RTS) in 2013 (Caissy et al., 2012; Elsobeiey and Al-Harbi, 2016). Aside from multi-GNSS real-time data streams, the IGS-RTS also generates RT-GNSS product streams, including satellite orbits, clocks, code/phase biases and GIM. These high-quality IGS-RTS products enable precise GNSS positioning, navigation, timing (PNT), ionosphere monitoring and hazard detection. In the Radio Technical Commission for Maritime Services (RTCM) Special Committee (SC-104), the State Space Representation (SSR) correction data format is defined as the standard message (RTCM-SSR) for real-time GNSS applications. In support of flexible multi-GNSS applications within current multi-constellation and multi-frequency environments, a new format (IGS-SSR) is developed. The dissemination of IGS Real-Time Global Ionosphere Maps (RT-GIMs) adopts spherical harmonic expansion to save the bandwidth in both RTCM-SSR and IGS-SSR formats (RTCM-SC, 2014; IGS, 2020).

The accuracy of RT-GIMs is typically worse than post-processed GIMs due to the short span of ionospheric observations, sparse distribution of stations, higher noises in carrier-to-code leveling, or difficulty in carrier ambiguity estimation in real-time processing mode. While RT-GIMs perform slightly worse than post-processed GIMs, it is found

that RT-GIMs are helpful to reduce the convergence time of dual-frequency precise point positioning (PPP), and they strengthen the solution (Li et al., 2013). With the corrections of RT-GIMs, the accuracy of single-frequency PPP reaches decimeter and meter level in horizontal and vertical directions (Ren et al., 2019), while the instantaneous (single-epoch) real-time kinematic (RTK) positioning over medium and long baselines is able to obtain a higher success rate of the ambiguity fixing and reliability for rover stations at a level of a few centimeters (Tomaszewski et al., 2020). In addition, the feasibility of ionospheric storm monitoring based on RT-GIMs is tested (García Rigo et al., 2017). A first fusion of IGS-GIMs and ionosonde data from the Global Ionosphere Radio Observatory (GIRO) paves the way for the improvement of real-time International Reference Ionosphere (Froñ et al., 2020). Currently, the routine RT-GIMs are available from CAS, Centre National d'Etudes Spatiales (CNES), German Aerospace Center in Neustrelitz (DLR-NZ), JPL, UPC, WHU and IONOLAB (Li et al., 2020; Laurichesse and Blot, 2015; Jakowski et al., 2011; Hoque et al., 2019; Komjathy et al., 2012; Roma Dollase et al., 2015; Sezen et al., 2013). Individual RT-GIMs from different IGS centers can be gathered from IGS-RTS by means of Network Transportation of RTCM by Internet Protocol (NTRIP) (Weber et al., 2007). With the contribution of IGS RT-GIMs from CAS, CNES and UPC, a first IGS real-time combination of GIMs was generated in 2018 (Roma-Dollase et al., 2018a).

Recently, one of the IGS RT-GIMs (UPC-IonSAT) has completely changed the real-time interpolation strategy, with a significant improvement. In addition, the number of contributing centers has been increased from three to four, thanks to the participation of Wuhan University. A new version of IGS combined RT-GIM (IRTG) has been developed to improve the performance and also adapt to the newly updated IGS-SSR format. In addition, the developed software has been further parallelized to decrease the latency of IRTG computation to a few minutes (Tange, 2011). This paper summarizes the computation methods of IGS RT-GIMs from different ionosphere centers and the generation of IRTG. In addition, the performance of different RT-GIMs and the real-time weighting technique is shown and discussed. The conclusions and future improvements are given in the final section.

## 2 Data and methods

### 2.1 Real-time GNSS data processing

In order to generate RT-GIMs, the real-time GNSS observations from worldwide stations are received and transformed into slant TEC (STEC). It should be noted that extraction of STEC in an unbiased way can be obtained by fitting an ionospheric model to the observations. With the global distributed STEC, different strategies are chosen for the computation of RT-GIMs.

Currently, two methods are commonly used for the calculation of real-time STEC. The first method is the so-called carrier-to-code leveling (CCL) as shown in Eq. (3) (Ciraolo et al., 2007; Zhang et al., 2019). The geometry-free (GF) combination of pseudorange and carrier phase observations is formed to extract STEC and differential code bias (DCB) in an unbiased way by fitting an ionospheric model (for example, spherical harmonic model). Due to the typically shorter phase-arc length in real-time mode, the impact of multipath and thermal noise is higher than in post-processing mode (Li et al., 2020).

$$P_{GF,t} \equiv P_{2,t} - P_{1,t} \\ = \alpha_{GF} \cdot \text{STEC}_t + c \cdot (D_r + D^s) + \epsilon_M + \epsilon_T \quad (1)$$

$$L_{GF,t} \equiv L_{1,t} - L_{2,t} = \alpha_{GF} \cdot \text{STEC}_t + B_{GF} \quad (2)$$

$$\tilde{P}_{GF,t} \equiv L_{GF,t} - \frac{1}{k} \sum_{i=1}^k (L_{GF,i} - P_{GF,i}) \\ \approx \alpha_{GF} \cdot \text{STEC}_t + c \cdot (D_r + D^s) \quad (3)$$

Here  $P_{1,t}$  and  $P_{2,t}$  are the pseudorange observations of epoch  $t$  at first and second frequencies, respectively.  $\alpha_{GF}$  can be approximated as  $40.3(\frac{1}{f_2} - \frac{1}{f_1})$ .  $f_1$  and  $f_2$  are the first and second frequencies of observation.  $\text{STEC}_t$  is the STEC of epoch  $t$ .  $r$  is receiver and  $s$  is satellite.  $c$  is the speed of light in vacuum.  $D_r$  and  $D^s$  are the receiver differential code biases (DCBs) and satellite DCB.  $\epsilon_M$  and  $\epsilon_T$  are the code multipath error and thermal noise error.  $L_{1,t}$  and  $L_{2,t}$  are the carrier phase observations including the priori corrections (such as wind-up term) of epoch  $t$  at first and second frequencies.  $B_{GF}$  equals  $B_1 - B_2$ , while  $B_1$  and  $B_2$  are the carrier phase ambiguities including the corresponding phase bias at first and second frequencies, respectively.  $k$  is the length of smoothing arc from beginning epoch to epoch  $t$ , and  $\tilde{P}_{GF,t}$  represents the smoothed  $P_{GF}$  of epoch  $t$ , which is significantly affected by the pseudorange multipath in real-time mode than in post-processing.

The second method is the GF combination of phase-only observations, and the  $B_{GF}$  is estimated together with the real-time TEC model (for example, described in terms of tomographic voxel-based basis functions) in Eq. (2) (Hernández-Pajares et al., 1997, 1999). Although the STEC from the second method is accurate and free of code multipath and thermal noise in post-processing, the convergence time can affect the accuracy of the STEC, most likely in the isolated receivers. In addition, the computation methods of RT-GIMs from different IGS real-time ionosphere centers were compared in detail at the next subsection and summarized in Table 1. Some ionosphere centers (CAS, CNES, WHU) directly estimate and disseminate spherical harmonic coefficients in a sun-fixed reference frame as Eq. (4) (RTCM-SC, 2014; Li et al., 2020), while UPC generates the RT-GIM in IONEX format and transforms RT-GIM into spherical harmonic co-

**Table 1.** The brief summary of different IGS RT-GIMs.

Agency/ GIM	Running date	Extra ionospheric information	DCB computation	GIM computation
CAS	Mid-2017 to present	2 d predicted GIM as back-ground information	Estimated at the same time with local VTEC, and corrected by 3 d aligned code bias	Observations with predicted GIMs generate 15° spherical harmonic expansion GIM in solar-geographic frame
CNES	End of 2014 to present (with an evolution of the spherical harmonic degree)	No	Expected in a forthcoming version	12° spherical harmonic expansion GIM which is generated in solar-geographic frame
UPC/URTG	6 Feb 2011 to 8 Sep 2019	1–2 d rapid GIM UQRG as background information	Optional	Tomographic model with kriging interpolation method and frozen rapid GIM (UQRG) as a priori model, which generates RT-GIM in sun-fixed geomagnetic frame
UPC/USRG	8 Sep 2019 to present	1–2 d rapid GIM UQRG as background information	Optional	Tomographic model with spherical harmonic interpolation method and frozen rapid GIM (UQRG) as a priori model, which generates RT-GIM in sun-fixed geomagnetic frame
UPC/UADG	4 Jan 2021 to present	Historical UQRG (since 1996) as databases	Optional	Tomographic model adopting atomic decomposition and LASSO solution for the global interpolation with the help of historical GIMs (UQRG), which generates GIM in sun-fixed geomagnetic frame
WHU	9 Nov 2020 to present	2 d predicted GIM as back-ground information	Directly use the previous satellite and receiver DCB estimated simultaneously with WHU rapid GIM	Observations with predicted GIMs yield 15° spherical harmonic expansion GIM in solar-geographic frame

efficients for the dissemination.

$$\left\{ \begin{array}{l}
 M_z = [1 - \sin^2 z / (1 + H_{\text{ion}} / R_E)^2]^{-\frac{1}{2}} \\
 \text{VTEC}_t = \text{STEC}_t / M_z \\
 \text{VTEC}_t = \sum_{n=0}^{N_{\text{SH}}} \sum_{m=0}^{\min(n, M_{\text{SH}})} P_{n,m}(\sin \varphi_I) \cdot (C_{n,m} \cos(m \lambda_{S,t}) + S_{n,m} \sin(m \lambda_{S,t})) \\
 \lambda_{S,t} = (\lambda_I + (t - t_0) \times \pi / 43\,200) \text{ modulo } 2\pi
 \end{array} \right. \quad (4)$$

Here  $z$  is the satellite zenith angle, and  $M_z$  is the mapping function between  $\text{STEC}_t$  and  $\text{VTEC}_t$ .  $H_{\text{ion}}$  is the height of the ionospheric single-layer assumption, and  $R_E$  is the radius of the earth.  $\text{VTEC}_t$  is the VTEC of epoch  $t$ .  $N_{\text{SH}}$  is the max degree of spherical harmonic expansion, and  $M_{\text{SH}}$  is the max order of spherical harmonic expansion.  $n$  and  $m$  are corresponding indices.  $P_{n,m}$  is the normalized associated Legendre functions.  $C_{n,m}$  and  $S_{n,m}$  are sine and cosine spherical harmonic coefficients.  $\varphi_I$  and  $\lambda_I$  are the geocentric latitude and longitude of ionospheric pierce point (IPP).  $\lambda_{S,t}$  is the mean sun fixed and phase-shifted longitude of IPP of epoch

$t$  (typically shifted by 2 h to approximate TEC maximum at 14:00 LT).  $t$  is the current epoch.  $t_0$  is a common reference of shifted hours, taken as 0 h in the present broadcasting of RT-GIM for WHU and 2 h for CAS, CNES and UPC.

## 2.2 The computation of RT-GIMs by different IGS real-time ionosphere centers

The strategies for generating RT-GIMs differ between IGS real-time ionospheric analysis centers (ACs). In this subsection, a brief introduction on the generation of RT-GIMs from individual ACs and the strategy comparison between different ACs are given.

### 2.2.1 Chinese Academy of Sciences

The post-processed GIM of CAS has been computed and uploaded to IGS since 2015 (Li et al., 2015). A predicting-plus-modeling approach is used by CAS for the computation of RT-GIM (Li et al., 2020). CAS RT-GIM is generated with multi-GNSS, GPS and GLONASS L1 + L2, BeiDou B1 + B2, and Galileo E1 + E5a real-time data streams,

provided by the IGS and regional GNSS tracking network stations. The real-time DCBs are estimated as part of the local ionospheric VTEC modeling using a generalized trigonometric series (GTS) function as Eq. (5). Then 3 d aligned biases are incorporated to increase the robustness of real-time DCBs (Wang et al., 2020).

$$\left\{ \begin{array}{l} \text{STEC}_t = M_z \cdot \text{VTEC}_t + c \cdot (D^s + D_r) \\ \text{VTEC}_t = \sum_{i=0}^{i_{\max}} \sum_{j=0}^{j_{\max}} \left\{ E_{i,j} \cdot \varphi_d^i \cdot \lambda_d^j \right\} \\ \quad + \sum_{l=0}^{l_{\max}} \{ C_l \cos(l \cdot h_t) + S_l \sin(l \cdot h_t) \} \\ h_t = 2\pi(t - 14)/T, \quad T = 24 \text{ h} \\ i_{\max} = j_{\max} = 2 \\ l_{\max} = 4 \end{array} \right. \quad (5)$$

Here  $r$  is receiver and  $s$  is satellite.  $\varphi_d$  and  $\lambda_d$  are the difference between IPP and station in latitude and longitude, respectively.  $i$ ,  $j$  and  $l$  represent the degrees in the polynomial model and Fourier series expansion.  $E_{i,j}$ ,  $C_l$  and  $S_l$  are unknown parameters.

The real-time STEC is computed by subtracting estimated DCB in Eq. (5) from  $\tilde{P}_{\text{GF},t}$  in Eq. (3), and then the STEC is converted into VTEC by means of a mapping function. The real-time VTEC from 130 global stations is directly modeled in a solar-geographic reference frame as Eq. (4). To mitigate the impacts of the unstable real-time data streams, e.g., the sudden interruption of the data streams, CAS-predicted TEC information is also included for RT-GIM computation. The broadcasted CAS RT-GIM is computed by the weighted combination of real-time VTEC spherical harmonic coefficients and predicted ionospheric information (Li et al., 2020).

### 2.2.2 Centre National d'Etudes Spatiales

In the framework of the RTS of the IGS, CNES has computed global VTEC in real time thanks to the CNES PPP-WIZARD project since 2014. The real-time VTEC is extracted by pseudorange and carrier phase GF combination as Eq. (3) with the help of a mapping function. The single-layer assumption in the mapping function adopts an altitude of 450 km above the Earth.

CNES also uses a spherical harmonic model for global VTEC representation, and the equation is the same as Eq. (4). Spherical harmonic coefficients are computed by means of a Kalman filter and simultaneous STEC from 100 stations of the real-time IGS network. CNES started to broadcast RT-GIM at the end of 2014 and changed spherical harmonic degrees from 6 to 12 in May of 2017 (Laurichesse and Blot, 2015).

### 2.2.3 Universitat Politècnica de Catalunya

UPC has been providing daily GIMs in IONEX format to IGS since 1998 (Hernández-Pajares et al., 1998, 1999; Orús

et al., 2005). In order to meet the demand of real-time GIM, the second author of this paper (from UPC-IonSAT) developed the Real-Time TOMographic IONosphere model software (RT-TOMION) and started to generate the UPC RT-GIM on 6 February 2011. The phase-only GF combination as Eq. (2) is used for obtaining real-time STEC from around 260 stations, and a 4-D voxel-based tomographic ionosphere model is adopted for global electron content modeling. The ionosphere is divided into two layers in the tomographic model, and the electron density of each voxel is estimated together with the ambiguity term  $B_{\text{GF}}$  by means of a Kalman filter in the sun-fixed reference frame. The estimated electron density is condensed at a fixed effective height (450 km) for the generation of a single-layer VTEC map, and then the VTEC interpolation method is adopted in a sun-fixed geomagnetic reference frame for filling the data gap on a global scale.

From 2011 to 2019, the kriging technique is selected by UPC for real-time VTEC interpolation. And the spherical harmonic model has been adopted by UPC since 8 September 2019. Recently, a new interpolation technique, denoted atomic decomposition interpolator of GIMs (ADIGIM), was developed. Since the global ionospheric electron content mainly depends on the diurnal, seasonal and solar variation, ADIGIM is computed by the weighted combination of good-quality historical GIMs (e.g., UQRG) with similar ionosphere conditions. The database of historical GIMs covers the last two solar cycles since 1998. The method for obtaining the weights of the linear combination of past maps is based on Eq. (6), which was first introduced in the problem of face recognition (Wright et al., 2008, 2010). While the face recognition is affected by the occlusions (such as glasses) in the face image, the reconstruction of GIM has problems in the regions that are not covered by GNSS stations. The problems have to be taken into account when selecting the past maps for combination and should not introduce a bias. As shown in Eq. (6), the problem is solved by introducing  $\ell_2$  norm and  $\ell_1$  norm. The property of the atomic decomposition and the least absolute shrinkage and selection operator (LASSO) is that it can select a small set of past maps which are the most similar to the real-time-measured VTEC at IPPs. The ADIGIM technique minimizes the difference between observed VTEC measurement and weighted VTEC from historical UQRG in similar ionosphere conditions. The underlying assumption is that the VTEC distribution over the areas not covered by the IPPs can be represented by the elements of the historical library of UQRG (Yang et al., 2021). The UPC RT-GIM with the new technique is denoted as UADG and generated by Eq. (6). Due to the improvement provided by the UADG, the broadcasted UPC-GIM was changed from USRG to UADG on 4 January 2021. In addition, the USRG and UADG are generated in real-time mode and saved in

IONEX format at HTTP as shown in Table 1.

$$\begin{cases} \text{VTEC}_{I,t} \approx D_{g,I,t} \cdot \alpha_t \\ \tilde{\alpha}_t = \arg \min_{\alpha_t} \frac{1}{2} \|\text{VTEC}_{I,t} - D_{g,I,t} \cdot \alpha_t\|_{\ell_2} + \rho \|\alpha_t\|_{\ell_1} \\ G_t = D_t \tilde{\alpha}_t \end{cases} \quad (6)$$

Here  $\text{VTEC}_{I,t}$  is the observed VTEC at IPP of epoch  $t$ . It is assumed that  $\text{VTEC}_{I,t}$  can be approximated by  $D_{g,I,t}$  and  $\alpha_t$ , while  $D_{g,I,t}$  is the VTEC extracted at IPP from historical databases of GIM  $g$  (for UPC, the UQRG is used), and  $\alpha_t$  is the unknown weight vector of each historical GIM at epoch  $t$ .  $\tilde{\alpha}_t$  is the estimated weight vector of each selected UQRG at epoch  $t$ . The estimated weight vector  $\tilde{\alpha}_t$  is obtained by the LASSO regression method with loss function norm  $\ell_2$  and regularization norm  $\ell_1$ .  $\ell_2$  is the norm for minimizing the Euclidean distance between observed VTEC measurements and historical UQRG databases at epoch  $t$ .  $\ell_1$  is the regularization norm for penalizing the approximation coefficients to limit the number of UQRG involved in the estimation, and  $\rho$  controls the sparsity of solution.  $G_t$  is the generated UPC RT-GIM of epoch  $t$  and is the weighted combination of historical UQRG. For mathematical convenience, each 2-D GIM is reformed as a 1-D vector (i.e., the columns are stacked along the meridian in order to create a vector of all the grid points of the map). This is justified because the measure of similarity is done over cells of  $2.5^\circ \times 5.0^\circ$  in the maps, and therefore the underlying  $\mathbb{R}^2$  (coordinate space of dimension 2) structure is not relevant for computing Euclidean distances in  $\ell_2$  norm.  $D_t$  is the selected historical UQRG database with similar ionosphere conditions at epoch  $t$ .

### 2.2.4 Wuhan University

The daily rapid and final GIM products have been generated with new WHU software named GNSS Ionosphere Monitoring and Analysis Software (GIMAS) since 21 June 2018 (Zhang and Zhao, 2018). At the end of the year 2020, WHU also published a first RT-GIM product.

WHU uses the spherical harmonic expansion model, and the formula is identical to Eq. (4). Currently, only the GPS real-time data streams from about 120 globally distributed IGS stations are used. The double-frequency code and carrier phase observations with a cut-off angle of  $10^\circ$  are used to gather precise geometry-free ionospheric data with the CCL method as Eq. (3) and ionospheric mapping function with the layer height of 450 km. In order to avoid the influence of satellite and receiver DCB on ionospheric parameter estimation, WHU directly uses the previous estimated DCB from the WHU rapid GIM product. According to previous experience, the real-time data are not enough to model the ionosphere precisely on a global scale with the spherical harmonic expansion technique. Considering the lack and the uneven distribution of the GPS-derived ionospheric data, 2 d predicted GIM as external ionospheric information is also incorporated. It is important to balance the weight between the real-time data and the background information. Both the

RT-GIM quality and the root mean square (rms) map are influenced by the weight (Zhang and Zhao, 2019).

In the year 2021, WHU is going to focus on how to further improve the accuracy of RT-GIM and update the computation method. The precise WHU RT-GIMs with multi-GNSS data and the application of WHU RT-GIM in the GNSS positioning as well as space physics domain are expected as next steps.

### 2.3 The combination of IGS RT-GIMs

Thanks to the contribution of the initial IGS real-time ionosphere centers (CAS, CNES and UPC) and globally distributed real-time GNSS stations, the first experimental IRTG was generated by means of the real-time dSTEC (RT-dSTEC) weighting technique (normalized inverse of the squared rms of RT-dSTEC error) in October 2018 (Roma-Dollase et al., 2018a; Li et al., 2020). Recently, WHU published the first WHU RT-GIM, and UPC upgraded the real-time VTEC interpolation technique. A new version of IRTG has been developed and broadcasted since 4 January 2021. The IGS combined RT-GIM is based on the weighted mean value of VTEC from different IGS centers as Eq. (7).

$$\begin{cases} \text{VTEC}_{\text{IRTG},t} = \sum_{g=1}^{N_{\text{AC}}} (w_{g,t} \cdot \text{VTEC}_{g,t}) \\ w_{g,t} = I_{g,t} / \sum_{g=1}^{N_{\text{AC}}} (I_{g,t}) \\ I_{g,t} = 1/\text{RMS}_{\delta,g,t}^2 \\ \text{RMS}_{\delta,g,t} = \sqrt{\sum_{i=1}^{N_t} (\delta_{g,i})^2 / N_t} \end{cases} \quad (7)$$

Here  $\text{VTEC}_{\text{IRTG},t}$  is the VTEC of IGS combined RT-GIM at epoch  $t$ , and  $\text{VTEC}_{g,t}$  is VTEC of RT-GIM  $g$  from the IGS center at epoch  $t$ .  $N_{\text{AC}}$  is the number of IGS centers.  $w_{g,t}$  is the weight of corresponding RT-GIM  $g$  at epoch  $t$  (the sum of  $w_{g,t}$  at epoch  $t$  is 1).  $\text{RMS}_{\delta,g,t}$  is the root mean square of RT-dSTEC error at epoch  $t$ .  $I_{g,t}$  is the inverse of the mean square of RT-dSTEC error at epoch  $t$ .  $N_t$  is the number of RT-dSTEC observations from the beginning epoch to the current epoch  $t$ .  $\delta_{g,i}$  is the RT-dSTEC error of RT-GIM  $g$  in the RT-dSTEC assessment.

In addition, the RT-dSTEC assessment is based on root mean square (rms) of the dSTEC error calculated by Eq. (8). In order to adapt to the real-time processing mode, the ambiguous reference STEC measurement  $L_{\text{GF},t_{\text{ref}}}$  is set to be the first elevation angle higher than  $10^\circ$  within a continuous phase arc to enable the RT-dSTEC calculation in the elevation-ascending arc.

$$\delta_{g,t} = \frac{1}{\alpha_{\text{GF}}} ((L_{\text{GF},t} - L_{\text{GF},t_{\text{ref}}}) - (M_z \cdot \text{VTEC}_{g,t} - M_{z_{\text{ref}}} \cdot \text{VTEC}_{g,t_{\text{ref}}})) \quad (8)$$

where  $\delta_{g,t}$  is the dSTEC error of GIM  $g$  at epoch  $t$ .  $t_{\text{ref}}$  is the epoch when reference elevation angle is stored.  $M_z$  and

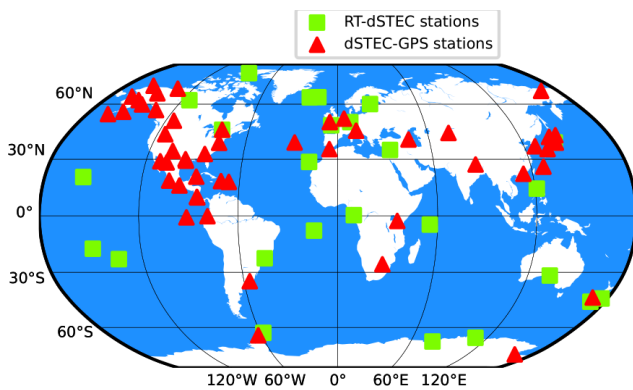


**Figure 1.** The 25 common real-time stations for RT-dSTEC assessment (in green) and 50 external GNSS stations for dSTEC-GPS assessment (in red).

$M_{z_{ref}}$  are the mapping functions of zenith angle of epoch  $t$  and zenith angle of reference epoch  $t_{ref}$ , respectively.

Due to the limited number of real-time stations, 25 common real-time stations that have been used by all the IGS real-time ionosphere centers are selected for allowing a fair RT-dSTEC assessment. The distribution can be seen as Fig. 1. Therefore, the RT-dSTEC is the measurement of “internal” post-fit residuals of RT-GIMs and still sensitive to the accuracy of assessed GIMs. Every 20 min, the RT-dSTEC assessment is performed and used for the combination of different IGS RT-GIMs. The steps for the generation of IRTG can be seen as Fig. 2. The RTCM-SSR has been the standard message for real-time corrections, and the IGS State Space Representation (SSR) format version 1.00 was published on 5 October 2020 (IGS, 2020). The content of IGS-SSR is compatible with RTCM-SSR contents. And the IGS-SSR format can support more extensions such as satellite attitude, phase center offsets, and variations in the near future. At present, both RTCM-SSR and IGS-SSR formats are used for the dissemination of RT-GIMs. In addition, IGS defines different references for antenna correction: average phase center (APC) and center of mass (CoM). The current status of RT-GIMs from different ionosphere centers can be seen in Table 2. It should be noted that “SSRA” means the SSR with the APC reference, and “SSRC” means the SSR with the CoM reference.

### 3 The performance of IGS RT-GIMs

In this section, the performance of IGS RT-GIMs was analyzed and compared with rapid IGS GIMs as well as IGS combined final GIM. It should be noted that the RT-GIMs were gathered with BKG Ntrip Client (BNC) software (Weber et al., 2016) and generated by received spherical harmonic coefficients from different centers as in Table 2. And there were two kinds of temporal resolution for received RT-GIMs: the common temporal resolution of 20 min and the

full (original) temporal resolution. Since the IRTG is combined every 20 min, we will focus on such a common time resolution to compare the performance. The detail of compared RT-GIMs can be seen in Table 3. The influence of temporal resolution on RT-GIMs was also shown in this section.

Before detailing the Jason-3 VTEC and GPS-dSTEC assessment, it should be taken into account that the GIM error versus Jason VTEC measurements have a high correlation with the GIM error versus dSTEC-GPS measurements, although the Jason VTEC measurements are vertical and the dSTEC-GPS measurements are slanted. As demonstrated in Hernández-Pajares et al. (2017), the Jason-3 VTEC assessment and dSTEC-GPS assessment are independent and consistent for GIM evaluation. In other words, the slant ray path geometry changes do not affect the capability of dSTEC reference data to rank the GIM, and the electron content between the Jason-3 altimeter and the GNSS satellites does not significantly affect the assessment of GIMs based on Jason-3 VTEC data.

#### 3.1 Jason-3 VTEC assessment

The VTEC from the Jason-3 altimeter was gathered as an external reference over the oceans. After applying a sliding window of 16 s to smooth the altimeter measurements, the typical standard deviation of Jason-3 VTEC measurement error is around 1 TECU. Although the electron content above the Jason-3 altimeter (about 1300 km) is not available and the altimeter bias is around a few TECU, the standard deviation of the difference between GIM-VTEC and Jason-3 VTEC is adopted to avoid the Jason-3 altimeter bias and the constant bias component of the plasmaspheric electron content in the assessment. The plasmaspheric electron content variation is up to a few TECU and is a relatively small part when compared with the GIM errors over the oceans. Jason-3 VTEC has been proven to be a reliable reference of VTEC over the oceans. The oceans are the most challenging regions for GIMs where permanent GNSS receivers are typically far away (Roma-Dollase et al., 2018b; Hernández-Pajares et al., 2017). In this context, the daily standard deviation of the difference between Jason-3 VTEC and GIM-VTEC was suitable as the statistic for GIM assessment in Eq. (9).

$$\begin{cases} \text{Bias}_g = \sum_{i=1}^{N_J} (\text{VTEC}_{\text{Jason-3},i} - \text{VTEC}_{g,i}) / N_J \\ \text{STD}_g = \sqrt{\sum_{i=1}^{N_J} (\text{VTEC}_{\text{Jason-3},i} - \text{VTEC}_{g,i} - \text{Bias}_g)^2 / (N_J - 1)} \end{cases}, \quad (9)$$

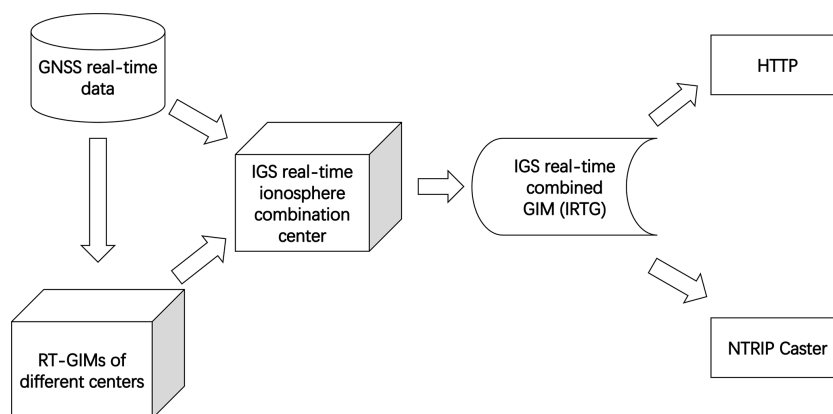
where  $\text{VTEC}_{\text{Jason},i}$  and  $\text{VTEC}_{\text{GIM},i}$  are VTEC extracted from Jason-3 and GIM observation  $i$ , respectively.  $N_J$  is the number of involved observations.

The recent 3-month data (1 December 2020 to 1 March 2021), containing the two significant events (new contributing RT-GIM (WHU) from 3 January 2021 and the introduction of the new atomic decomposition UPC-GIM (UADG) on 4 January 2021), have been selected to study the consistency and performance of the IGS RT-GIMs.



**Table 2.** The current status of broadcasting IGS RT-GIMs.

Agency	Temporal resolution	Broadcast frequency	Spherical harmonic degree	Mount points in NTRIP caster	Real-time IONEX saved at FTP/HTTP
CAS	5 min	1 min	15	123.56.176.228:2101/CAS05 <sup>a</sup> 59.110.42.14:2101/SSRA00CAS1 <sup>b</sup> 59.110.42.14:2101/SSRA00CAS0 <sup>a</sup> 59.110.42.14:2101/SSRC00CAS1 <sup>b</sup> 59.110.42.14:2101/SSRC00CAS0 <sup>a</sup> 182.92.166.182:2101/IONO00CAS1 <sup>b</sup> 182.92.166.182:2101/IONO00CAS0 <sup>a</sup>	ftp://ftp.gipp.org.cn/product/ionex/ (last access: 10 September 2021) (update at the end of day)
CNES	2 min	1 min	12	products.igs-ip.net:2101/CLK91 <sup>a</sup> products.igs-ip.net:2101/SSRA00CNE1 <sup>b</sup> products.igs-ip.net:2101/SSRA00CNE0 <sup>a</sup> products.igs-ip.net:2101/SSRC00CNE1 <sup>b</sup> products.igs-ip.net:2101/SSRC00CNE0 <sup>a</sup>	No
UPC (only UADG)	15 min	15 s	15	products.igs-ip.net:2101/IONO00UPC1 <sup>b</sup>	http://chapman.upc.es/tomion/real-time/quick/ (last access: 10 September 2021) (UADG and USRG, update every 15 min)
WHU	5 min	1 min	15	58.49.58.150:2106/IONO00WHU0 <sup>a</sup>	No
IGS	20 min	15 s	15	products.igs-ip.net:2101/IONO00IGS1 <sup>b</sup>	http://chapman.upc.es/irtg/ (last access: 10 September 2021) (update every 20 min)

<sup>a</sup> RTCM-SSR format.<sup>b</sup> IGS-SSR format.**Figure 2.** Data flow for the IGS real-time combined GIM.

As can be seen in Fig. 3, the standard deviation of UPC RT-GIM (upc1) VTEC versus measured Jason-3 VTEC is worse than other RT-GIMs before the transition from USRG to UADG on 4 January 2021. It should be noted that the upc1 in RTCM-SSR format was stopped from 15 December 2020 to 2 January 2021, due to the change of broadcasting

format and some technical issues. The assessment of upc1 was based on the UPC RT-GIMs saved in a local repository during the interrupted period. The standard deviation of upc1 VTEC versus measured Jason-3 VTEC reached around 7 TECU on 6 December 2020 due to the interruption of the downloading module. And the upc1 achieved a significant

**Table 3.** The ID of compared IGS RT-GIMs.

Agency	20 min RT-GIM	RT-GIM with full temporal resolution
CAS	crtg	crfg
CNES	cnes	cnfs
UPC	upc1	upf1
WHU	whu0	whf0
IGS	irtg	irfg*

\* Note irfg and irtg are the same.

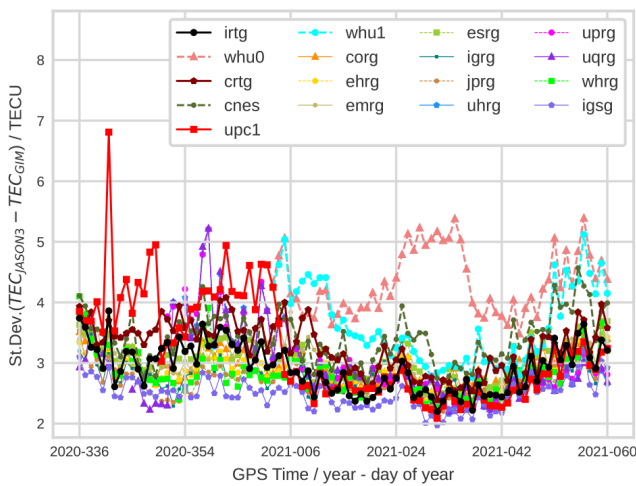


**Figure 3.** Daily standard deviation of GIM VTEC versus measured Jason-3 VTEC (in TECU), from 1 December 2020 to 1 March 2021.

improvement after the transition on 4 January 2021. In addition, the accuracy of IGS experimental combined RT-GIM (irtg) also increased due to the better performance of upc1. Compared with IGS rapid GIMs (corg, ehrg, emrg, esrg, igrg, jprg, uhrg, uprg, uqrg, whrg) and IGS final combined GIM (igsg), the upc1 and irtg are equivalent to the post-processed GIMs and even better than some rapid GIMs. The accuracy of CAS RT-GIM (crtg) and CNES RT-GIM (cnes) is close to the post-processed GIMs, while WHU RT-GIM (whu0) is slightly worse than the other GIMs. As shown and explained in Eq. (4), the whu0 is shifted by 0 h. To see the influence of phase-shifted  $\lambda_{S,t}$ , the whu0 is manually shifted by 2 h (i.e., take  $t_0$  as 2 h for whu0 in Eq. 4) in post-processing mode. And the accuracy of the 2 h shifted WHU RT-GIM (whu1) is slightly better than whu0 as can be seen in Fig. 3.

In order to investigate the influence of temporal resolution on RT-GIMs over oceans, different RT-GIMs with full temporal resolution were involved. The summary of Jason-3 VTEC assessment can be seen in Table 4. The overall standard deviation of GIM-VTEC minus Jason-3 VTEC is computed in separate time periods to focus on the influence of the transition from USRG to UADG. As shown in Table 4, the overall standard deviation of GIM-VTEC versus Jason-3

VTEC is consistent with Fig. 3, and the quality of 20 min and full temporal resolution of RT-GIMs are similar over oceans. And the accuracy of 2 h shifted whu1 in Jason-3 VTEC assessment is higher than whu0 in Table 4. In particular, the overall standard deviation of upc1 VTEC versus measured Jason-3 VTEC drops from 4.3 to 2.7 TECU, and, in agreement with that, the standard deviation of irtg VTEC versus measured Jason-3 VTEC decreases from 3.3 to 2.8 TECU.

### 3.2 dSTEC-GPS assessment

In addition, dSTEC-GPS assessment in post-processing mode was involved as a complementary tool with high accuracy (better than 0.1 TECU) over continental regions on a global scale. In the dSTEC-GPS assessment, the maximum elevation angle within a continuous arc was regarded as the reference angle in Eq. (8). The dSTEC observations provide the direct measurements of the difference of STEC within a continuous phase arc involving different geometries. As has been introduced before, the STEC is proportional to VTEC by means of the ionospheric mapping function. Therefore, the dSTEC error observations (see Eq. 8), containing different geometries and mapping function error are direct measurements for evaluating GIM-STEAC, which is commonly used by GNSS users to calculate ionospheric correction. In addition, the common agreed ionospheric thin layer model is set to be 450 km in height in the generation of GIM to provide VTEC in a consistent way for different ionospheric analysis centers. And in this way the GNSS users are able to consistently recover the STEC from GIM-VTEC by the commonly agreed mapping function. The dSTEC-GPS assessment was performed by globally distributed GNSS stations as shown in Fig. 1 on 3 January (before the transition of UPC RT-GIM from USRG to UADG) and 5 January (after the transition) in 2021, with a focus on the transition of UPC RT-GIM. The rms error and relative error were used for the assessment as Eq. (10).

$$\left\{ \begin{array}{l} \text{RMS}_{\delta,g} = \sqrt{\sum_{i=1}^{N_S} (\delta_{g,i})^2 / N_S} \\ O_{\Delta_{S_{GPS,t,i}}} = (L_{GF,t} - L_{GF,t_{ref}}) / \alpha_{GF} \\ \text{RMS}_{\Delta_{S_{GPS}}} = \sqrt{\sum_{i=1}^{N_S} (O_{\Delta_{S_{GPS,t,i}}})^2 / N_S} \\ \text{Relative error}_g = 100 \cdot \text{RMS}_{\delta,g} / \text{RMS}_{\Delta_{S_{GPS}}} \end{array} \right. \quad (10)$$

Here  $\text{RMS}_{\delta,g}$  is the rms error of GIM  $g$ . And  $\delta_{g,i}$  is the dSTEC error of GIM  $g$  similar to Eq. (8), while the reference angle of Eq. (8) is replaced by the maximum elevation angle within a continuous arc.  $N_S$  is the number of involved observations.  $O_{\Delta_{S_{GPS,t,i}}}$  is the dSTEC-GPS observation.  $\text{RMS}_{\Delta_{S_{GPS}}}$  is the rms of the observed dSTEC-GPS.  $\text{Relative error}_g$  is the relative error of GIM  $g$ .

As shown in Table 4, the rms error of most post-processed GIMs reaches around 2 or 3 TECU, while the rms error ranges from 2.8 to 5.54 TECU for RT-GIMs. The transi-

**Table 4.** Standard deviation of GIM-VTEC minus Jason-3 VTEC in Jason-3 VTEC assessment (last two columns) and dSTEC-GPS assessment results of RT-GIMs on 3 January (second and third columns) and 5 January (fourth and fifth columns) in 2021.

GIM	RMSE of 3 January in dSTEC-GPS assessment (TECU)	Relative error of 3 January in dSTEC-GPS assessment (%)	RMSE of 5 January in dSTEC-GPS assessment (TECU)	Relative error of 5 January in dSTEC-GPS assessment (%)	Overall standard deviation of the GIM-VTEC versus measured Jason-3 VTEC from 1 December 2020 to 3 January 2021 in Jason-3 VTEC assessment (TECU)	Overall standard deviation of GIM-VTEC versus measured Jason-3 VTEC from 4 January to 1 March 2021 in Jason-3 VTEC assessment (TECU)
corg	2.90	45.07	3.35	49.20	3.1	2.9
ehrg	2.54	39.55	2.81	41.23	3.0	2.8
emrg	2.62	40.75	2.73	40.08	3.2	2.9
esrg	2.70	41.98	3.06	44.99	3.2	3.0
igr	2.60	40.40	3.06	44.99	2.9	2.8
jprg	2.73	42.46	2.86	41.98	2.8	2.7
uhrg	1.91	29.69	2.21	32.43	3.9	2.8
uprg	2.04	31.80	2.41	35.39	3.9	2.8
uqrg	1.89	29.44	2.19	32.24	3.5	2.8
whrg	2.42	37.63	2.65	38.94	3.0	2.8
igsg	2.33	36.25	2.57	37.74	2.6	2.5
crtg	3.36	52.25	3.86	56.67	3.6	3.2
crfg	4.29	66.67	3.92	57.56	3.7	3.2
cnes	<b>3.35</b>	52.13	3.74	54.86	3.5	3.4
cnfs	3.58	55.73	4.62	67.88	3.5	3.4
upc1	3.85	59.91	<b>2.80</b>	41.06	4.3	<b>2.7</b>
upf1	3.87	60.20	2.81	41.26	4.5	<b>2.7</b>
whu0	5.19	80.69	5.45	79.84	4.3	4.4
whf0	5.31	82.61	5.54	81.28	4.3	4.4
whu1	4.37	67.97	4.40	64.55	4.3	3.8
irtg	<i>4.11</i>	63.86	<i>3.37</i>	49.47	<b>3.3</b>	2.8

The value in bold font means the corresponding RT-GIM has the best performance among the remaining RT-GIMs in each column, and values of irtg are italic for comparison.

tion of UPC RT-GIM (upf1) from USRG to UADG is apparent in the dSTEC-GPS assessment, and the rms error of IGS RT-GIM (irtg) decreased from 4.11 to 3.37 TECU due to the improvement of UPC RT-GIM. After the transition of UPC RT-GIM, the performance of upf1 and irtg is comparable with most post-processed GIMs. Similar to the performance in the Jason-3 VTEC assessment, the accuracy of the remaining RT-GIMs is close to post-processed GIMs. And the rms error of 2 h shifted whu1 is around 4.4 TECU, which is better than the whu0. Therefore, the 2 h shift is recommended for  $\lambda_{S,t}$  in Eq. (4). It should be pointed out that the performance of RT-GIMs with the full temporal resolution is slightly worse than 20 min RT-GIMs. Furthermore, the full temporal resolution RT-GIM is even worse than the GIM obtained by linear interpolation of the 20 min RT-GIM in a sun-fixed reference frame. This is coincident with a smaller number of ionospheric observations at shorter timescales. In Fig. 4, the performance of IGS RT-GIMs after the upgrade of the UPC interpolation method in the dSTEC-GPS assessment

is represented. The higher values of rms errors occur around the Equator and Southern Hemisphere for all the RT-GIMs. And the higher values might be caused by the high-electron-density gradients at the Equator and the sparse distribution of real-time stations in the Southern Hemisphere.

### 3.3 The sensibility of real-time weighting technique

RT-dSTEC assessment of RT-GIMs was automatically running in real-time mode and used for real-time weighting in the combination of IGS RT-GIMs. In order to compare with the dSTEC-GPS assessment, the RT-dSTEC assessment with real-time stations in Fig. 1 was also performed on 3 and 5 January 2021. As can be seen in Table 5, the rank of RT-GIMs in the RT-dSTEC assessment is similar to the dSTEC-GPS assessment, but the rms error values are larger. And the larger rms error coincides with the much lower elevation angle of the observation reference in the RT-dSTEC assessment.

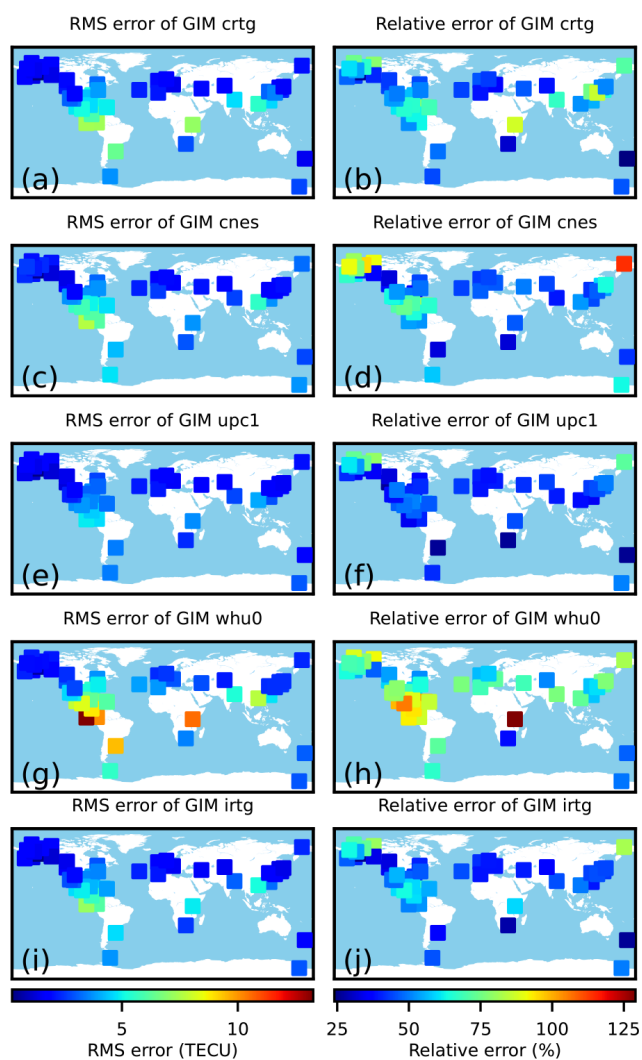


**Figure 4.** The distribution of dSTEC-GPS results on 5 January 2021 (after the improvement of the UPC interpolation technique).

**Table 5.** RMSE of RT-GIMs in RT-dSTEC assessment on 3 and 5 January 2021.

GIM	RMSE of 3 January (TECU)	RMSE of 5 January (TECU)
upc1	4.24	<b>3.91</b>
crtg	4.25	4.98
cnes	<b>3.98</b>	4.07
whu0	5.94	5.81

The value in bold font means the corresponding RT-GIM has the best performance among the remaining RT-GIMs in each column.

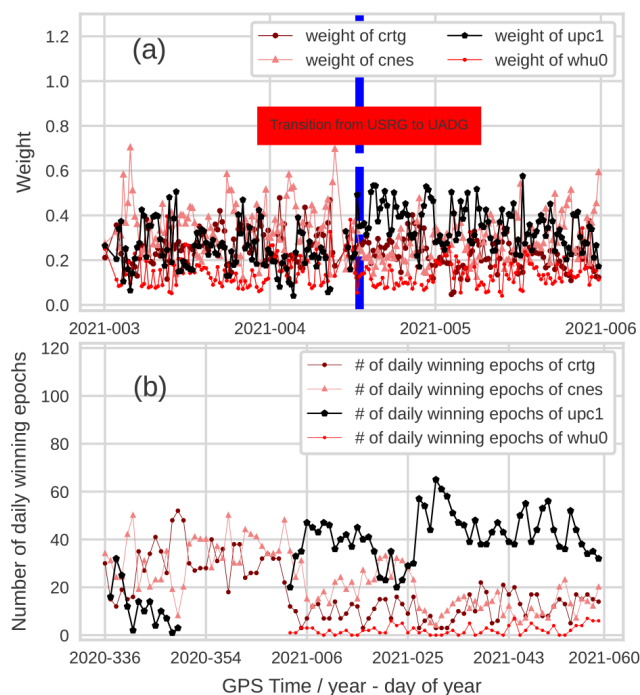


**Figure 5.** The evolution of real-time weights and daily winning epochs of RT-GIMs. (a) The real-time weights from 3 to 5 January 2021. (b) The daily number of epochs when one of the RT-GIMs is better than the others from 1 December 2020 to 1 March 2021.

The real-time weights of RT-GIMs can be defined as the normalized inverse of the squared rms of RT-dSTEC errors and represent the accuracy of RT-GIMs in the RT-dSTEC assessment. For each RT-GIM, the number of daily winning epochs is computed by counting the number of epochs within the day when the one RT-GIM is better than the other RT-GIMs. The evolution of daily winning epochs of RT-GIMs shown in the bottom figure of Fig. 5 is consistent with the Jason-3 VTEC assessment. The upc1 was not involved in the combination from 15 December 2020 to 2 January 2021 when the dissemination of upc1 was stopped, as can be seen in the bottom figure of Fig. 5. The significant improvement of the transition of upc1 from USRG to UADG shown in dSTEC-GPS and the Jason-3 VTEC assessment is also obvious in the top panel of Fig. 5. In addition, the daily winning epoch’s evolution and the transition in Fig. 5 are consistent with the accuracy of RT-GIMs, providing a combined RT-GIM which is one of the best RT-GIMs, as shown in the altimeter-based and dSTEC-based assessments. The good performance of the combination algorithm can be mainly explained from the point of view of the weights, i.e., the sensitivity of the dSTEC error to the quality of the RT-GIMs, but also from the point of view of the linear combination that can play a positive role under any potential negative correlation between the performance of pairs of involved RT-GIMs.

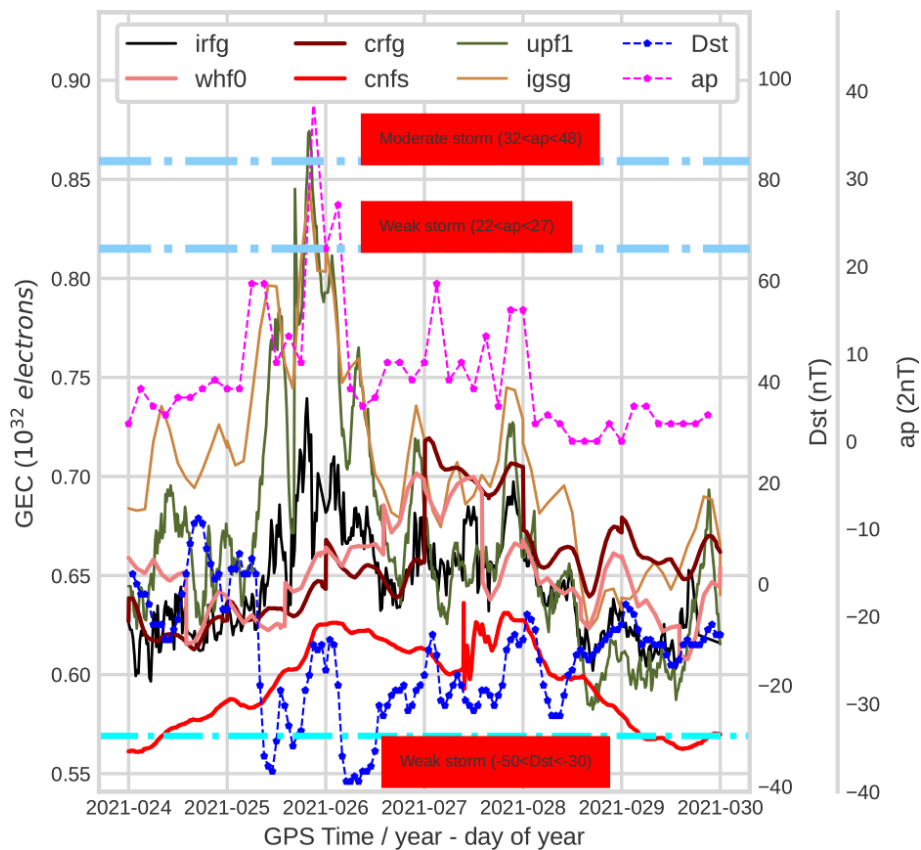


**Figure 6.** The GEC, ap and Dst evolution of RT-GIMs from 24 to 29 January 2021 during the low-solar-activity period.

### 3.4 The response of RT-GIMs to recent minor geomagnetic storms

The global electron content (GEC) is defined as the total number of free electrons in the ionosphere. Hence the GEC can be estimated from the summation of the product of the VTEC value and the area of the corresponding GIM cell. In addition, GEC has been used as an ionospheric index (Afraimovich et al., 2006; Hernández-Pajares et al., 2009). With the purpose of further checking the consistency of IGS RT-GIMs, the GEC of RT-GIMs was calculated and compared from 24 to 29 January 2021. It should be noted that the solar activity is low in January 2021. During the selected period, several weak geomagnetic storms and one moderate geomagnetic storm occurred according to the classification of geomagnetic indices (Loewe and Prölss, 1997; Gonzalez et al., 1999), and the GEC evolution can be seen in Fig. 6. The GEC of CNES RT-GIM (cnfs) is slightly different from other RT-GIMs, and seems to be caused by the bias in CNES RT-GIM. There are some jumps in the GEC evolution of CAS RT-GIM (crfg) and WHU RT-GIM (whf0), and the jumps might be related to the handling of day boundary or unreal predicted GIM in certain cases. Compared with IGS final combined GIM (igsg), the good performance of global VTEC representation with upf1 and irfg can be seen in Fig. 6.

In addition, the response of upf1 and irfg to the recent minor geomagnetic storms (detected by 3 h ap and 1 h Dst indices) is apparent and also similar to the post-processed IGS final combined GIM (igsg).

## 4 Data availability

The IGS real-time combined GIMs during the testing period are available from Zenodo at <https://doi.org/10.5281/zenodo.5042622> (Liu et al., 2021b) in IONEX format (Schaer et al., 1998). In addition, more archived IGS combined RT-GIMs can be found at <http://chapman.upc.es/irtg/archive/> (Liu and Hernández-Pajares, 2021a), and the latest IGS combined RT-GIMs are available in real-time mode at [http://chapman.upc.es/irtg/last\\_results/](http://chapman.upc.es/irtg/last_results/) (Liu and Hernández-Pajares, 2021b).

## 5 Conclusions

In this paper, we have summarized the computation methods of RT-GIMs from four individual IGS ionosphere centers and introduced the new version of IGS combined RT-GIM. Ac-

According to the results of Jason-3 VTEC and dSTEC-GPS assessment, it could be concluded as follows.

- The real-time weighting technique for the generation of IGS combined RT-GIM performs well when it is compared with Jason-3 VTEC and dSTEC-GPS assessment.
- The transition of UPC RT-GIM from USRG to UADG is obvious in all involved assessments and also demonstrates the sensibility of the real-time weighting technique to RT-GIMs when the accuracy of RT-GIMs is increased.
- The quality of most IGS RT-GIMs is close to post-processed GIMs.
- The difference among RT-GIMs with 20 min and full temporal resolution can be neglected over oceans in the Jason-3 VTEC assessment (see Fig. 3 and Table 4), while the difference is visible in some RT-GIMs over continental regions in the dSTEC-GPS assessment (see Table 4). The lower accuracy of GIMs with full temporal resolution (2 or 5 min) might be related to the uneven distribution of ionospheric observations, the weight between predicted GIMs and real-time observations. Combined with the previous study (Liu et al., 2021a), it is suggested to find a more suitable temporal resolution for the generation of RT-GIM in a sun-fixed reference frame.

In addition, the GEC evolution of UPC RT-GIM and IGS combined RT-GIM is close to the GEC evolution of IGS final combined GIM in post-processing mode and has an obvious response to the geomagnetic storm during the low-solar-activity period. Future improvements might include the following.

- Broadcast real-time rms maps that can be useful for the positioning users.
- Increase the accuracy of high-temporal-resolution RT-GIMs. In addition, higher maximum spherical harmonic degrees might be adopted to increase the accuracy and spatial resolution of RT-GIMs.
- Coinciding with a much larger number of RT-GNSS receivers in the future, the dSTEC weighting might be improved by replacing the “internal” with the “external” receivers, i.e., not used by any real-time analysis centers. In this way the weighting would be sensitive as well to the interpolation–extrapolation error of the different real-time ionospheric GIMs to be combined. And the resulting combination might behave better.
- Increase the number of worldwide GNSS receivers used for the RT-dSTEC up to more than 100. In this way we will be able to study the potential upgrade of the present global weighting to a regional weighting among other potential improvements in the combination strategy.

**Author contributions.** QL wrote the manuscript. QL developed the updated combination software with contributions from DRD, HY and MHP. QL and MHP designed the research, with contributions from HY, EMM, DRD and AGR. QL, HY, EMM, MHP, ZL, NW, DL, AB, Q. Zhao and Q. Zhang provided the real-time GIMs of the corresponding IGS centers. AH, MS, GW and AS contributed in creating the framework of the real-time IGS service, the ionospheric message format and BNC open software updates. LA suggested the initial idea of this work. AK, StS, JF, AK, RGF and AGR contributed in the generation of rapid and final IGS GIMs used as additional references in the manuscript.

**Competing interests.** The contact author has declared that neither they nor their co-authors have any competing interests.

**Disclaimer.** Publisher’s note: Copernicus Publications remains neutral with regard to jurisdictional claims in published maps and institutional affiliations.

**Acknowledgements.** The authors are thankful to the collaborative and friendly framework of the International GNSS Service, an organization providing first-class open data and open products (Johnston et al., 2017). The VTEC data from the Jason-3 altimeter were gathered from the NASA EOSDIS Physical Oceanography Distributed Active Archive Center (PO.DAAC) at the Jet Propulsion Laboratory, Pasadena, CA (<https://doi.org/10.5067/GHGMR-4FJ01>), and the National Oceanic and Atmospheric Administration (NOAA). We are also thankful to GeoForschungsZentrum (GFZ) and to World Data Center (WDC) for Geomagnetism, Kyoto, for providing the ap and Dst indices.

**Financial support.** This research has been supported by the China Scholarship Council (CSC). The contribution from UPC-IonSAT authors was partially supported by the European Union-funded project PITHIA-NRF (grant no. 101007599) and by the ESSP/ICAO-funded project TEC4SpaW. The work of Andrzej Krankowski is supported by the National Centre for Research and Development, Poland, through grant ARTEMIS (grant nos. DWM/PL-CHN/97/2019 and WPC1/ARTEMIS/2019).

**Review statement.** This paper was edited by Christian Voigt and reviewed by two anonymous referees.

## References

- Afraimovich, E., Astafyeva, E., Oinats, A., Yasukevich, Y. V., and Zhivetiev, I.: Global electron content and solar activity: comparison with IRI modeling results, in: poster presentation at IGS Workshop, Darmstadt, Germany, 8–11 May 2006.
- Caissy, M., Agrotis, L., Weber, G., Hernandez-Pajares, M., and Hugentobler, U.: Innovation: Coming Soon-The International GNSS Real-Time Service, available at:

- <https://www.gpsworld.com/gnss-systemaugmentation-assistanceinnovation-coming-soon-13044/> (last access: 21 March 2021), 2012.
- Chen, J., Ren, X., Zhang, X., Zhang, J., and Huang, L.: Assessment and Validation of Three Ionospheric Models (IRI-2016, NeQuick2, and IGS-GIM) From 2002 to 2018, *Space Weather*, 18, e2019SW002422, <https://doi.org/10.1029/2019SW002422>, 2020.
- Ciraolo, L., Azpilicueta, F., Brunini, C., Meza, A., and Radice, S.: Calibration errors on experimental slant total electron content (TEC) determined with GPS, *J. Geodesy*, 81, 111–120, <https://doi.org/10.1007/s00190-006-0093-1>, 2007.
- Elsobeiey, M. and Al-Harbi, S.: Performance of real-time Precise Point Positioning using IGS real-time service, *GPS Solut.*, 20, 565–571, <https://doi.org/10.1007/s10291-015-0467-z>, 2016.
- Feltens, J.: Development of a new three-dimensional mathematical ionosphere model at European Space Agency/European Space Operations Centre, *Space Weather*, 5, S12002, <https://doi.org/10.1029/2006SW000294>, 2007.
- Feltens, J. and Schaer, S.: IGS Products for the Ionosphere, in: Proceedings of the 1998 IGS Analysis Center Workshop Darmstadt, Germany, 9–11 February 1998, pp. 3–5, 1998.
- Fernandes, M. J., Lázaro, C., Nunes, A. L., and Scharroo, R.: Atmospheric corrections for altimetry studies over inland water, *Remote Sens.-Basel*, 6, 4952–4997, <https://doi.org/10.3390/rs6064952>, 2014.
- Froń, A., Galkin, I., Krankowski, A., Bilitza, D., Hernández-Pajares, M., Reinisch, B., Li, Z., Kotulak, K., Zakharenkova, I., Cherniak, I., Roma Dollase, D., Wang, N., Flisek, P., and García-Rigo, A.: Towards Cooperative Global Mapping of the Ionosphere: Fusion Feasibility for IGS and IRI with Global Climate VTEC Maps, *Remote Sens.-Basel*, 12, 3531, <https://doi.org/10.3390/rs12213531>, 2020.
- García-Rigo, A., Monte, E., Hernández-Pajares, M., Juan, J., Sanz, J., Aragón-Ángel, A., and Salazar, D.: Global prediction of the vertical total electron content of the ionosphere based on GPS data, *Radio Sci.*, 46, RS0D25, <https://doi.org/10.1029/2010RS004643>, 2011.
- García Rigo, A., Roma Dollase, D., Hernández Pajares, M., Li, Z., Terkildsen, M., Ghoddousi Fard, R., Dettmering, D., Erdogan, E., Haralambous, H., Beniguel, Y., Berdermann, J., Kriegel, M., Krypiak-Gregorczyk, A., Gulyaeva, T., Komjathy, A., Vergados, P., Feltens, J., Zandbergen, R., Olivares, G., Fuller-Rowell, T., Altadill, D., Blanch, E., Bergeot, N., Krankowski, A., Agrotis, L., Galkin, I., Orus-Perez, R., and Prol, F. S.: St. Patrick's day 2015 geomagnetic storm analysis based on real time ionosphere monitoring, in: EGU 2017: European Geosciences Union General Assembly, Vienna, Austria, 23–28 April 2017, proceedings book, 2017.
- Ghoddousi-Fard, R.: GPS ionospheric mapping at Natural Resources Canada, in: IGS workshop, Pasadena, 23–27 June 2014.
- Gonzalez, W. D., Tsurutani, B. T., and De Gonzalez, A. L. C.: Interplanetary origin of geomagnetic storms, *Space Sci. Rev.*, 88, 529–562, <https://doi.org/10.1023/A:1005160129098>, 1999.
- Gulyaeva, T. L. and Stanislawski, I.: Derivation of a planetary ionospheric storm index, *Ann. Geophys.*, 26, 2645–2648, <https://doi.org/10.5194/angeo-26-2645-2008>, 2008.
- Gulyaeva, T. L., Arikani, F., Hernandez-Pajares, M., and Stanislawski, I.: GIM-TEC adaptive ionospheric weather assessment and forecast system, *J. Atmos. Sol.-Terr. Phys.*, 102, 329–340, <https://doi.org/10.1016/j.jastp.2013.06.011>, 2013.
- Hernández-Pajares, M., Juan, J., and Sanz, J.: Neural network modeling of the ionospheric electron content at global scale using GPS data, *Radio Sci.*, 32, 1081–1089, <https://doi.org/10.1029/97RS00431>, 1997.
- Hernández-Pajares, M., Juan, J., Sanz, J., and Solé, J.: Global observation of the ionospheric electronic response to solar events using ground and LEO GPS data, *J. Geophys. Res.-Space*, 103, 20789–20796, <https://doi.org/10.1029/98JA01272>, 1998.
- Hernández-Pajares, M., Juan, J., and Sanz, J.: New approaches in global ionospheric determination using ground GPS data, *J. Atmos. Sol.-Terr. Phys.*, 61, 1237–1247, [https://doi.org/10.1016/S1364-6826\(99\)00054-1](https://doi.org/10.1016/S1364-6826(99)00054-1), 1999.
- Hernández-Pajares, M., Juan, J., Sanz, J., Orus, R., García-Rigo, A., Feltens, J., Komjathy, A., Schaer, S., and Krankowski, A.: The IGS VTEC maps: a reliable source of ionospheric information since 1998, *J. Geodesy*, 83, 263–275, <https://doi.org/10.1007/s00190-008-0266-1>, 2009.
- Hernández-Pajares, M., Roma-Dollase, D., Krankowski, A., García-Rigo, A., and Orús-Pérez, R.: Methodology and consistency of slant and vertical assessments for ionospheric electron content models, *J. Geodesy*, 91, 1405–1414, <https://doi.org/10.1007/s00190-017-1032-z>, 2017.
- Hernández-Pajares, M., Lyu, H., Aragón-Ángel, À., Monte-Moreno, E., Liu, J., An, J., and Jiang, H.: Polar Electron Content From GPS Data-Based Global Ionospheric Maps: Assessment, Case Studies, and Climatology, *J. Geophys. Res.-Space*, 125, e2019JA027677, <https://doi.org/10.1029/2019JA027677>, 2020.
- Hoque, M. M., Jakowski, N., and Orús-Pérez, R.: Fast ionospheric correction using Galileo Az coefficients and the NTCM model, *GPS Solut.*, 23, 41, <https://doi.org/10.1007/s10291-019-0833-3>, 2019.
- IGS: IGS State Space Representation (SSR) Format Version 1.00, available at: [https://files.igs.org/pub/data/format/igs\\_ssr\\_v1.pdf](https://files.igs.org/pub/data/format/igs_ssr_v1.pdf) (last access: 21 March 2021), 2020.
- Jakowski, N., Hoque, M., and Mayer, C.: A new global TEC model for estimating transionospheric radio wave propagation errors, *J. Geodesy*, 85, 965–974, <https://doi.org/10.1007/s00190-011-0455-1>, 2011.
- Jiang, H., Liu, J., Wang, Z., An, J., Ou, J., Liu, S., and Wang, N.: Assessment of spatial and temporal TEC variations derived from ionospheric models over the polar regions, *J. Geodesy*, 93, 455–471, <https://doi.org/10.1007/s00190-018-1175-6>, 2019.
- Johnston, G., Riddell, A., and Hausler, G.: The International GNSS Service, in: Springer Handbook of Global Navigation Satellite Systems, 1st edn., edited by: Teunissen, P. J. and Montenbruck, O., Springer International Publishing, Cham, Switzerland, 967–982, <https://doi.org/10.1007/978-3-319-42928-1>, 2017.
- Komjathy, A. and Born, G. H.: GPS-based ionospheric corrections for single frequency radar altimetry, *J. Atmos. Sol.-Terr. Phys.*, 61, 1197–1203, [https://doi.org/10.1016/S1364-6826\(99\)00051-6](https://doi.org/10.1016/S1364-6826(99)00051-6), 1999.
- Komjathy, A., Galvan, D., Stephens, P., Butala, M., Akopian, V., Wilson, B., Verkhoglyadova, O., Mannucci, A., and Hickey, M.: Detecting ionospheric TEC perturbations caused by natural hazards using a global network of GPS receivers: The

- Tohoku case study, *Earth Planets Space*, 64, 1287–1294, <https://doi.org/10.5047/eps.2012.08.003>, 2012.
- Laurichesse, D. and Blot, A.: New CNES real time products including BeiDou, available at: <https://lists.igs.org/pipermail/igsmail/2015/001017.html> (last access: 21 March 2021), 2015.
- Le, A. Q. and Tiberius, C.: Single-frequency precise point positioning with optimal filtering, *GPS Solut.*, 11, 61–69, <https://doi.org/10.1007/s10291-006-0033-9>, 2007.
- Li, M., Yuan, Y., Wang, N., Li, Z., and Huo, X.: Performance of various predicted GNSS global ionospheric maps relative to GPS and JASON TEC data, *GPS Solut.*, 22, 55, <https://doi.org/10.1007/s10291-018-0721-2>, 2018.
- Li, X., Ge, M., Zhang, H., and Wickert, J.: A method for improving uncalibrated phase delay estimation and ambiguity-fixing in real-time precise point positioning, *J. Geodesy*, 87, 405–416, <https://doi.org/10.1007/s00190-013-0611-x>, 2013.
- Li, Z., Yuan, Y., Wang, N., Hernandez-Pajares, M., and Huo, X.: SHPTS: towards a new method for generating precise global ionospheric TEC map based on spherical harmonic and generalized trigonometric series functions, *J. Geodesy*, 89, 331–345, <https://doi.org/10.1007/s00190-014-0778-9>, 2015.
- Li, Z., Wang, N., Hernández Pajares, M., Yuan, Y., Krankowski, A., Liu, A., Zha, J., García Rigo, A., Roma-Dollase, D., Yang, H., Laurichesse, D., and Blot, A.: IGS real-time service for global ionospheric total electron content modeling, *J. Geodesy*, 94, 32, <https://doi.org/10.1007/s00190-020-01360-0>, 2020.
- Liu, J.-Y., Chen, Y., Chuo, Y., and Chen, C.-S.: A statistical investigation of preearthquake ionospheric anomaly, *J. Geophys. Res.-Space*, 111, A05304, <https://doi.org/10.1029/2005JA011333>, 2006.
- Liu, L., Wan, W., Ning, B., and Zhang, M.-L.: Climatology of the mean total electron content derived from GPS global ionospheric maps, *J. Geophys. Res.-Space*, 114, A06308, <https://doi.org/10.1029/2009JA014244>, 2009.
- Liu, Q. and Hernández-Pajares, M.: The archive of IGS combined real-time GIM [data set], available at: <http://chapman.upc.es/irtg/archive>, last access: 10 September 2021a.
- Liu, Q. and Hernández-Pajares, M.: The latest results of IGS combined real-time GIM [data set], available at: [http://chapman.upc.es/irtg/last\\_results](http://chapman.upc.es/irtg/last_results), last access: 10 September 2021b.
- Liu, Q., Hernández-Pajares, M., Lyu, H., and Goss, A.: Influence of temporal resolution on the performance of global ionospheric maps, *J. Geodesy*, 95, 34, <https://doi.org/10.1007/s00190-021-01483-y>, 2021a.
- Liu, Q., Hernández-Pajares, M., Yang, H., Monte-Moreno, E., Roma, D., García Rigo, A., Li, Z., Wang, N., Laurichesse, D., Blot, A., Zhao, Q., and Zhang, Q.: Global Ionosphere Maps of vertical electron content combined in real-time from the RT-GIMs of CAS, CNES, UPC-IonSAT, and WHU International GNSS Service (IGS) centers (from Dec 1, 2020, to March 1, 2021), Zenodo [data set], <https://doi.org/10.5281/zenodo.5042622>, 2021b.
- Loewe, C. and Prölss, G.: Classification and mean behavior of magnetic storms, *J. Geophys. Res.-Space*, 102, 14209–14213, <https://doi.org/10.1029/96JA04020>, 1997.
- Lou, Y., Zheng, F., Gu, S., Wang, C., Guo, H., and Feng, Y.: Multi-GNSS precise point positioning with raw single-frequency and dual-frequency measurement models, *GPS Solut.*, 20, 849–862, <https://doi.org/10.1007/s10291-015-0495-8>, 2016.
- Mannucci, A., Wilson, B., Yuan, D., Ho, C., Lindqwister, U., and Runge, T.: A global mapping technique for GPS-derived ionospheric total electron content measurements, *Radio Sci.*, 33, 565–582, <https://doi.org/10.1029/97RS02707>, 1998.
- Orús, R., Hernández-Pajares, M., Juan, J., and Sanz, J.: Improvement of global ionospheric VTEC maps by using kriging interpolation technique, *J. Atmos. Sol.-Terr. Phys.*, 67, 1598–1609, <https://doi.org/10.1016/j.jastp.2005.07.017>, 2005.
- Ren, X., Chen, J., Li, X., Zhang, X., and Freeshah, M.: Performance evaluation of real-time global ionospheric maps provided by different IGS analysis centers, *GPS Solut.*, 23, 113, <https://doi.org/10.1007/s10291-019-0904-5>, 2019.
- Roma-Dollase, D., Gómez Cama, J. M., Hernández Pajares, M., and García-Rigo, A.: Real-time Global Ionospheric modelling from GNSS data with RT-TOMION model, in: 5th International Colloquium Scientific and Fundamental Aspects of the Galileo Programme, Braunschweig, Germany, 27–29 October 2015.
- Roma-Dollase, D., Hernández-Pajares, M., García Rigo, A., Krankowski, A., Fron, A., Laurichesse, D., Blot, A., Orús-Pérez, R., Yuan, Y., Li, Z., Wang, N., Schmidt, M., and Erdogan, E.: Looking for optimal ways to combine global ionospheric maps in real-time, in: IGS workshop 2018, Wuhan, 29 October–2 November, 2018a.
- Roma-Dollase, D., Hernández-Pajares, M., Krankowski, A., Kotulak, K., Ghoddousi-Fard, R., Yuan, Y., Li, Z., Zhang, H., Shi, C., Wang, C., Feltens, J., Vergados, P., Komjathy, A., Schaer, S., García-Rigo, A., and Gómez-Cama, J. M.: Consistency of seven different GNSS global ionospheric mapping techniques during one solar cycle, *J. Geodesy*, 92, 691–706, <https://doi.org/10.1007/s00190-017-1088-9>, 2018b.
- RTCM-SC: Proposal of new RTCM SSR messages, SSR Stage 2: Vertical TEC (VTEC) for RTCM Standard 10403.2 Differential GNSS (global navigation satellite system) Services – Version 3, RTCM Special Committee, 104, 2014.
- Schaer, S., Beutler, G., Rothacher, M., and Springer, T. A.: Daily global ionosphere maps based on GPS carrier phase data routinely produced by the CODE Analysis Center, in: Proceedings of the IGS AC Workshop, Silver Spring, MD, USA, 19–21 March, 1996.
- Schaer, S., Gurtner, W., and Feltens, J.: IONEX: The ionosphere map exchange format version 1, in: Proceedings of the IGS AC workshop, Darmstadt, Germany, 9–11 February 1998, vol. 9, 1998.
- Sezen, U., Arikan, F., Arikan, O., Ugurlu, O., and Sadeghimorad, A.: Online, automatic, near-real time estimation of GPS-TEC: IONOLAB-TEC, *Space Weather*, 11, 297–305, <https://doi.org/10.1002/swe.20054>, 2013.
- Sotomayor-Beltran, C., Sobey, C., Hessels, J., De Bruyn, G. et al.: Calibrating high-precision Faraday rotation measurements for LOFAR and the next generation of low-frequency radio telescopes, *Astron. Astrophys.*, 552, A58, <https://doi.org/10.1051/0004-6361/201220728>, 2013.
- Tange, O.: Gnu parallel-the command-line power tool, *The USENIX Magazine*, 36, 42–47, <https://doi.org/10.5281/zenodo.16303>, 2011.
- Tomaszewski, D., Wielgosz, P., Rapiński, J., Krypiak-Gregorczyk, A., Kaźmierczak, R., Hernández-Pajares, M., Yang, H., and OrúsPérez, R.: Assessment of Centre National d'Etudes Spatiales Real-Time Ionosphere Maps



- in Instantaneous Precise Real-Time Kinematic Positioning over Medium and Long Baselines, *Sensors*, 20, 2293, <https://doi.org/10.3390/s20082293>, 2020.
- Wang, N., Li, Z., Duan, B., Hugentobler, U., and Wang, L.: GPS and GLONASS observable-specific code bias estimation: comparison of solutions from the IGS and MGEX networks, *J. Geodesy*, 94, 74, <https://doi.org/10.1007/s00190-020-01404-5>, 2020.
- Weber, G., Mervart, L., Lukes, Z., Rocken, C., and Dousa, J.: Real-time clock and orbit corrections for improved point positioning via NTRIP, in: Proceedings of the 20th international technical meeting of the satellite division of the institute of navigation (ION GNSS 2007), Fort Worth, USA, 25–28 September 2007, pp. 1992–1998, 2007.
- Weber, G., Mervart, L., Stürze, A., Rülke, A., and Stöcker, D.: BKG Ntrip Client, Version 2.12, vol. 49 of Mitteilungen des Bundesamtes für Kartographie und Geodäsie, Verlag des Bundesamtes für Kartographie und Geodäsie, Frankfurt am Main, 2016.
- Wright, J., Yang, A. Y., Ganesh, A., Sastry, S. S., and Ma, Y.: Robust face recognition via sparse representation, *IEEE T. Pattern Anal.*, 31, 210–227, <https://doi.org/10.1109/TPAMI.2008.79>, 2008.
- Wright, J., Ma, Y., Mairal, J., Sapiro, G., Huang, T. S., and Yan, S.: Sparse representation for computer vision and pattern recognition, *P. IEEE*, 98, 1031–1044, <https://doi.org/10.1109/JPROC.2010.2044470>, 2010.
- Yang, H., Monte-Moreno, E., Hernández-Pajares, M., and Romadollase, D.: Real-time interpolation of global ionospheric maps by means of sparse representation, *J. Geodesy*, 95, 71, <https://doi.org/10.1007/s00190-021-01525-5>, 2021.
- Zhang, B., Teunissen, P. J., Yuan, Y., Zhang, X., and Li, M.: A modified carrier-to-code leveling method for retrieving ionospheric observables and detecting short-term temporal variability of receiver differential code biases, *J. Geodesy*, 93, 19–28, <https://doi.org/10.1007/s00190-018-1135-1>, 2019.
- Zhang, H., Gao, Z., Ge, M., Niu, X., Huang, L., Tu, R., and Li, X.: On the convergence of ionospheric constrained precise point positioning (IC-PPP) based on undifferential uncombined raw GNSS observations, *Sensors*, 13, 15708–15725, <https://doi.org/10.3390/s131115708>, 2013a.
- Zhang, H., Xu, P., Han, W., Ge, M., and Shi, C.: Eliminating negative VTEC in global ionosphere maps using inequality-constrained least squares, *Adv. Space Res.*, 51, 988–1000, <https://doi.org/10.1016/j.asr.2012.06.026>, 2013b.
- Zhang, Q. and Zhao, Q.: Global ionosphere mapping and differential code bias estimation during low and high solar activity periods with GIMAS software, *Remote Sens.-Basel*, 10, 705, <https://doi.org/10.3390/rs10050705>, 2018.
- Zhang, Q. and Zhao, Q.: Analysis of the data processing strategies of spherical harmonic expansion model on global ionosphere mapping for moderate solar activity, *Adv. Space Res.*, 63, 1214–1226, <https://doi.org/10.1016/j.asr.2018.10.031>, 2019.
- Zhao, B., Wan, W., Liu, L., Mao, T., Ren, Z., Wang, M., and Christensen, A. B.: Features of annual and semiannual variations derived from the global ionospheric maps of total electron content, *Ann. Geophys.*, 25, 2513–2527, <https://doi.org/10.5194/angeo-25-2513-2007>, 2007.



# Influence of temporal resolution on the performance of global ionospheric maps

Qi Liu<sup>1</sup> · Manuel Hernández-Pajares<sup>1,2</sup> · Haixia Lyu<sup>1,2</sup> · Andreas Goss<sup>3</sup>

Received: 7 April 2020 / Accepted: 19 January 2021 / Published online: 22 February 2021  
© Springer-Verlag GmbH Germany, part of Springer Nature 2021

## Abstract

Global ionosphere maps (GIM) computed from dual-frequency GNSS measurements have been widely used for monitoring ionosphere as well as providing ionospheric corrections in Space Geodesy since 1998. This work focuses on a comprehensive study of the influence of time resolution on GIM performance. One and a half solar cycle of the IGS GIM with higher time resolution and accuracy (the UPC-IonSAT Quarter-of-an-hour time resolution Rapid GIM, AKA uqrg) has been taken as baseline to downsample them to all possible sub-daily temporal resolutions. The performance of the resulting GIMs has been assessed by directly comparing with external vertical total electron content (VTEC) measurements from Jason altimeters over oceanic regions. In order to perform a complete assessment and analysis of involved GIMs, the influence of geographical position and solar and geomagnetic activities was also taken into account during more than one solar cycle. In addition, to have a clear view at the smaller time resolutions, a more accurate assessment, the dSTEC test based on external GNSS measurements not used in the GIM generation was also done during two solstice and two equinox days in 2015 over continental regions. The assessment shows that discrepancy among GIMs with different time resolutions becomes more apparent at low latitudes and also at high solar-geomagnetic activity. The results also suggest that the accuracy for GIMs with time resolution smaller or equal to 60 min is consistent during the period from 2002 to 2019 and is more accurate than other GIMs with lower temporal resolution. Accordingly, high time resolution (including 15, 30, 45 and 60 min) is recommended for the application of GIMs with the highest accuracy.

**Keywords** Global Navigation Satellite Systems · Ionosphere · Global ionospheric map · Temporal resolution · Vertical total electron content · Jason

## ATTENTION<sub>ii</sub>

Pages 58 to 73 of the thesis, containing the article mentioned above  
are available at the editor's web

<https://link.springer.com/article/10.1007/s00190-021-01483-y>



## RESEARCH ARTICLE

10.1029/2021SW002926

### Key Points:

- A new ionospheric temporal and spatial gradient index based on UPC-IonSAT Global Ionosphere Maps (UQRG) are presented at the selected region
- The new ionospheric spatial gradients indices at grid points of UQRG are presented
- The derived ionospheric spatial gradients and temporal variations indices are analyzed during quiet and disturbed ionosphere states

### Correspondence to:

M. Hernández-Pajares,  
manuel.hernandez@upc.edu

### Citation:

Liu, Q., Hernández-Pajares, M., Yang, H., Monte-Moreno, E., García-Rigo, A., Lyu, H., et al. (2022). A new way of estimating the spatial and temporal components of the Vertical Total Electron Content gradient based on UPC-IonSAT Global Ionosphere Maps. *Space Weather*, 20, e2021SW002926. <https://doi.org/10.1029/2021SW002926>

Received 22 SEP 2021  
Accepted 11 JAN 2022

# A New Way of Estimating the Spatial and Temporal Components of the Vertical Total Electron Content Gradient Based on UPC-IonSAT Global Ionosphere Maps

Qi Liu<sup>1</sup> , Manuel Hernández-Pajares<sup>1,2</sup> , Heng Yang<sup>1,3</sup> , Enric Monte-Moreno<sup>4</sup> , Alberto García-Rigo<sup>1,2</sup> , Haixia Lyu<sup>1,5</sup> , Germán Olivares-Pulido<sup>1</sup> , and Raül Orús-Pérez<sup>6</sup>

<sup>1</sup>Universitat Politècnica de Catalunya (UPC-IonSAT), Barcelona, Spain, <sup>2</sup>Institut d'Estudis Espacials de Catalunya (IEEC), Barcelona, Spain, <sup>3</sup>School of Electronic Information and Engineering, Yangtze Normal University, Chongqing, China, <sup>4</sup>Department of TSC, TALP, Universitat Politècnica de Catalunya, Barcelona, Spain, <sup>5</sup>GNSS Research Center, Wuhan University, Wuhan, China, <sup>6</sup>Wave Interaction and Propagation Section (TEC-EFW) ESA ESTEC, Noordwijk, The Netherlands

**Abstract** The determination of the ionospheric perturbation degree is essential to describe the ionosphere state for space weather monitoring. A new method for estimating the spatial and temporal components of the Vertical Total Electron Content (VTEC) gradient is introduced. The new method is based on VTEC estimated at each grid point of Global Ionosphere Map (GIM) by the UPC-IonSAT research group of the Universitat Politècnica de Catalunya. Depending on the requirement, the VTEC spatial gradients can be derived at selected regions or grid points of the GIM on a global scale. According to the comparison with previous studies over the Europe region during quiet ionosphere state and two severe geomagnetic storms, the new method has proven to be reliable and has a great potential for the monitoring of ionospheric perturbation degree on a global scale. In addition, the associated warning of disturbed ionosphere might be available in the context of the on-going development of real-time GIMs.

**Plain Language Summary** Space weather events in the space environment can significantly affect the performance of satellite navigation, positioning, and communications. Among the space weather events, the perturbations of the upper atmosphere of the earth, the ionosphere, can degrade the function of radio systems crossing the ionosphere. In this paper, a new method based on Global Ionosphere Maps for measuring the perturbation of the ionosphere on a global scale is presented and validated during quiet and disturbed ionosphere states.

## 1. Introduction

The fluctuations of the ionospheric electron density (i.e., ionosphere perturbations) have adverse impacts on the transionospheric radio signals including radar altimetry, radio communication systems, space-based remote sensing, and Global Navigation Satellite System (GNSS) positioning (e.g., Jakowski, Béniguel, et al., 2012; Jakowski, Borries, & Wilken, 2012; Monaldo, 1991). For example, due to the large fluctuations of the ionospheric electron density, the GPS stations experienced an outage at high latitude, and the Wide Area Augmentation System was disabled for few hours in the United States of America during the Halloween storm of 2003 (Doherty et al., 2004; Webb & Allen, 2004), which also affected to the Test Bed of the European Geostationary Navigation Overlay Service (EGNOS) in northern Europe (Hernández-Pajares et al., 2005). In addition, the EGNOS service was degraded during the ionospheric perturbation period of St. Patrick's Day storm in 2015. Consequently, it is important to identify the perturbation degree of the ionosphere to monitor the ionospheric state.

To characterize the amplitude and phase fluctuations of GNSS signals, the ionosphere scintillation index  $S_4$  and  $\sigma_\phi$  were introduced in 1981 (Rino et al., 1981). Based on Total Electron Content (TEC) from GNSS receivers, the Rate of Change of TEC Index (ROTI) was proposed as a measure of ionospheric irregularities (Pi et al., 1997). A new ionospheric perturbation index, Regional Ionosphere Disturbances Index, was based on regional Neustrelitz TEC Model (Jakowski et al., 2006). With data sets from the European Space Agency (ESA) Swarm constellation, the Ionospheric Bubble Index was generated as a level 2 product to provide information about Equatorial Plasma Bubbles (Park et al., 2013). A global ionospheric disturbance index map, W-index map, use the TEC from Global Ionosphere Map (GIM) refer to the median TEC value of preceding 7 days to

© 2022. The Authors.

This is an open access article under the terms of the [Creative Commons Attribution-NonCommercial-NoDerivs License](https://creativecommons.org/licenses/by-nc-nd/4.0/), which permits use and distribution in any medium, provided the original work is properly cited, the use is non-commercial and no modifications or adaptations are made.

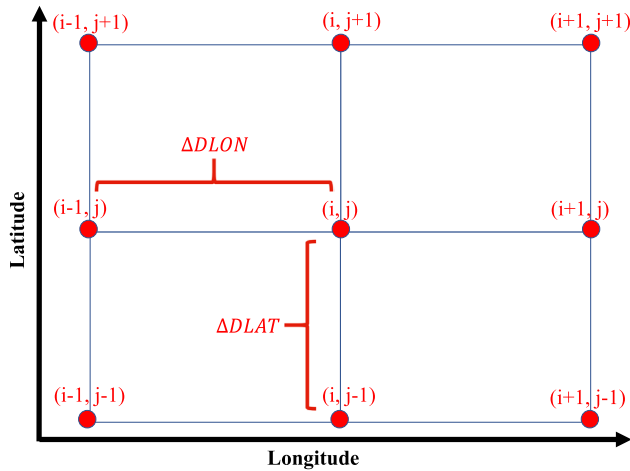


Figure 1. The diagram of grid points in Global Ionosphere Map.

identify the TEC perturbation level (Gulyaeva et al., 2013). In order to obtain objective measures of the ionosphere state, the Disturbance Ionosphere index (DIX) was calculated with differential GNSS carrier phase observations (Jakowski, Borries, & Wilken, 2012). The Disturbance Index Spatial Gradient was the modified DIX with a focus on spatial gradient (Wilken et al., 2018). An ionospheric scale index map based on DIX was proposed to characterize the TEC variation refer to the mean quiet ionospheric state (Denardini et al., 2020). Most of previous studies are targeted on the ionospheric scintillation, irregularities or the TEC perturbation refer to different types of reference values. With the purpose of calculating full (non-relative) values of TEC spatial gradients and temporal variations in a real-time scenario, the Gradient Ionosphere index (GIX) and Sudden Ionospheric Disturbance index (SIDX) were obtained from the TEC derived from raw GNSS pseudorange observations and tested in Europe (Jakowski & Hoque, 2019). However, such an approach for the calculation of TEC spatial gradient and temporal variation is only possible over the regions where GNSS receivers are installed.

In order to represent the distribution of Vertical Total Electron Content (VTEC) on a global scale, different global ionospheric models have been developed. For instance, the spherical harmonic model was proposed for global VTEC representation in 1995 (Schaer et al., 1995) and has been modified in following researches (e.g., Feltens, 2007; Ghoddousi-Fard, 2014; H. Zhang et al., 2013; Li et al., 2015; Q. Zhang & Zhao, 2019; Roma-Dollase et al., 2018). The tomographic TEC model with a two-layer assumption was developed by Universitat Politècnica de Catalunya (UPC; Hernández-Pajares et al., 1998, 1999, 2000). To define the format of GIM generated by the global ionospheric model, the IONosphere map EXchange (IONEX) format was proposed and widely used by GNSS communities (Schaer et al., 1998). The Kriging interpolation technique was introduced to improve the accuracy of UPC tomographic model. In addition, the temporal resolution of the associated UPC GIMs was increased to 15 min (Orús et al., 2005). Such GIM, UPC-IonSAT Quarter-of-an-hour time resolution Rapid GIM (UQRG), is one of the most accurate ones (Liu, Hernández-Pajares, Lyu, & Goss, 2021; Roma-Dollase et al., 2018). And, it has been

demonstrated that the UQRG can provide realistic VTEC features in polar regions with few GNSS receivers available. Therefore, the tomographic model and interpolation technique of UQRG are reliable for the global VTEC representation (Hernández-Pajares, Lyu, Aragón-Àngel, et al., 2020).

In this paper, we propose a new way of estimating the spatial and temporal components of the VTEC gradient from UQRG GIMs. The new method is able to provide spatial gradients and temporal variations on a global and regional scale in a fast and compact way following the IONEX format.

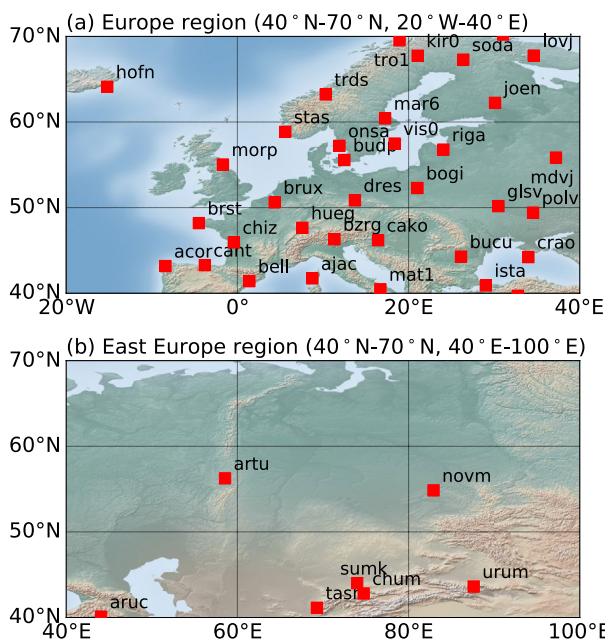


Figure 2. The distribution of stations for generating UPC-IonSAT Quarter-of-an-hour time resolution Rapid GIM at the selected Europe region (40°–70°N and 20°W–40°E) and East Europe region (40°–70°N and 40°–100°E).

## 2. Data and Methods

The UQRG GIM is based on GNSS carrier phase observations only and it is being generated by the combination of tomographic model and Kriging interpolation technique on a daily basis and with latencies of less than 2 days. As it has been mentioned above, the temporal resolution of UQRG is 15 min and the global VTEC of UQRG is provided in terms of 5,183 grid points with a spatial resolution of 5° and 2.5° in longitude and latitude, respectively, and provided in IONEX format (Schaer et al., 1998).

### 2.1. Spatial Gradients of VTEC at Grid Points of GIM

Since the VTEC of GIM is provided at grid points, the spatial components of the gradient  $\nabla V$  at each grid point, VTEC grid Gradient indices based

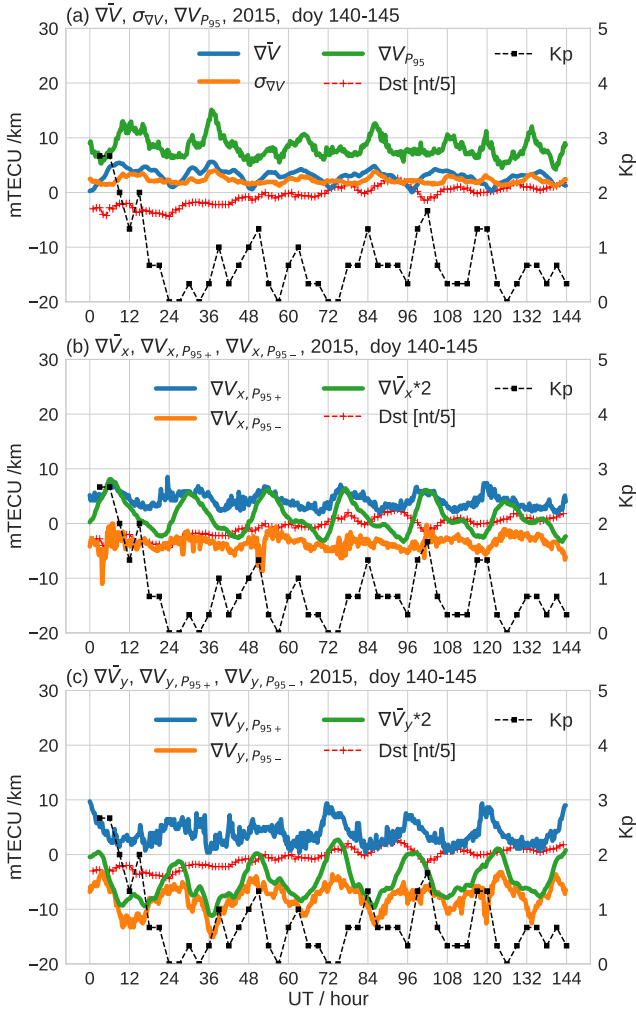


**Figure 3.** The evolution of Regional VTEC spatial Gradient indices based on UQRG at Europe ( $40^{\circ}$ – $70^{\circ}$ N and  $20^{\circ}$ W– $40^{\circ}$ E) during the geomagnetic quiet period 20–25 May 2015.

on UQRG (VGUG), can be divided into  $\nabla V_x$ ,  $\nabla V_y$ , and its module  $\nabla V$ , as Equation 1. And, the diagram of the grid points of GIM can be seen in Figure 1.

$$\begin{cases} \nabla V_{x,i,j} = (VTEC_{i,j} - VTEC_{i-1,j})/\Delta DLON \\ \nabla V_{y,i,j} = (VTEC_{i,j} - VTEC_{i,j-1})/\Delta DLAT \\ \nabla V_{i,j} = \sqrt{\nabla V_{x,i,j}^2 + \nabla V_{y,i,j}^2} \\ \vec{\nabla V} = (\nabla V_{x,i,j}, \nabla V_{y,i,j}) \end{cases} \quad (1)$$

where  $\nabla V_{x,i,j}$  is the zonal component of VTEC spatial gradient at grid point  $[i, j]$ , while  $i$  is the order of grid point  $[i, j]$  along the west–east direction and  $j$  is the order of grid point  $[i, j]$  along the south–north direction.  $VTEC_{i,j}$  and  $VTEC_{i-1,j}$  are the VTEC at grid points  $[i, j]$  and  $[i - 1, j]$ , respectively.  $\Delta DLON$  is the distance (km) between grid points  $[i, j]$  and  $[i - 1, j]$ , taking into account the corresponding latitude, for a range of  $[-75^{\circ}, 75^{\circ}]$  to avoid too close GIM grid points.  $\nabla V_{y,i,j}$  is the meridional component of VTEC spatial gradient at grid point  $[i, j]$ .  $VTEC_{i,j}$  and  $VTEC_{i,j-1}$  are the VTEC at grid points  $[i, j]$  and  $[i, j - 1]$ , respectively.  $\Delta DLAT$  is the distance (km) between grid points  $[i, j]$  and  $[i, j - 1]$ .

## 2.2. Spatial Gradients and Temporal Variations of VTEC Over the Selected Region

Similar to the definition of regional spatial gradient and temporal variation in Jakowski and Hoque (2019), the Regional VTEC spatial Gradient indices based on UQRG (RVGU) are defined. And RVGU include  $\overline{\nabla V}$ ,  $\sigma_{\nabla V}$ , and  $\nabla V_{P95}$  as shown in Equation 2.

$$\begin{cases} \overline{\nabla V} = \sum_{i=1}^N \sum_{j=1}^M \nabla V_{i,j} / N_S \\ \sigma_{\nabla V} = \sqrt{(\sum_{i=1}^N \sum_{j=1}^M \nabla V_{i,j}^2) / N_S - \overline{\nabla V}^2} \\ \nabla V_{P95} = P_{95}(\nabla V_{i,j}) \end{cases} \quad (2)$$

where  $N, M$  are the maximum numbers of zonal and meridional components considered at grid points within the selected region.  $N_S$  is the total number of grid points over the selected region.  $\overline{\nabla V}$  is the average of  $\nabla V_{i,j}$  over the selected region.  $\sigma_{\nabla V}$  is the standard deviation of VTEC spatial gradient over the selected region. The  $\nabla V_{P95}$  is the 95th percentile value of  $\nabla V_{i,j}$  over the selected region in Equation 2.

In addition, the RVGU include  $\overline{\nabla V_x}$ ,  $\nabla V_{x,P95+}$ ,  $\nabla V_{x,P95-}$ ,  $\overline{\nabla V_y}$ ,  $\nabla V_{y,P95+}$ , and  $\nabla V_{y,P95-}$  as Equation 3. It should be noted that the 95th percentiles of VTEC spatial gradient values over the selected region,  $\nabla V_{x,P95\pm}$  and  $\nabla V_{y,P95\pm}$ , have negative and positive values for both zonal (eastward or westward) component and meridional (northward or southward) component of VTEC spatial gradients.  $\nabla V_{x,P95\pm}$  and  $\nabla V_{y,P95\pm}$  represent zonal (eastward or westward) component and meridional (northward or southward) component of VTEC spatial gradients, respectively. And, the eastward gradient for zonal component and northward gradient for meridional component are defined as positive values, while westward gradient and southward gradient are negative values.

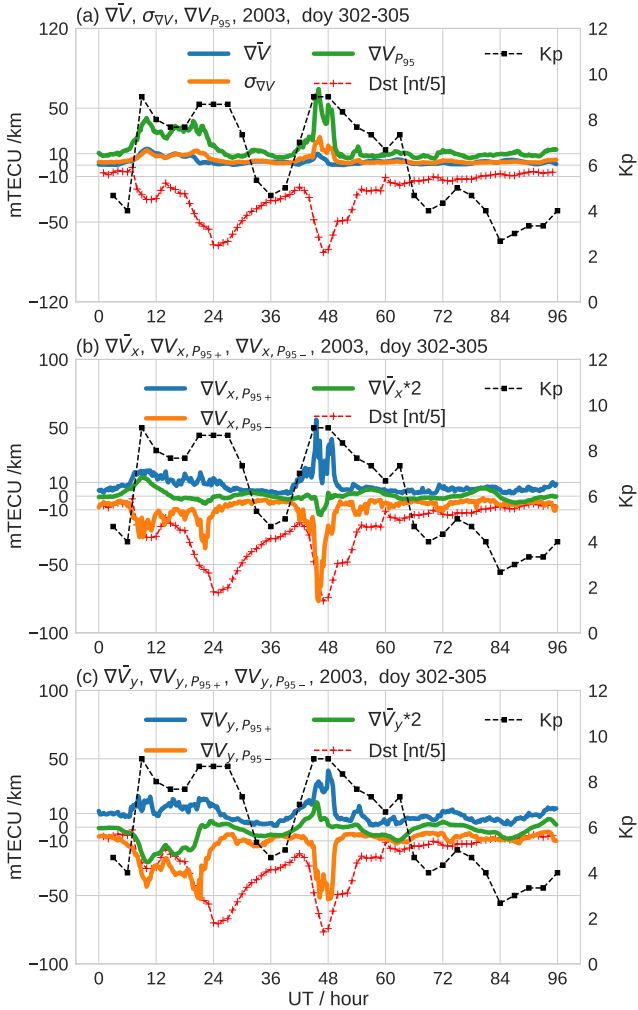


**Figure 4.** The evolution of Regional VTEC spatial Gradient indices based on UQRG at Europe (40°–70°N and 20°W–40°E) during the Halloween storm 28 October to 1 November 2003.

### 3. Results and Analysis

In this section, the performance of VTEC spatial gradient and temporal variation indices at Europe region and grid points is analyzed. It should be noted that VGUG and RVGU are just generic terms about VTEC grid gradient indices and regional VTEC spatial gradient indices based on UQRG.

#### 3.1. Regional VTEC Spatial Gradients and Temporal Variations

In order to show the level of regional VTEC spatial gradients, RVGU, over Europe region (40°–70°N and 20°W–40°E) in a quiet ionospheric state, the period from 20 May to 25 May of 2015 was selected. The Europe region is defined as (40°–70°N and 20°W–40°E) for a clear comparison with the results of Jakowski and Hoque (2019). And, the map of selected Europe region (40°–70°N and 20°W–40°E) can be seen in Figure 2a. It should be noted that, the range of Europe region in this section is slightly different from Jakowski and Hoque (2019) due to the lack of GNSS receivers in the southeast corner of the selected region in Jakowski and Hoque (2019). As it can be seen in Figure 2b, the East Europe region (40°–70°N and 40°–100°E) is selected to show the performance of regional VTEC spatial gradients (RVGU) with few GNSS receivers.

$$\left\{ \begin{array}{l} \overline{\nabla V_x} = \sum_{i=1}^N \sum_{j=1}^M \nabla V_{x,i,j} / N_S \\ \nabla V_{x,P95+} = P_{95}(\nabla V_{x,i,j,p}) \\ \nabla V_{x,P95-} = -P_{95}(|\nabla V_{x,i,j,n}|) \\ \overline{\nabla V_y} = \sum_{i=1}^N \sum_{j=1}^M \nabla V_{y,i,j} / N_S \\ \nabla V_{y,P95+} = P_{95}(\nabla V_{y,i,j,p}) \\ \nabla V_{y,P95-} = -P_{95}(|\nabla V_{y,i,j,n}|) \end{array} \right. \quad (3)$$

where  $\overline{\nabla V_x}$  is the zonal component of VTEC spatial gradients over the selected region. The subscript  $p$  denotes positive and  $n$  denotes negative.  $\nabla V_{x,P95+}$  is the 95th percentiles of positive VTEC spatial gradient value  $\nabla V_{x,i,j,p}$  for zonal (eastward) component.  $\nabla V_{x,P95-}$  is the negative value of 95th percentiles of absolute VTEC spatial gradient  $|\nabla V_{x,i,j,n}|$  for zonal (westward) component.  $\overline{\nabla V_y}$  is the meridional component of VTEC spatial gradients over the selected region.  $\nabla V_{y,P95+}$  is the 95th percentiles of positive VTEC spatial gradient value  $\nabla V_{y,i,j,p}$  for meridional (northward) component.  $\nabla V_{y,P95-}$  is the negative value of 95th percentiles of absolute VTEC spatial gradient  $|\nabla V_{y,i,j,n}|$  for meridional (southward) component.

The Regional Ionospheric Disturbance index based on UQRG (RIDU) can be obtained as follows:

$$\left\{ \begin{array}{l} \dot{V}_{i,j} = \Delta VTEC_{i,j} / \Delta t = (VTEC_{i,j,t} - VTEC_{i,j,t-1}) / \Delta t \\ RIDU = \sum_{i=1}^n \sum_{j=1}^m \dot{V}_{i,j} \end{array} \right. \quad (4)$$

where  $\dot{V}_{i,j}$  is the temporal derivative of grid point  $[i, j]$ .  $\Delta VTEC_{i,j}$  is the difference between the VTEC of current epoch and previous epoch at grid point  $[i, j]$ .  $\Delta t$  is the time between current epoch and previous epoch (15 min for UQRG). RIDU is the regional temporal variations of grid points within the selected region.

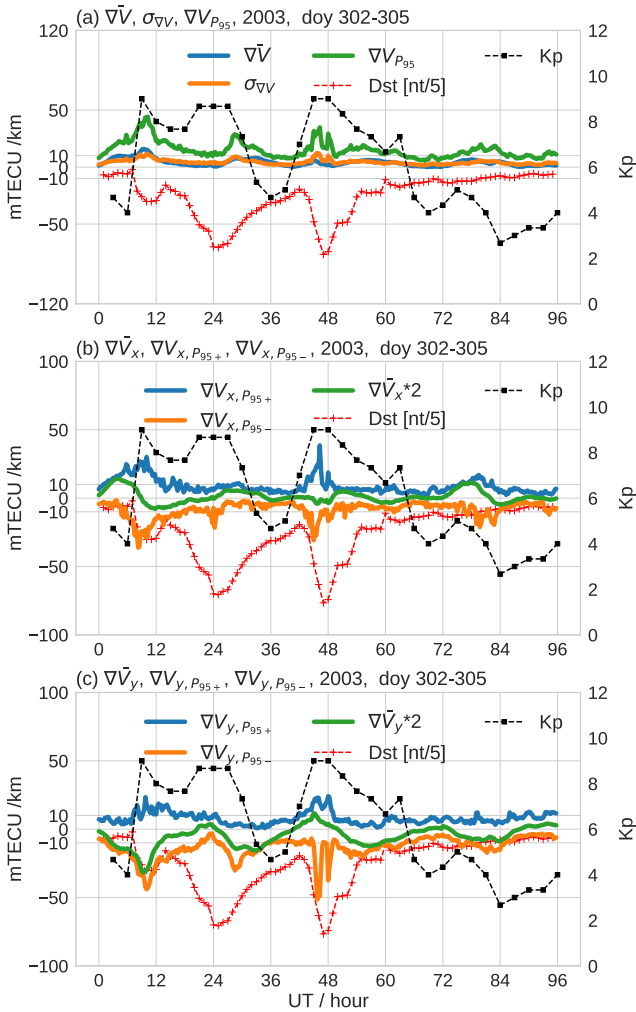


**Figure 5.** The evolution of Regional VTEC spatial Gradient indices based on UQRG at East Europe (40°–70°N and 40°–100°E) during the Halloween storm 28 October to 1 November 2003.

values. The VTEC distribution can also be affected by solar irradiation, electric field, photochemical process and plasma transport among other effects. As reported in previous studies (Liu et al., n.d.; Maruyama et al., 2013; Nishioka et al., 2017), the plasma stream is induced by the geomagnetic storm with the penetration electric fields and disturbance dynamo electric fields. And, the plasma stream produces the extreme TEC enhancement in Japan. Therefore, the VTEC spatial gradient indices should be used to describe the spatial perturbation degree of the ionosphere regardless of the source.

The reason why 95th percentile spatial gradient indices,  $\nabla V_{P95}$ ,  $\nabla V_{x,P95\pm}$ , and  $\nabla V_{y,P95\pm}$  are performing well, can be seen in Figure 7. The Figure 7 shows the evolution of box plots for  $\nabla V$ ,  $\nabla V_x$ , and  $\nabla V_y$  at Europe (40°–70°N and 20°W–40°E) during the Halloween storm. The box plots provide intuitive figures about the degree of dispersion and skewness in the spatial gradient values. For example, each box is calculated every 15 min in Figure 7a and it depicts the  $\nabla V$  values through their quartiles. The values of the orange line are the middle values of  $\nabla V$  in Figure 7a, while the higher end and lower end of bold black lines are 75th percentile (Q3) and 25th percentile (Q1) values of  $\nabla V$ , respectively. The higher end and lower end of light black lines are the  $Q3 + 1.5 \times (Q3 - Q1)$

In Figure 3b,  $\nabla V_{x,P95+}$  and  $\nabla V_{x,P95-}$  represent 95th percentiles of positive VTEC spatial gradient values (eastward) and negative VTEC spatial gradient values (westward), respectively. And  $\nabla V_{y,P95+}$  and  $\nabla V_{y,P95-}$  in Figure 3c represent 95th percentiles of positive VTEC spatial gradient values (northward) and negative VTEC spatial gradient values (southward), respectively. The  $\overline{\nabla V_x}$  and  $\overline{\nabla V_y}$  values are multiplied by 2 and the Dst is divided by 5 to obtain a clear comparison.

As can be seen in Figure 3, the VTEC spatial gradient indices RVGU range from around –10 to 10 during the geomagnetic quiet period 20–25 May 2015. In addition, the evolution of RVGU in Figure 3 shows the ability of VTEC spatial gradient indices to capture the small gradients in the order of 6–18 mTECU/km (1–3 mm/km, in GPS L1 delay units) and also the diurnal variation of VTEC spatial gradients (Jakowski & Hoque, 2019; Lee et al., 2006).

The performance of VTEC spatial gradient indices RVGU during two severe geomagnetic storms can be seen in Figures 4, 5 and 6. As shown in Figures 4 and 5, the  $\nabla V_{P95}$ ,  $\nabla V_{x,P95\pm}$ , and  $\nabla V_{y,P95\pm}$  are more sensitive than other regional self-defined indices ( $\nabla V$ ,  $\sigma_{\nabla V}$ ,  $\overline{\nabla V_x}$ ,  $\overline{\nabla V_y}$ ) to the geomagnetic activity in both Europe and East Europe regions. And the VTEC spatial gradient values tend to be larger when the geomagnetic activity increases (i.e., Kp index increases and Dst index decreases).

The main St. Patrick's Day storms started on 17 March 2015 and lasted for 5 days. The highest disturbance of VTEC can be seen in  $\nabla V_{P95}$ ,  $\nabla V_{x,P95\pm}$  and  $\nabla V_{y,P95\pm}$  around 36 UT and 41 UT in Figure 6. The evolution of  $\nabla V_{P95}$ ,  $\nabla V_{x,P95\pm}$ , and  $\nabla V_{y,P95\pm}$  is more related to Kp index than Dst index during the perturbed ionospheric state. In addition, the  $\nabla V_{y,P95\pm}$  values are larger than  $\nabla V_{x,P95\pm}$  during the perturbed ionospheric state. Hence, the ionospheric perturbation degree of South-North component is higher than West-East component during the perturbed ionospheric state of St. Patrick's Day storms.

As shown in Figures 4 and 6, the Kp index is more relevant than Dst index to the variation of VTEC spatial gradient values over the selected Europe region. Some previous studies investigating the ionospheric disturbances suggest that geomagnetic storms can cause strong disturbances in the electron density distribution and TEC (Biqiang et al., 2007; Vlasov et al., 2003). However, the evolution of VTEC spatial gradient values is not exactly the same as the variation of geomagnetic activity level. The geomagnetic activity level is not the only factor affecting the variation of VTEC spatial gradient

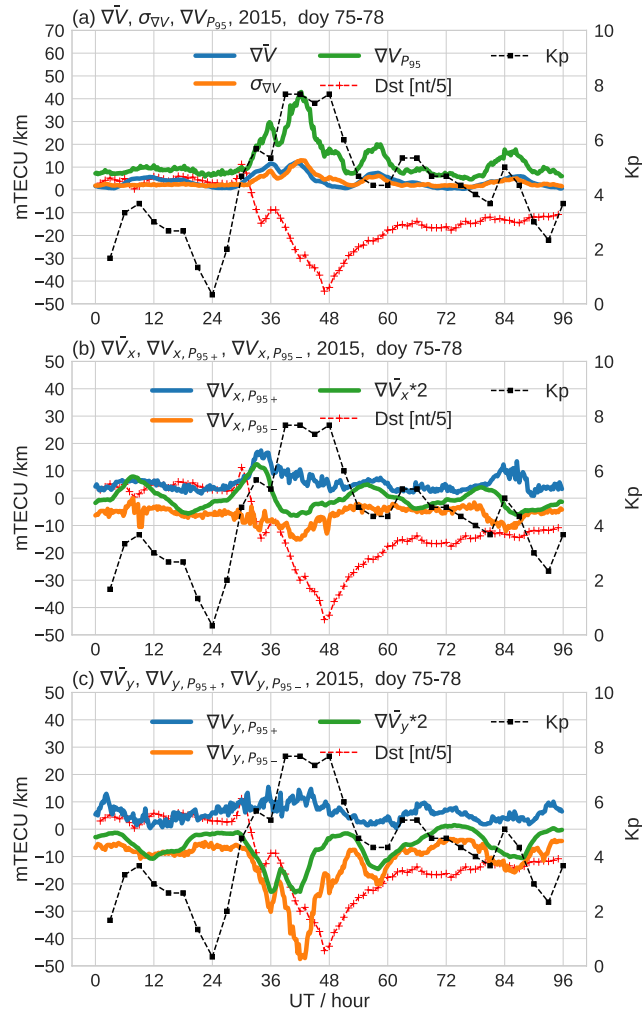


**Figure 6.** The evolution of Regional VTEC spatial Gradient indices based on UQRG at Europe (40°–70°N and 20°W–40°E) during the St. Patrick’s Day storm 16–20 March 2015.

and  $Q1 - 1.5 \times (Q3 - Q1)$  values of  $\nabla V$ , respectively. The higher end and lower end of light black lines are the boundaries of boxes. In addition, the outliers of VAUG values (red color) are outside the boxes.

As shown in Figure 7, the distributions of  $\nabla V$ ,  $\nabla V_x$ , and  $\nabla V_y$  at the selected Europe region have obvious skewness. Therefore, the negative and positive percentile values are both valuable. In addition, the long tail distributions due to the presence of extraordinary values in Figure 7 justify the great performance of 95th percentile spatial gradient indices  $\nabla V_{P95}$ ,  $\nabla V_{x,P95\pm}$ , and  $\nabla V_{y,P95\pm}$ .

As it can be seen in Figure 8, the regional index of VTEC temporal variation, RIDU, has a rapid increase during the very strong X-17.0 class solar flare on 28 October 2003. Nevertheless, the RIDU values are not sensitive to solar flares weaker than the one shown in Figure 8, due to the intrinsic temporal resolution of the GIMs (15 min). The smaller RIDU values are related to the temporal resolution of UQRG. Since the temporal resolution of UQRG is 15 min for RIDU and the temporal resolution of GNSS data is 1 s for SIDX, the RIDU values are typically lower than SIDX values. In addition, the RIDU values are not sensitive to the rapid VTEC variation due to the 15-min temporal resolution.



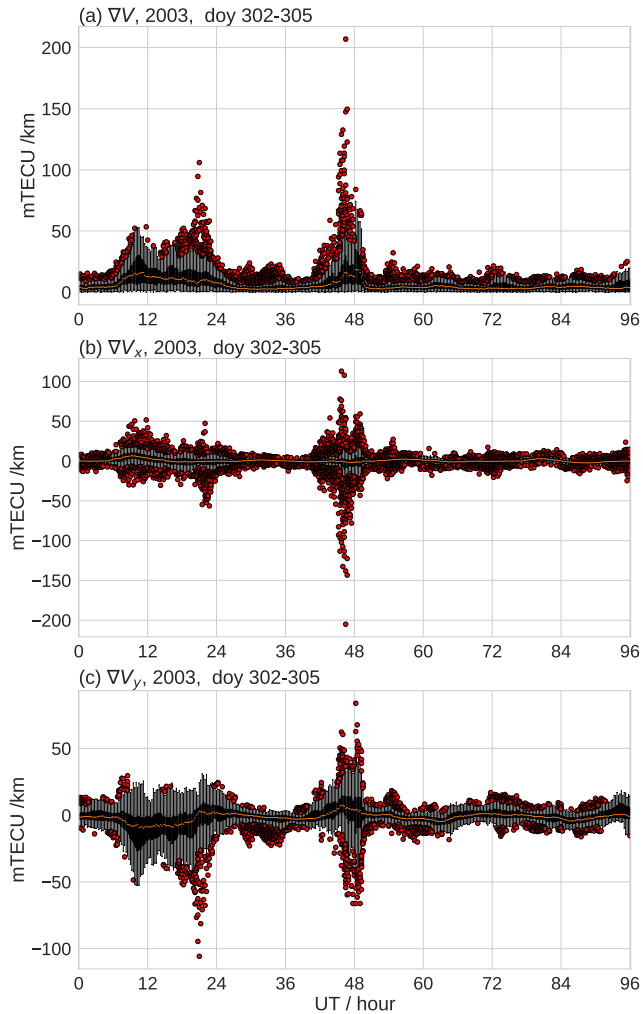


**Figure 7.** The evolution of box plot for  $\nabla V$ ,  $\nabla V_x$ , and  $\nabla V_y$  at Europe ( $40^{\circ}$ – $70^{\circ}$ N and  $20^{\circ}$ W– $40^{\circ}$ E) during the Halloween storm 28 October to 1 November 2003. (a) The evolution of  $\nabla V$ . (b) The evolution of  $\nabla V_x$ . (c) The evolution of  $\nabla V_y$ .

### 3.2. VTEC Spatial Gradients at Grid Points

As reported in (Jakowski & Hoque, 2019), the EGNOS for Aalborg station is affected by the ionospheric perturbations resulting from St. Patrick's Day storm. Since the Aalborg station is located at [ $57^{\circ}$ N and  $10^{\circ}$ E], the grid point [ $55^{\circ}$ N and  $10^{\circ}$ E] close to Aalborg station is selected to see the performance of VGUG. And the increase of Kp and the decrease of Dst might account for the sudden increase of  $\nabla V_{P_{95}}$  around 12 UT in Figure 9a. In addition, the performance of  $\nabla V_x$ , and  $\nabla V_y$  around Aalborg station [ $57^{\circ}$ N and  $10^{\circ}$ E] in Figure 9b is consistent with  $\nabla V_{P_{95}}$  in Figure 9a.

Since the grid points of UQRG are distributed on a global scale, the global map of VTEC spatial gradients at each grid point can be derived. As shown in Figure 9, the RVGU at Europe ( $40^{\circ}$ – $70^{\circ}$ N and  $20^{\circ}$ W– $40^{\circ}$ E) reached a peak around 18 UT of 17 March 2015 when the geomagnetic indices Kp and Dst are also high. In Figure 10, the behavior of VTEC spatial gradients on 18 UT of 17 March 2015 are compared with the previous quiet day (16 March 2015). The high southward VTEC gradients at Europe ( $40^{\circ}$ – $70^{\circ}$ N and  $20^{\circ}$ W– $40^{\circ}$ E) in Figure 9 is also clear in Figure 10d. In addition, the high VTEC gradients of zonal, meridional, and temporal components are also obvious compared to the previous geomagnetic quiet day around grid point [ $75^{\circ}$ S and  $60^{\circ}$ W] in Figures 10b, 10d and 10f.

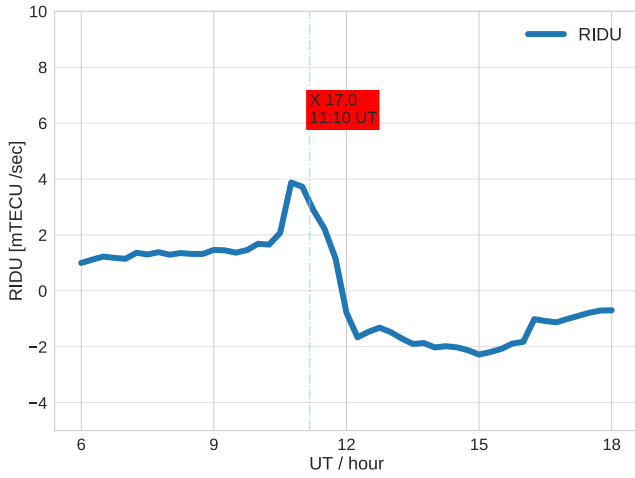


**Figure 8.** The evolution of Regional Ionospheric Disturbance index based on UQRG at Europe (40°–70°N and 20°W–40°E) on 28 October 2003 when a strong X-17.0 solar flare happened.

#### 4. Discussion

The main difference between the proposed method and Jakowski and Hoque (2019) is the calculation of VTEC and the distribution of VTEC gradient values. VTEC values of the proposed method are directly derived from UQRG, and the border of UQRG at the selected region take into account the data outside the region during the generation of UQRG. The VTEC values of Jakowski and Hoque (2019) use the VTEC from raw GNSS data of ground receivers inside the selected region. The TEC gradient values from the proposed method are derived at each grid point at the selected region, while the TEC gradient values from Jakowski and Hoque (2019) are based on TEC between ionospheric piercing points around receivers.

Despite the difference between the proposed method and Jakowski and Hoque (2019), both of these two methods are targeted on the full (non-relative) values of VTEC spatial gradients and temporal changes. As shown in Figure 4, the evolution of the VTEC spatial gradient indices is similar to Figure 7 of Jakowski and Hoque (2019). And, the VTEC spatial gradient values of Figure 6 are typically smaller than the values shown in Figure 8 of Jakowski and Hoque (2019) in agreement with an expected certain smoothing effect associated with the GIM resolution. But, the evolution of the VTEC spatial gradient indices in Figure 4 is similar to Figure 8 of Jakowski and Hoque (2019). The evolution of  $\nabla V_{P_{95}}$  in Figure 9a is similar to the gradient index 95% in Figure 10 of Jakowski and Hoque (2019), with an exception due to the different calculation methods and distribution of observations around 12 UT on 17 March 2015. The rise of  $\nabla V_{P_{95}}$  in Figure 9a around 16 UT is consistent with the reported growth of gradient index 95% in Figure 10 of Jakowski and Hoque (2019). In addition, the evolution of  $\nabla V_{P_{95}}$  in Figure 9a is consistent with the evolution of 95% of vertical positioning error in Figure 10 of Jakowski and Hoque (2019), which indicates the performance of GNSS positioning service. When the vertical positioning error is high, the GNSS Satellite-Based Augmentation System service can be degraded and even disabled.

In order to compare the proposed RVGU with the level of ionospheric irregularities, the regional ROTI indices are introduced. The calculation of the regional ROTI indices can be seen as follows:

$$\begin{cases} \overline{ROTI} = \sum_{k=1}^{N_R} ROTI_k / N_R \\ ROTI_{P_{95}} = P_{95}(ROTI_k) \end{cases} \quad (5)$$

where  $N_R$  is the total numbers of ROTI values calculated from GNSS receivers within the selected region (Pi et al., 1997).  $\overline{ROTI}$  is the average of  $ROTI_k$  over the selected region.  $ROTI_{P_{95}}$  is the 95th percentile value of  $ROTI_k$  over the selected region.

As can be seen in Figure 11, the blue line represents the 95th percentiles of ROTI values, and the orange line is the averaged ROTI values both at Europe (40°–70°N and 20°W–40°E). According to the original definition, the ROTI is directly defined as the variability (standard deviation) index of the TEC gradient (rate of TEC). It is clear in Figure 11 that the typical low value of  $ROTI_{P_{95}}$  before 07 UT approximately, coincident with quite constant gradient, is not maintained any more afterward. Indeed, the  $ROTI_{P_{95}}$  is always greater than 0.2 TECU/min after 07 UT, coinciding with continuous variability of the gradient index  $\nabla V_{P_{95}}$ .

As shown in Figure 11, the level of ionospheric irregularities at Europe (40°–70°N and 20°W–40°E),  $ROTI_{P_{95}}$ , reaches around 2 TECU/min on 13 UT and

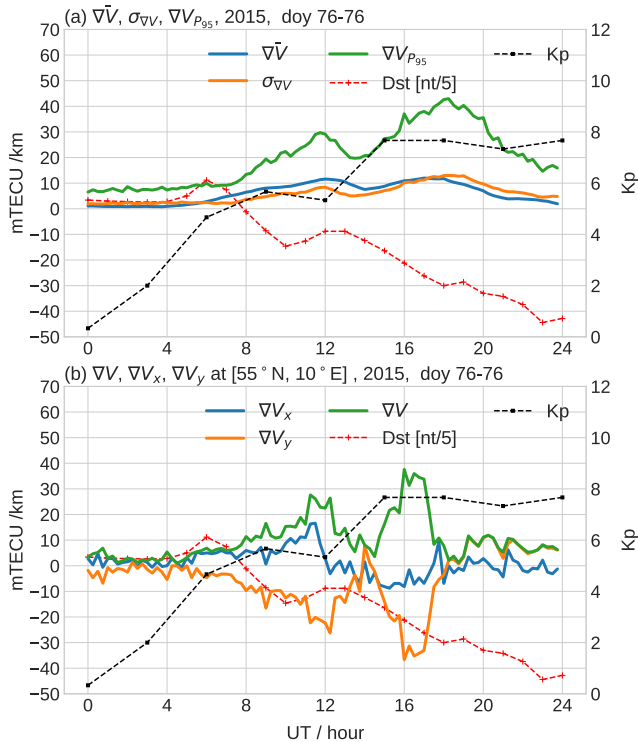


**Figure 9.** The evolution of Regional VTEC spatial Gradient indices based on UQRG at Europe (40°–70°N and 20°W–40°E) and the evolution of VGUG at grid point (55°N and 10°E) on 17 March 2015. (a) The evolution of Regional VTEC spatial Gradient indices based on UQRG. (b) The evolution of VGUG.

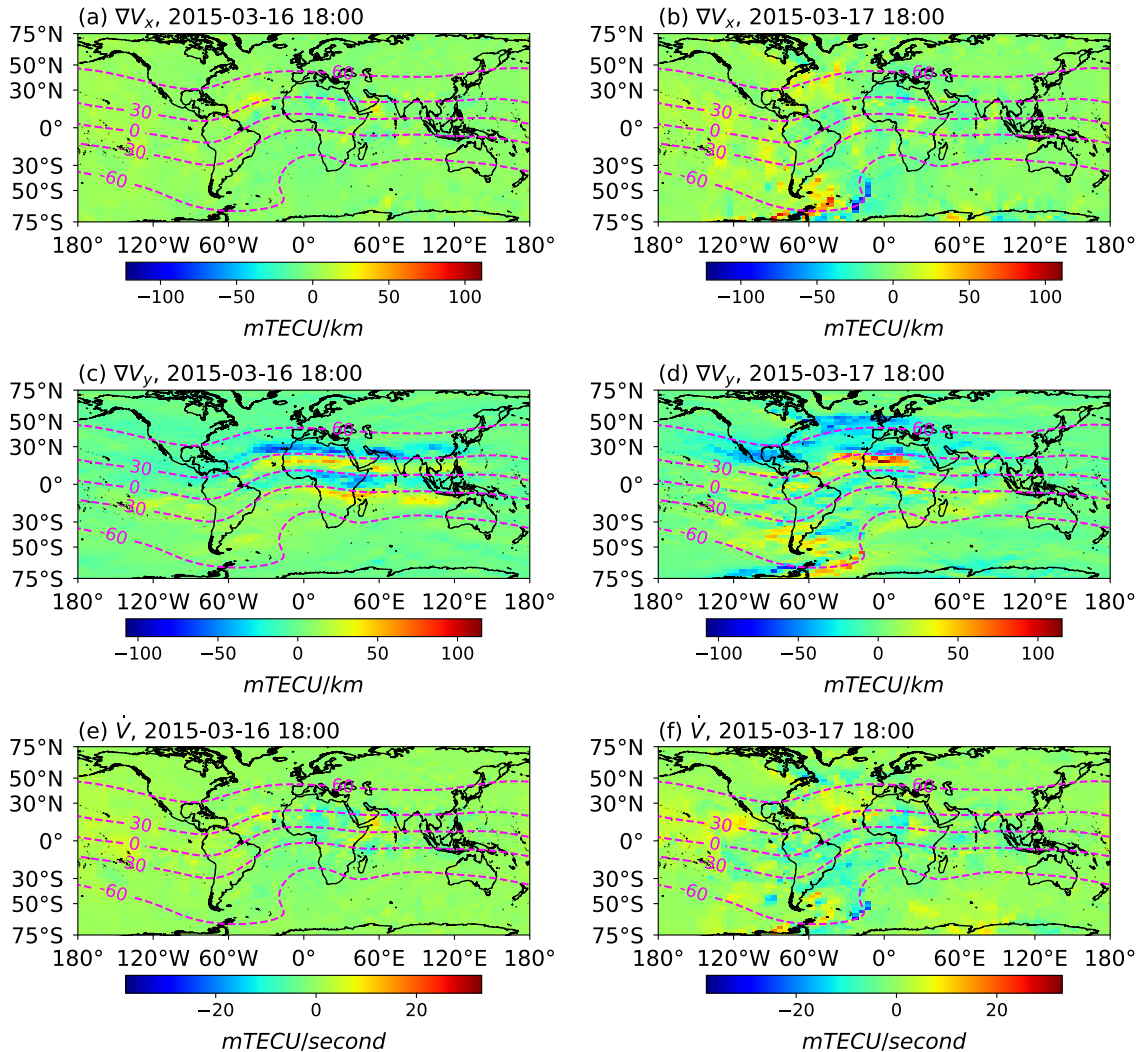


**Figure 10.** The global map of  $\nabla V_x$ ,  $\nabla V_y$ , and  $\dot{V}_{i,j}$  for a latitudinal range of  $(-75^\circ, 75^\circ)$  on 18 UT of 16–17 March 2015. (a) The global map of  $\nabla V_x$  on 18 UT of 16 March 2015. (b) The global map of  $\nabla V_x$  on 18 UT of 17 March 2015. (c) The global map of  $\nabla V_y$  on 18 UT of 16 March 2015. (d) The global map of  $\nabla V_y$  on 18 UT of 17 March 2015. (e) The global map of  $\dot{V}$  on 18 UT of 16 March 2015. (f) The global map of  $\dot{V}$  on 18 UT of 17 March 2015. The magenta dashed lines are for the geomagnetic dip angles.

started to increase rapidly from 13 UT of 16 March 2015 when the regional VTEC gradient index  $\nabla V_{P_{95}}$  also began to grow. In this regard, the evolution of the gradient index  $\nabla V_{P_{95}}$  is qualitatively consistent with the evolution of the regional ROTI index  $ROTI_{P_{95}}$ .

## 5. Conclusions

The new way of estimating the spatial and temporal components of the ionospheric VTEC gradient, based on UQRG GIM, has been introduced and validated during a quiet geomagnetic period of 2015, Halloween storm, and St. Patrick's Day storm. They provide a realistic estimation at time scales similar or larger than the GIM temporal resolution of 15 min.

The spatial components of the VTEC gradient have been estimated at each grid point of GIM (VGUG) and at the selected region (RVGU). Although VTEC regional gradient indices based on UQRG, RVGU, are smaller compared with GIX of Jakowski and Hoque (2019), the evolution of RVGU is consistent with GIX. In particular, the  $\nabla V_{P_{95}}$ ,  $\nabla V_{x,P_{95\pm}}$ , and  $\nabla V_{y,P_{95\pm}}$  are more sensitive than other regional self-defined indices ( $\overline{\nabla V}$ ,  $\sigma_{\nabla V}$ ,  $\overline{\nabla V_x}$ , and  $\overline{\nabla V_y}$ ) to the ionospheric perturbations over the selected Europe region and thus suitable as the regional VTEC spatial

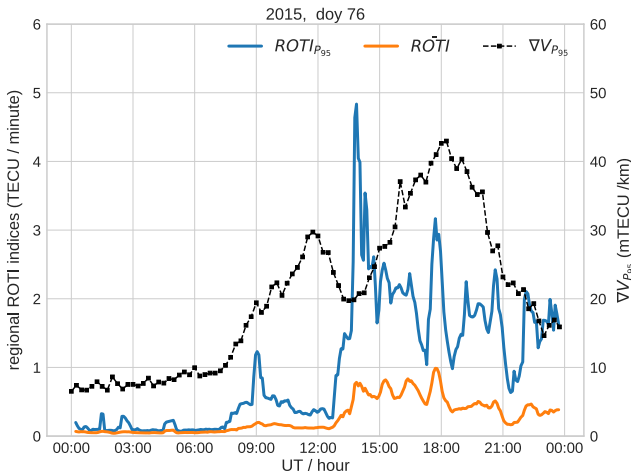


**Figure 11.** The evolution of regional Rate of Change of TEC Index (ROTI) indices at Europe ( $40^{\circ}$ – $70^{\circ}$ N and  $20^{\circ}$ W– $40^{\circ}$ E) during the St. Patrick's Day storm 17 March 2015. The blue line is the 95th percentiles of ROTI values, while the orange line is the averaged ROTI values at the selected Europe region ( $40^{\circ}$ – $70^{\circ}$ N and  $20^{\circ}$ W– $40^{\circ}$ E). The black line is the 95th percentile value of  $VV_{i,j}$  over the selected Europe region ( $40^{\circ}$ – $70^{\circ}$ N and  $20^{\circ}$ W– $40^{\circ}$ E).

gradient indices. As shown in Figures 2b and 5, the regional gradient indices is also able to capture the ionospheric perturbations where GNSS receivers are sparse. Accordingly, the proposed regional gradient indices open a new way to estimate the ionospheric perturbation degree at regions where few GNSS receivers are available.

The RVGU and VGUG might be the potential indicators for the degradation of GNSS positioning service as discussed in Section 4. In addition, the global map of VTEC spatial and temporal gradients at each grid point (similar to Figure 10) can be helpful to investigate the behavior of ionospheric perturbations on a global scale.

The future expected research in this topic can include:

1. To investigate the possibility and reliability of monitoring the ionospheric perturbation degree in real-time with the newly developed real-time GIMs (Li et al., 2020; Liu, Hernández-Pajares, Yang, et al., 2021; Yang et al., 2021).
2. To increase the spatial and temporal resolution of GIM for capturing small-scale ionospheric perturbations and rapid VTEC variations. The resolution of GIM might be improved by the better coverage station and multi-GNSS measurements (not just GPS). Moreover, the assimilation of multiple techniques (such as LEO satellites, DORIS, vessels) might also enhance the resolution of GIM (Hernández-Pajares, Lyu, Garcia-Fernandez, & Orus-Perez, 2020).

## Data Availability Statement

The UQRG data are openly accessible (<https://cdadis.nasa.gov/archive/gnss/products/ionex>) from Crustal Dynamics Data Information System (Noll, 2010). The Kp index is available (<https://datapub.gfz-potsdam.de/download/10.5880.Kp.0001>) from GeoForschungsZentrum (Matzka et al., 2021) and Dst index is accessible (<http://wdc.kugi.kyoto-u.ac.jp/dstdir/>) from World Data Center for Geomagnetism, Kyoto (World Data Center for Geomagnetism, Kyoto et al., 2015).

## References

- Biqiang, Z., Weixing, W., Libo, L., & Tian, M. (2007). Morphology in the total electron content under geomagnetic disturbed conditions: Results from global ionosphere maps. *Annales Geophysicae*, 25(7), 1555–1568. <https://doi.org/10.5194/angeo-25-1555-2007>
- Denardini, C., Picanço, G., Barbosa Neto, P., Nogueira, P., Carmo, C., Resende, L., et al. (2020). Ionospheric scale index map based on TEC data for space weather studies and applications. *Space Weather*, 18(9), e2019SW002328. <https://doi.org/10.1029/2019sw002328>
- Doherty, P., Coster, A. J., & Murtagh, W. (2004). Space weather effects of October–November 2003. *GPS Solutions*, 8(4), 267–271. <https://doi.org/10.1007/s10291-004-0109-3>
- Feltens, J. (2007). Development of a new three-dimensional mathematical ionosphere model at European Space Agency/European Space Operations Centre. *Space Weather*, 5(12), S12002. <https://doi.org/10.1029/2006SW000294>
- Ghoddousi-Fard, R. (2014). GPS ionospheric mapping at Natural Resources Canada. In *IGS workshop*.
- Gulyaeva, T. L., Arikani, F., Hernandez-Pajares, M., & Stanislawska, I. (2013). GIM-TEC adaptive ionospheric weather assessment and forecast system. *Journal of Atmospheric and Solar-Terrestrial Physics*, 102, 329–340. <https://doi.org/10.1016/j.jastp.2013.06.011>
- Hernández-Pajares, M., Juan, J., & Sanz, J. (1999). New approaches in global ionospheric determination using ground GPS data. *Journal of Atmospheric and Solar-Terrestrial Physics*, 61(16), 1237–1247. [https://doi.org/10.1016/S1364-6826\(99\)00054-1](https://doi.org/10.1016/S1364-6826(99)00054-1)
- Hernández-Pajares, M., Juan, J., Sanz, J., & Colombo, O. L. (2000). Application of ionospheric tomography to real-time GPS carrier-phase ambiguities Resolution, at scales of 400–1000 km and with high geomagnetic activity. *Geophysical Research Letters*, 27(13), 2009–2012. <https://doi.org/10.1029/1999GL011239>
- Hernández-Pajares, M., Juan, J. M., Sanz, J., & Solé, J. G. (1998). Global observation of the ionospheric electronic response to solar events using ground and LEO GPS data. *Journal of Geophysical Research: Space Physics*, 103(A9), 20789–20796. <https://doi.org/10.1029/98JA01272>
- Hernández-Pajares, M., Lyu, H., Aragón-Ángel, A., Monte-Moreno, E., Liu, J., An, J., & Jiang, H. (2020). Polar electron content from GPS data-based global ionospheric maps: Assessment, case studies, and Climatology. *Journal of Geophysical Research: Space Physics*, 125(6), e2019JA027677. <https://doi.org/10.1029/2019JA027677>
- Hernández-Pajares, M., Lyu, H., Garcia-Fernandez, M., & Orus-Perez, R. (2020). A new way of improving global ionospheric maps by ionospheric tomography: Consistent combination of multi-GNSS and multi-space geodetic dual-frequency measurements gathered from vessel-, LEO-and ground-based receivers. *Journal of Geodesy*, 94(8). <https://doi.org/10.1007/s00190-020-01397-1>

## Acknowledgments

Q. Liu is grateful for the financial support of the China Scholarship Council. This research has been done under the partial support of the ESA and European Commission (EC) funded eMONITOR/MoNEWIC (H2020-ESA-037) project and the EC funded PITH-IA-NRF (H2020-INFRAIA-2018-2020 101007599) project.

- Hernández-Pajares, M., Zornoza, J. M. J., Subirana, J. S., Farnworth, R., & Soley, S. (2005). EGNOS test bed ionospheric corrections under the October and November 2003 storms. *IEEE Transactions on Geoscience and Remote Sensing*, 43(10), 2283–2293. <https://doi.org/10.1109/TGRS.2005.855625>
- Jakowski, N., Béniguel, Y., De Franceschi, G., Pajares, M. H., Jacobsen, K. S., Stanislawski, I., et al. (2012). Monitoring, tracking and forecasting ionospheric perturbations using GNSS techniques. *Journal of Space Weather and Space Climate*, 2, A22. <https://doi.org/10.1051/swsc/2012022>
- Jakowski, N., Borries, C., & Wilken, V. (2012). Introducing a disturbance ionosphere index. *Radio Science*, 47(4). <https://doi.org/10.1029/2011RS004939>
- Jakowski, N., & Hoque, M. M. (2019). Estimation of spatial gradients and temporal variations of the total electron content using ground-based GNSS measurements. *Space Weather*, 17(2), 339–356. <https://doi.org/10.1029/2018SW002119>
- Jakowski, N., Stankov, S., Schlueter, S., & Klaehn, D. (2006). On developing a new ionospheric perturbation index for space weather operations. *Advances in Space Research*, 38(11), 2596–2600. <https://doi.org/10.1016/j.asr.2005.07.043>
- Lee, J., Pullen, S., Datta-Barua, S., & Enge, P. (2006). Assessment of Nominal Ionosphere Spatial Decorrelation for LAAS. *Proceedings of IEEE/ION PLANS 2006*, 506–514.
- Li, Z., Wang, N., Hernández-Pajares, M., Yuan, Y., Krankowski, A., Liu, A., et al. (2020). IGS real-time service for global ionospheric total electron content modeling. *Journal of Geodesy*, 94(3). <https://doi.org/10.1007/s00190-020-01360-0>
- Li, Z., Yuan, Y., Wang, N., Hernandez-Pajares, M., & Huo, X. (2015). SHPTS: Towards a new method for generating precise global ionospheric TEC map based on spherical harmonic and generalized trigonometric series functions. *Journal of Geodesy*, 89(4), 331–345. <https://doi.org/10.1007/s00190-014-0778-9>
- Liu, Q., Hernández-Pajares, M., Lyu, H., & Goss, A. (2021). Influence of temporal resolution on the performance of global ionospheric maps. *Journal of Geodesy*, 95(3). <https://doi.org/10.1007/s00190-021-01483-y>
- Liu, Q., Hernández-Pajares, M., Lyu, H., Nishioka, M., Yang, H., Monte-Moreno, E., et al. (n.d.). Ionospheric storm scale index based on high time resolution UPC-IonSAT global ionospheric maps (IsUG). *Space Weather*, 19, e2021SW002853. <https://doi.org/10.1029/2021SW002853>
- Liu, Q., Hernández-Pajares, M., Yang, H., Monte-Moreno, E., Roma-Dollase, D., García-Rigo, A., et al. (2021). The cooperative IGS RT-GIMs: A reliable estimation of the global ionospheric electron content distribution in real time. *Earth System Science Data*, 13(9), 4567–4582. <https://doi.org/10.5194/essd-13-4567-2021>
- Maruyama, T., Ma, G., & Tsugawa, T. (2013). Storm-induced plasma stream in the low-latitude to midlatitude ionosphere. *Journal of Geophysical Research: Space Physics*, 118(9), 5931–5941. <https://doi.org/10.1002/jgra.50541>
- Matzka, J., Stolle, C., Yamazaki, Y., Bronkalla, O., & Morschhauser, A. (2021). The geomagnetic Kp index and derived indices of geomagnetic activity. *Space Weather*, 19(5), e2020SW002641. <https://doi.org/10.1029/2020SW002641>
- Monaldo, F. (1991). Ionospheric variability and the measurement of ocean mesoscale circulation with a spaceborne radar altimeter. *Journal of Geophysical Research*, 96(C3), 4925–4937. <https://doi.org/10.1029/90jc02486>
- Nishioka, M., Tsugawa, T., Jin, H., & Ishii, M. (2017). A new ionospheric storm scale based on TEC and  $f_oF_2$  statistics. *Space Weather*, 15(1), 228–239. <https://doi.org/10.1002/2016sw001536>
- Noll, C. E. (2010). The crustal dynamics data information system: A resource to support scientific analysis using space geodesy. *Advances in Space Research*, 45(12), 1421–1440. <https://doi.org/10.1016/j.asr.2010.01.018>
- Orús, R., Hernández-Pajares, M., Juan, J., & Sanz, J. (2005). Improvement of global ionospheric VTEC maps by using kriging interpolation technique. *Journal of Atmospheric and Solar-Terrestrial Physics*, 67(16), 1598–1609. <https://doi.org/10.1016/j.jastp.2005.07.017>
- Park, J., Noja, M., Stolle, C., & Lühr, H. (2013). The Ionospheric Bubble Index deduced from magnetic field and plasma observations onboard Swarm. *Earth, Planets and Space*, 65(11), 1333–1344. <https://doi.org/10.5047/eps.2013.08.005>
- Pi, X., Mannucci, A., Lindqwister, U., & Ho, C. (1997). Monitoring of global ionospheric irregularities using the worldwide GPS network. *Geophysical Research Letters*, 24(18), 2283–2286. <https://doi.org/10.1029/97GL02273>
- Rino, C., Cousins, M., & Klobuchar, J. (1981). Amplitude and phase scintillation measurements using the Global Positioning System. In *Symposium on the effect of the ionosphere on radiowave systems*.
- Roma-Dollase, D., Hernández-Pajares, M., Krankowski, A., Kotulak, K., Ghoddousi-Fard, R., Yuan, Y., et al. (2018). Consistency of seven different GNSS global ionospheric mapping techniques during one solar cycle. *Journal of Geodesy*, 92(6), 691–706. <https://doi.org/10.1007/s00190-017-1088-9>
- Schaer, S., Beutler, G., Mervart, L., Rothacher, M., & Wild, U. (1995). Global and regional ionosphere models using the GPS double difference phase observable. In *Proceedings of the IGS workshop "special topics and new directions"*.
- Schaer, S., Gurtner, W., & Feltens, J. (1998). IONEX: The ionosphere map exchange format version 1. In *Proceedings of the IGS AC workshop* (Vol. 9).
- Vlasov, M., Kelley, M. C., & Kil, H. (2003). Analysis of ground-based and satellite observations of F-region behavior during the great magnetic storm of July 15, 2000. *Journal of Atmospheric and Solar-Terrestrial Physics*, 65(11–13), 1223–1234. <https://doi.org/10.1016/j.jastp.2003.08.012>
- Webb, D. F., & Allen, J. H. (2004). Spacecraft and ground anomalies related to the October–November 2003 solar activity. *Space Weather*, 2(3). <https://doi.org/10.1029/2004sw000075>
- Wilken, V., Kriegel, M., Jakowski, N., & Berdermann, J. (2018). An ionospheric index suitable for estimating the degree of ionospheric perturbations. *Journal of Space Weather and Space Climate*, 8, A19. <https://doi.org/10.1051/swsc/2018008>
- World Data Center for Geomagnetism, K., Nose, M., Iyemori, T., Sugiura, M., & Kamei, T. (2015). Geomagnetic Dst index. <https://doi.org/10.17593/14515-74000>
- Yang, H., Monte-Moreno, E., Hernández-Pajares, M., & Roma-Dollase, D. (2021). Real-time interpolation of global ionospheric maps by means of sparse representation. *Journal of Geodesy*, 95(6). <https://doi.org/10.1007/s00190-021-01525-5>
- Zhang, H., Xu, P., Han, W., Ge, M., & Shi, C. (2013). Eliminating negative VTEC in global ionosphere maps using inequality-constrained least squares. *Advances in Space Research*, 51(6), 988–1000. <https://doi.org/10.1016/j.asr.2012.06.026>
- Zhang, Q., & Zhao, Q. (2019). Analysis of the data processing strategies of spherical harmonic expansion model on global ionosphere mapping for moderate solar activity. *Advances in Space Research*, 63(3), 1214–1226. <https://doi.org/10.1016/j.asr.2018.10.031>













## RESEARCH ARTICLE

10.1029/2021SW002853

# Ionospheric Storm Scale Index Based on High Time Resolution UPC-IonSAT Global Ionospheric Maps (IsUG)

### Key Points:

- The new ionospheric storm scale, IsUG, is presented
- The IsUG is based on the high resolution and rapid UPC-IonSAT Global Ionosphere Maps (UQRG)
- Statistical analysis is carried out on a global scale from 1997 to 2014 comparing well with the available raw GNSS data based I-scale index

Qi Liu<sup>1</sup> , Manuel Hernández-Pajares<sup>1,2</sup> , Haixia Lyu<sup>3,1</sup> , Michi Nishioka<sup>4</sup> , Heng Yang<sup>5,1</sup> , Enric Monte-Moreno<sup>6</sup> , Tamara Gulyaeva<sup>7</sup> , Yannick Béniguel<sup>8</sup> , Volker Wilken<sup>9</sup>, Germán Olivares-Pulido<sup>1</sup> , and Raúl Orús-Pérez<sup>10</sup> 

<sup>1</sup>Universitat Politècnica de Catalunya (UPC-IonSAT), Barcelona, Spain, <sup>2</sup>Institut d'Estudis Espacials de Catalunya (IEEC), Barcelona, Spain, <sup>3</sup>GNSS Research Center, Wuhan University, China, <sup>4</sup>National Institute of Information and Communications Technology (NICT), Tokyo, Japan, <sup>5</sup>School of Electronic Information and Engineering, Yangtze Normal University, Chongqing, China, <sup>6</sup>Department of TSC, TALP, Universitat Politècnica de Catalunya, Barcelona, Spain, <sup>7</sup>IZMIRAN, Moscow, Russia, <sup>8</sup>Informatique, Electromagnétisme, Electronique, Analyse numérique (IEEA), Courbevoie, France, <sup>9</sup>German Aerospace Center (DLR), Neustrelitz, Germany, <sup>10</sup>Wave Interaction and Propagation Section (TEC-EFW) ESA ESTEC, Noordwijk, The Netherlands

### Supporting Information:

Supporting Information may be found in the online version of this article.

### Correspondence to:

M. Hernández-Pajares,  
manuel.hernandez@upc.edu

### Citation:

Liu, Q., Hernández-Pajares, M., Lyu, H., Nishioka, M., Yang, H., Monte-Moreno, E., et al. (2021). Ionospheric storm scale index based on high time resolution UPC-IonSAT global ionospheric maps (IsUG). *Space Weather*, 19, e2021SW002853. <https://doi.org/10.1029/2021SW002853>

Received 20 JUL 2021  
Accepted 10 OCT 2021

**Abstract** The ionospheric storms have adverse effects on the radio communications, satellite communications and also the Global Navigation Satellite Systems (GNSS) application. A new Ionospheric storm Scale from Universitat Politècnica de Catalunya (UPC) Global Ionosphere Map (GIM), IsUG, is introduced for characterizing the ionospheric state on a global scale. The IsUG is based on the Vertical Total Electron Content (VTEC) derived from the continuously computed UPC Quarter-of-an-hour time resolution Rapid GIM (UQRG), taking as reference the ones during the period 1997 to 2014. It is similar to the I-scale index previously introduced, although it was over Japan and based on raw GNSS data. The dependence of the VTEC on season, local time and geographical location at each grid point of UQRG is removed by normalizing (i.e., by subtracting the mean and dividing by the corresponding standard deviation) the percentage deviation of hourly median VTEC. After validating IsUG versus I-scale, the IsUG distribution is presented and analyzed at global scale during a severe geomagnetic storm from 7 to 10 November 2004 as an example of the potentialities of the new index. The results suggest that the IsUG global map has a great potential for the scientific study of ionospheric storms from a global perspective and also for space weather warning considering the accuracy of the recently developed real-time GIMs.

**Plain Language Summary** The upper part of the atmosphere, the ionosphere, affects the Global Navigation Satellite Systems (GNSS) signals crossing it. Thanks to this effect, and to the worldwide coverage of GNSS receivers, it is possible to estimate the spatial and temporal distribution of free electrons at global scale (the so called Global Ionosphere Maps, GIMs). In this work we present a new application of the GIMs, as a simple and worldwide way of providing the scale of ionospheric storm (IsUG), in agreement with a previous definition based on raw localized GNSS data, and allowing its computation in real-time.

## 1. Introduction

Driven by the high energy inputs resulting from geomagnetic storms, the ionospheric storms contain varying electron density and have significant impacts on the society in general and on the space environment in particular, including high ionospheric correction error for trans-ionospheric radio signals, blackouts of High Frequency (HF) communication systems and disruption of Ultra High Frequency (UHF) satellite communications (Buonsanto, 1999). The evolution of ionospheric storms can be divided into positive phase (when the electron density increases) and negative phase (when the electron density decreases; Fagundes et al., 2016). It is important to identify the ionospheric conditions for the space weather warnings to mitigate the influence of ionospheric storms.

In 1960, a monthly ionospheric index was introduced in terms of a monthly mean of the ionospheric critical frequency  $f_0F2$  measured from several stations, reflecting the average conditions of the ionosphere (Minnis & Bazzard, 1960). And the improved ionospheric index MF2 was proposed to increase the accuracy of monthly median  $f_0F2$  estimation and long-term prediction (Mikhailov & Mikhailov, 1995; Perrone & De

© 2021. The Authors.

This is an open access article under the terms of the [Creative Commons Attribution-NonCommercial-NoDerivs License](https://creativecommons.org/licenses/by-nc-nd/4.0/), which permits use and distribution in any medium, provided the original work is properly cited, the use is non-commercial and no modifications or adaptations are made.

Franceschi, 1998). To represent the real-time ionospheric conditions, the ionospheric activity indices (AI) were calculated by the comparison between real-time hourly  $f_0F2$  and median  $f_0F2$  of the same local time for the past 30 days (Bremer et al., 2006). Afterward the degree of ionospheric disturbance, W-index, was introduced in Gulyaeva and Stanislawska (2008) in terms of the logarithm of hourly Total Electron Content (TEC) referred to the median hourly TEC for the past 27 days. In addition, the ionosphere variability index  $V_o$  was obtained by moving TEC median in the preceding 15 days with variance bounds at grid points of GIM (Gulyaeva & Mannucci, 2020). In order to remove the dependence of the ionospheric state on season, local time, and geographical position, the ionospheric storm scale (I-scale) was proposed by Nishioka et al. (2017). However, the presented I-scale was based on the hourly median TEC extracted from GNSS raw observations of the Japanese regional station network only.

The Ionosphere Working Group (Iono-WG) was created in the frame of the International GNSS Service (IGS) in 1998. One of the main goals of Iono-WG was to derive GIMs with different techniques from raw GNSS observations in IONosphere map EXchange (IONEX) format by the different analysis centers, assessing and generating a combined GIM (Feltens & Schaer, 1998; Feltens, 2007; Mannucci et al., 1998; Hernández-Pajares et al., 1998, 1999, 2009; Schaer et al., 1996, 1998). The IGS GIMs provide global VTEC at grid points with the common spatial resolution of  $2.5^\circ \times 5^\circ$  in latitude and longitude (Ghoddousi-Fard, 2014; Li et al., 2015; Zhang et al., 2013). The temporal resolution of IGS GIMs ranges from 15 min to 2 h (Liu, Hernández-Pajares, Lyu, et al., 2021). Among the GIMs from different IGS Ionospheric Associate Analysis Centers (IAACs), the UQRG from UPC describes the estimated VTEC from slant GNSS observation as a tomographic two-layer voxel-based model in a sun-fixed geomagnetic reference frame and estimates the VTEC of each voxel every 15 min by Kriging interpolation technique on a global scale (Hernández-Pajares et al., 1998, 1999, 2000; Orús et al., 2005). The UQRG has been proven to be one of the most accurate GIMs (Hernández-Pajares et al., 2017; Roma-Dollase et al., 2018). In particular, UQRG is able to represent realistic VTEC structures in the challenging polar regions where few GNSS stations and observations are available and the VTEC estimation is challenging (Hernández-Pajares et al., 2020).

The good performance and high temporal resolution of UQRG allow us to introduce a new ionospheric storm scale based on the definition of I-scale and historical UQRG from 1997 to 2014. The new ionospheric storm scale is able to provide in a fast and straightforward way (based on a single daily GIM file in IONEX format instead of hundreds of raw GNSS data files) for generating a realistic global map of the ionospheric storm disturbance level, which is dependent-free on season, local time, and geographic location.

## 2. Data and Methodology for IsUG

The hourly median VTEC at each grid point was extracted from historical UQRG with a 15-min resolution (during the period 1997–2014). Since the spatial resolution of UQRG is  $2.5^\circ \times 5^\circ$  in latitude and longitude, the hourly median VTEC is derived at 5,112 grid points on a global scale. Hereafter the derived hourly VTEC is denoted as  $G_{TEC}$ . The percentage deviation of VTEC was computed to describe the current ionospheric state as indicated in previous studies (Bremer et al., 2006; Nishioka et al., 2017). The formula can be seen in Equation 1.

$$P_{TEC} = \frac{100 \times (G_{TEC} - R_{TEC})}{R_{TEC}} \quad (1)$$

where  $P_{TEC}$  is the percentage deviation of VTEC.  $G_{TEC}$  is the hourly median VTEC derived at grid points of GIM. The hourly median VTEC is the median of the five VTEC values during 1-h interval, under the GIM VTEC temporal resolution of 15 min. The hourly median VTEC is calculated every hour (for example, 0, 1, 2 UT). The median VTEC is adopted since the median value would have lower variability than a mean value. The hourly median VTEC is also chosen to mitigate the effect of extremely large or small estimated VTEC values. The  $R_{TEC}$  is the reference median value derived from the  $G_{TEC}$  at the same local time and geographic location in the past 27 days. In this way the influence of this significant period of VTEC variability (see for example Figure 22 in Hernández-Pajares et al., 2009) is removed. The 27 days window is in agreement with the solar rotation period, which has a significant impact on the VTEC variation of ionosphere (Bremer et al., 2006; Schmölter et al., 2021). Both the 27 days variation of solar radiation and the 27 days variation of geomagnetic activity caused by the solar wind and interplanetary magnetic field, have effects

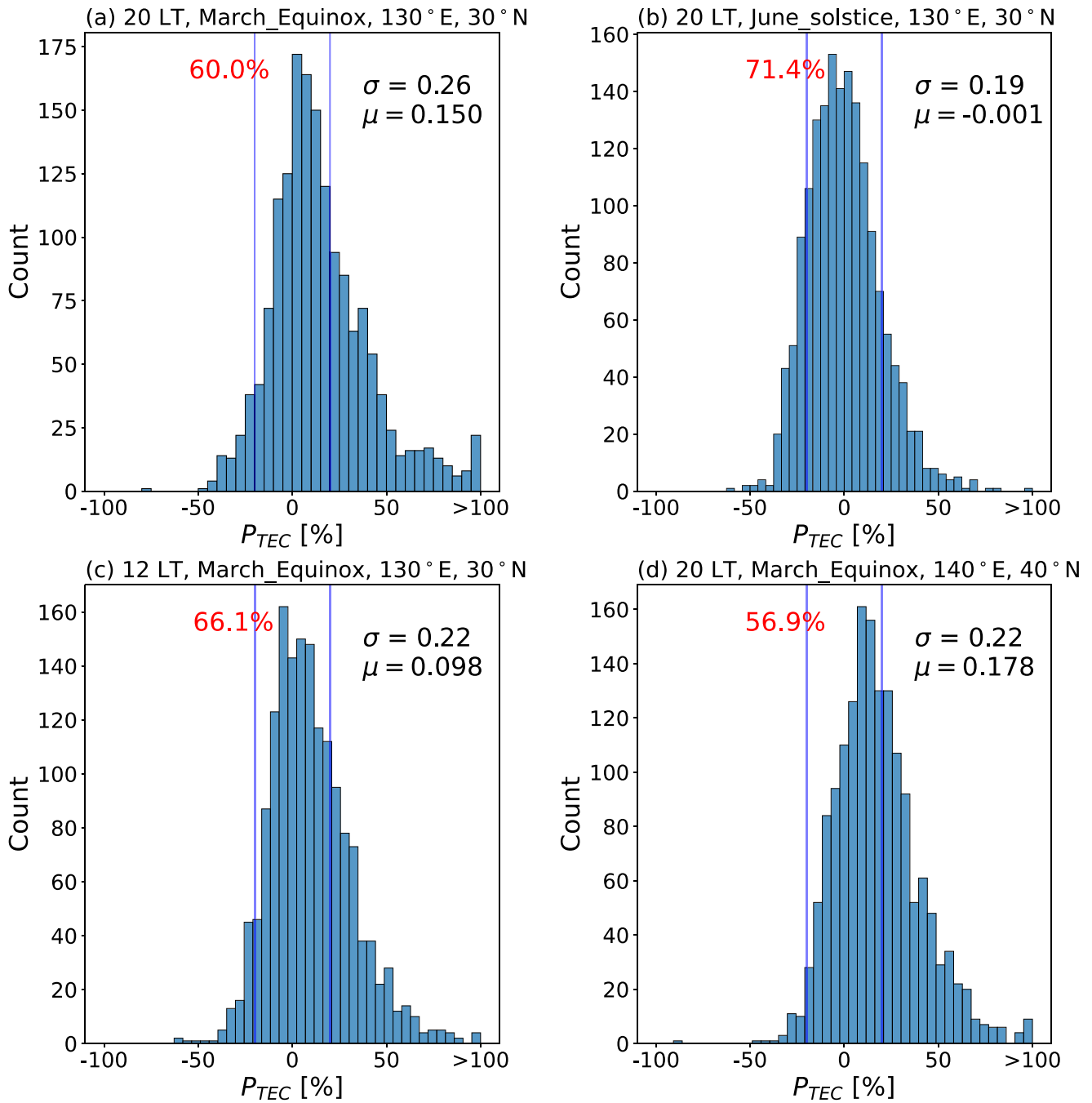


**Figure 1.** The distribution of  $P_{TEC}$  from 1997 to 2014 (the number in red color indicates the relative amount of the absolute percentage values  $|P_{TEC}|$  below 20%). (a)  $P_{TEC}$  of (130°E, 30°N) during 3 months around March Equinox at 20 Local Time (LT) (b)  $P_{TEC}$  of (130°E, 30°N) during 3 months around June Solstice at 20 Local Time (LT) (c)  $P_{TEC}$  of (130°E, 30°N) during 3 months around March Equinox at 12 LT (d)  $P_{TEC}$  of (140°E, 40°N) during 3 months around March Equinox at 20 LT.

on ionospheric VTEC (Ma et al., 2012; Schreiber, 1998). The window size smaller and larger than 27 days is more affected by the daily variations and the seasonal variations (Nishioka et al., 2017).

With the purpose of characterizing and comparing the distribution of UQRG-GIM derived  $P_{TEC}$  at specific regions previously characterized by I-scale (Nishioka et al., 2017), the grid points of (130°E, 30°N) and (140°E, 40°N) were chosen in longitude and latitude, coinciding with the corresponding values in Nishioka



**Table 1**  
Comparison of  $P_{TEC}$  Distribution Parameters During 1997–2014 Between the Values Derived From UQRG (Input for IsUG Index) and the Values Derived in Nishioka et al. (2017) as Input to I-Scale

Season	LT	Long.	Lat.	$P_{TEC}$ (UQRG-GIM)			$P_{TEC}$ (raw-GNSS-data)		
				$\sigma$	$\mu$	per. 20%	$\sigma$	$\mu$	per. 20%
March Equi.	20 h	130°E	30°N	0.28	0.150	60.0	0.33	0.19	54.3
June Equi.	20 h	130°E	30°N	0.19	−0.001	71.4	0.20	−0.02	69.7
March Equi.	12 h	130°E	30°N	0.22	0.098	66.1	0.26	0.08	62.1
March Equi.	20 h	140°E	40°N	0.23	0.178	56.9	0.27	0.22	50.2

et al. (2017) and the same time period (years 1997–2014). It should be noted out that the grid point of (130°E, 30°N) is within the region of 29° latitudinal band, while the grid point of (140°E, 40°N) is within the region of 41° latitudinal band as defined in Nishioka et al. (2017). In addition, the mean value  $\mu$  and standard deviation  $\sigma$  of  $P_{TEC}$  are divided by 100 (i.e., not in %) in all the figures and tables, in order to compare with the figures and tables of Nishioka et al. (2017).

As it can be seen in Figure 1, the histograms are dissimilar at different local time, season and geographical locations. Figure 1a shows the histogram of  $P_{TEC}$ , where 60% of absolute percentage values  $|P_{TEC}|$  have a value lower than 20% and can be regarded as undisturbed at grid point [130°E, 30°N]. 71.4% of absolute percentage values  $|P_{TEC}|$  are lower than 20% in Figure 1b. In addition, the standard deviation  $\sigma$  of  $P_{TEC}$  is 0.28 and the mean value  $\mu$  of  $P_{TEC}$  is 0.19 in Figure 1a, while the  $\sigma$  and  $\mu$  of Figure 1b are 0.19 and −0.001, respectively. The difference between Figures 1a and 1b is the season: the season is March Equinox in Figure 1a, while the season is June Solstice in Figure 1b. Consequently, the  $P_{TEC}$  is affected by the season variation. In addition, the difference between Figures 1a and 1c indicates the local time dependence of  $P_{TEC}$ . In Figure 1d, 56.9% of absolute percentage values  $|P_{TEC}|$  are smaller than 20% at grid point [140°E, 40°N]. These results are similar to the corresponding input  $P_{TEC}$  values for I-scale shown in Figure 1 of Nishioka et al. (2017), as it is summarized in Table 1.

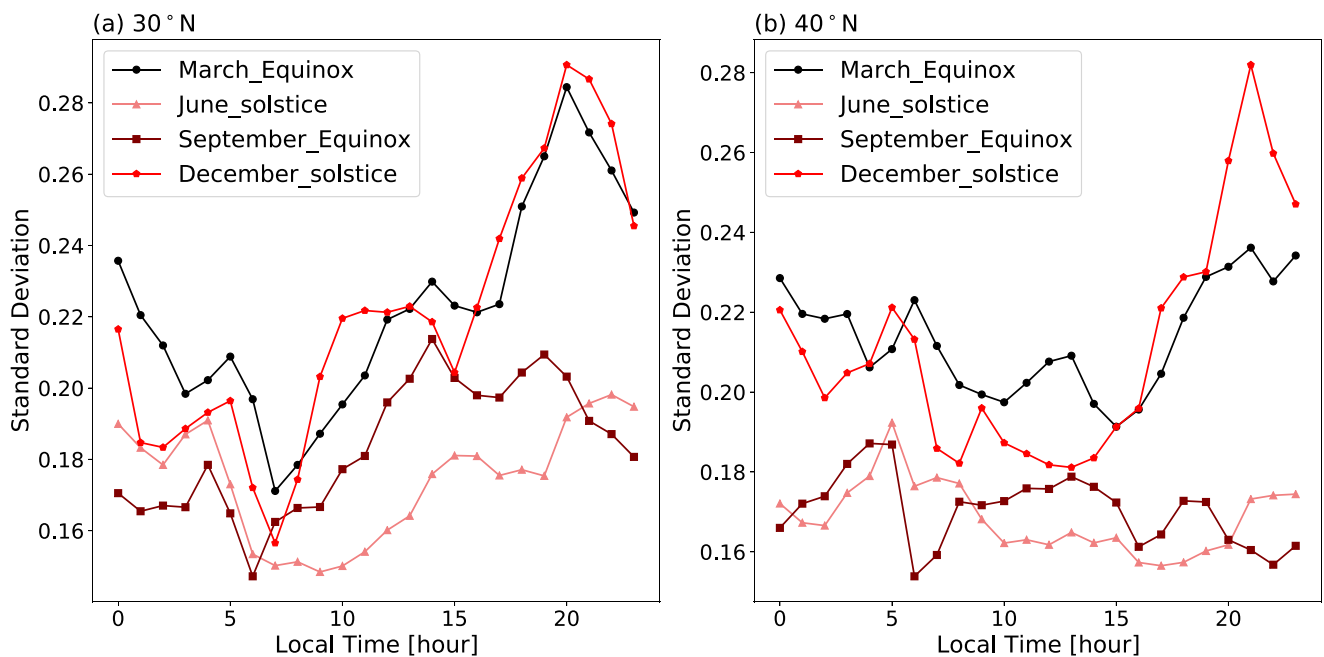


**Figure 2.** The variation of standard deviation at different seasons. (a) Standard deviation of (140°E, 40°N) during the period from 1997 to 2014. (b) Standard deviation of (130°E, 30°N) during the period from 1997 to 2014.

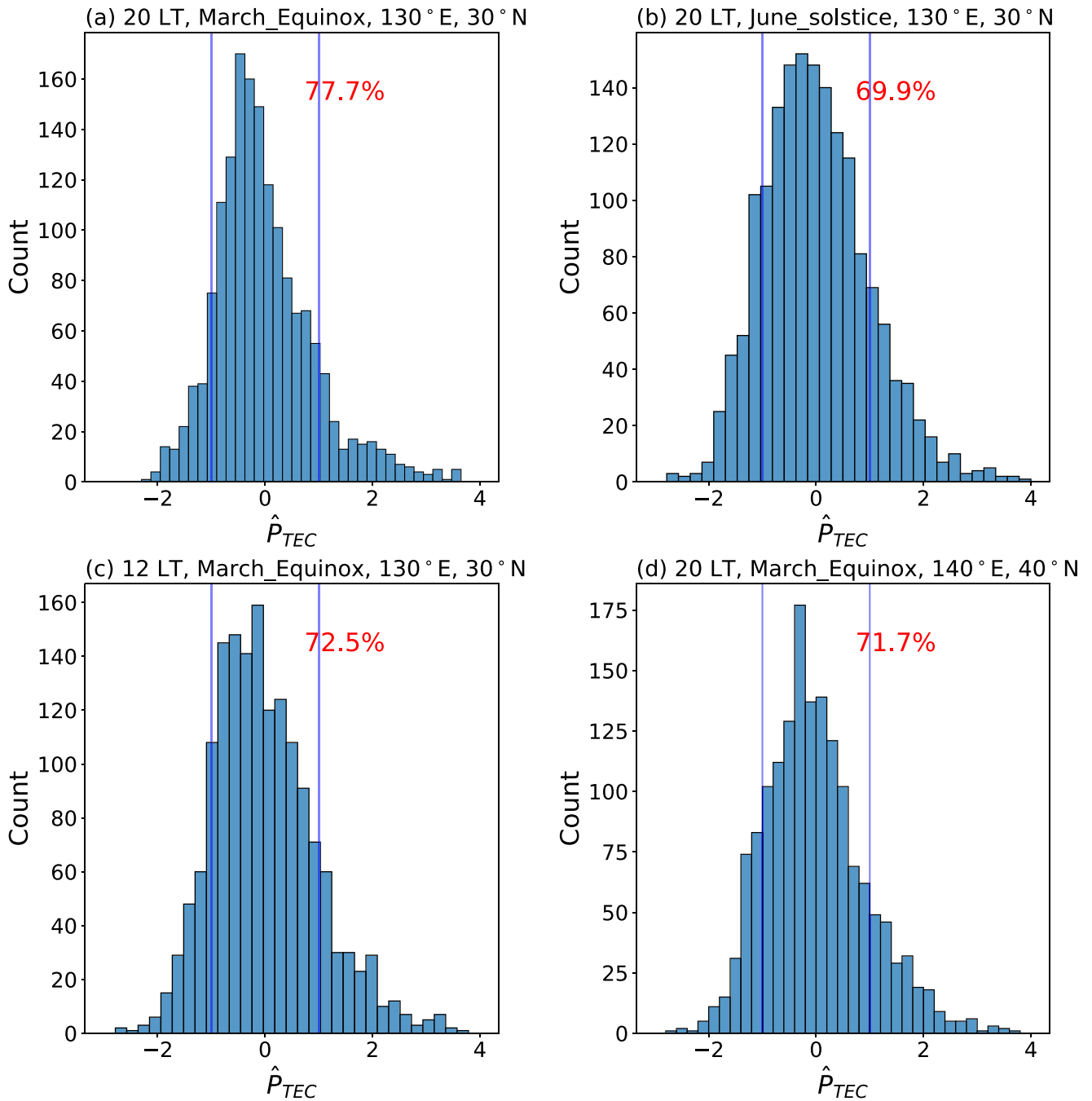


**Figure 3.** The distribution of  $\hat{P}_{TEC}$  from 1997 to 2014 (the number in red color indicates the rate of count when the absolute percentage values  $|\hat{P}_{TEC}|$  are lower than 20%). (a)  $\hat{P}_{TEC}$  of (130°E, 30°N) during 3 months around March Equinox at 20 Local Time (LT) (b)  $\hat{P}_{TEC}$  of (130°E, 30°N) during 3 months around June Solstice at 20 LT (c)  $\hat{P}_{TEC}$  of (130°E, 30°N) during 3 months around March Equinox at 12 LT (d)  $\hat{P}_{TEC}$  of (140°E, 40°N) during 3 months around March Equinox at 20 LT.

In Figure 2a and 2b, it is shown that the standard deviation values of March Equinox and December Solstice are typically larger than the standard deviation of September Equinox and June Solstice. While the standard deviation reaches higher value around 5 and 20 local hour in Figures 2a and 2b, the standard deviation of grid point (140°E, 40°N) tends to be smoother than the grid point (130°E, 30°N) during the daytime. The LT evolution of the  $P_{TEC}$ (UQRG-GIM) standard deviation is in general similar but slightly lower when it is

**Table 2**

Comparison of the Percentiles for  $|\hat{P}_{TEC}| \leq 1$  During 1997–2014 Between the Values Derived From UQRG (Input for IsUG Index) and the Values Derived in Nishioka et al. (2017) as Input to I-Scale

Season	LT	Long.	Lat.	$\hat{P}_{TEC}$ (UQRG-GIM)	$\hat{P}_{TEC}$ (raw-GNSS-data)
				(this work)	(Nishioka et al., 2017)
				perc. $ \hat{P}_{TEC}  \leq 1$	perc. $ \hat{P}_{TEC}  \leq 1$
March Equi.	20 h	130°E	30°N	77.7	77.5
June Equi.	20 h	130°E	30°N	69.7	72.9
March Equi.	12 h	130°E	30°N	72.5	72.6
March Equi.	20 h	140°E	40°N	71.7	72.3

compared with the corresponding results, shown in Figure 2 of Nishioka et al. (2017), but obtained from the raw-GNSS data. This is in agreement with the fact that the VTEC values provided under the GIM resolution can be smoother than the ones provided directly by the raw GNSS data.

The normalized  $P_{TEC}$  as Equation 2 is introduced to remove the dependence of  $P_{TEC}$  on season, local time and geographical location as shown in Figures 1 and 2. It should be noted that the normalized  $P_{TEC}$  is calculated at each grid point with corresponding mean value and standard deviation from 1997 to 2014.

$$\hat{P}_{TEC} = \frac{P_{TEC} - \mu}{\sigma} \quad (2)$$

where the  $\mu$  and  $\sigma$  are the mean value and standard deviation derived from Equation 1 and shown in Figure 2. The mean value  $\mu$  and standard deviation  $\sigma$  of  $P_{TEC}$  at each grid point are calculated every hour (in local time) during each given season.

After the normalization of  $P_{TEC}$ , 69.9% – 77.7% of absolute percentage values  $|\hat{P}_{TEC}|$  are smaller than 1 in Figure 3, implying the minor difference among different season, local time, geographical location when  $|\hat{P}_{TEC}| < 1$ , also in agreement with the corresponding  $\hat{P}_{TEC}$  input for I-scale shown in Figure 3 of Nishioka et al. (2017). The summary of both distributions of  $\hat{P}_{TEC}$  can be seen in Table 2.

As shown in Table 3, the definition of IsUG can be seen in the first, second and third columns, for severe, strong, moderate (positive and negative) among quiet states. And the occurrence probability of IsUG at global scale is given in the fourth column. The probability of a quiet ionospheric state is 73.96%, which is similar to the I-scale results at 29°N over Japan (Table 1 in Nishioka et al., 2017). And the probabilities of either positive and negative moderate, strong, severe ionospheric storms are around 10%, 1%, 0.1%.

### 3. Results and Analysis

In this section, the results of IsUG based on UQRG from 1997 to 2014 are presented in detail and analyzed.

#### 3.1. The Statistics of IsUG During a Severe Geomagnetic Storm

The consistency between the IsUG and I-scale indices can be seen in detail during geomagnetic storms. Indeed, a severe geomagnetic storm happened from November 7 to 10, 2004, as reported in previous studies (e.g., Maruyama, 2006; Maruyama et al., 2013; Sori et al., 2019). As depicted in Figure 4, the observed VTEC at [130°E, 30°N],  $G_{TEC}$ , reaches ~100 TECU when the Dst value is –374 nT and the Kp value is 9– at 7 UT of November 8. And the highest  $\hat{P}_{TEC}$  (18.92) is obtained at 10 UT of November 8, as indicated as the left downward arrow in Figure 4b, taking into account the time dependence of the reference VTEC,  $R_{TEC}$ . As can be seen in Figure 5, the snapshots of UQRG VTEC,  $P_{TEC}$ , mean value  $\mu$

**Table 3**

The Definition and Occurrence Probability of IsUG Derived From UQRG During the Period 1997–2014

IsUG	Description	Definition	Probability on a global scale (%)
IP3	Severe positive storm	$5 < \hat{P}$	0.17
IP2	Strong positive storm	$3 < \hat{P} \leq 5$	0.72
IP1	Moderate positive storm	$1 < \hat{P} \leq 3$	12.43
I0	Quiet	$-1 < \hat{P} \leq 1$	73.96
IN1	Moderate negative storm	$-2 < \hat{P} \leq -1$	11.72
IN2	Strong negative storm	$-3 < \hat{P} \leq -2$	0.95
IN3	Severe negative storm	$\hat{P} < -3$	0.06

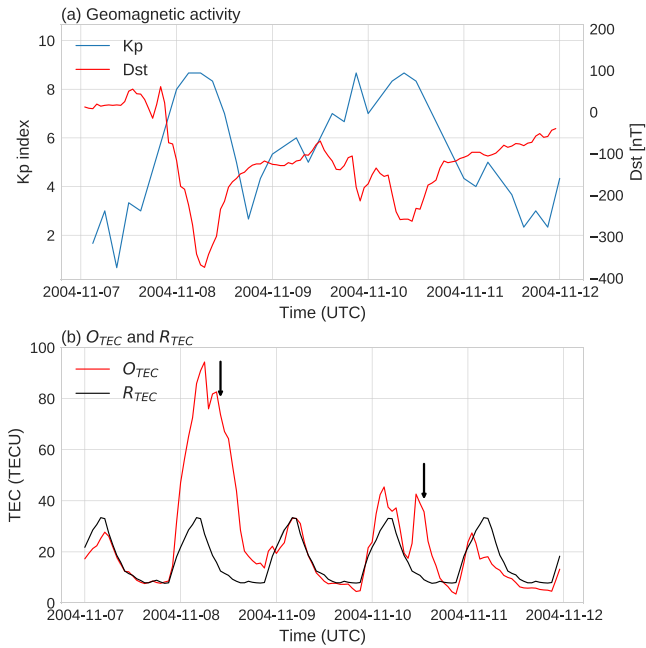


**Figure 4.** The evolution of  $G_{TEC}$ ,  $R_{TEC}$ , Kp and Dst at (130°E, 30°N) from November 7 to 10, 2004.

of  $P_{TEC}$  and standard deviation  $\sigma$  of  $P_{TEC}$  at each grid point are consistent with Figure 4 when the highest  $\hat{P}_{TEC}$  (18.92) at (130°E, 30°N) is obtained. The UQRG TEC reached a high value around grid point (130°E, 30°N). It should be noted that the high value of  $P_{TEC}$  around (155°E, 30°N) is caused by high  $G_{TEC}$  (33.4) and low  $R_{TEC}$  (2.7) around 23 LT during the nighttime.

The intense TEC enhancement that might be related to the storm-induced plasma stream, has been indicated by Maruyama et al. (2013). And right downward arrow in Figure 4b indicates the second peak  $\hat{P}_{TEC}$  at 13 UT of November 10. Finally we observe that the  $G_{TEC}$  and  $R_{TEC}$  values obtained from the UQRG GIM (bottom plot of Figure 4) are almost identical to the corresponding values obtained from raw GNSS measurements (central plot of Figure 4 in Nishioka et al., 2017).

### 3.2. Global Map of IsUG

With the  $\hat{P}_{TEC}$  calculated at each grid point of UQRG from 1997 to 2014, the global map of IsUG can be also obtained in a straightforward way (one advantage of IsUG vs. I-scale). The detailed animations of IsUG during one quiet and one disturbed period of 2004 are presented in the Supporting Information S1.

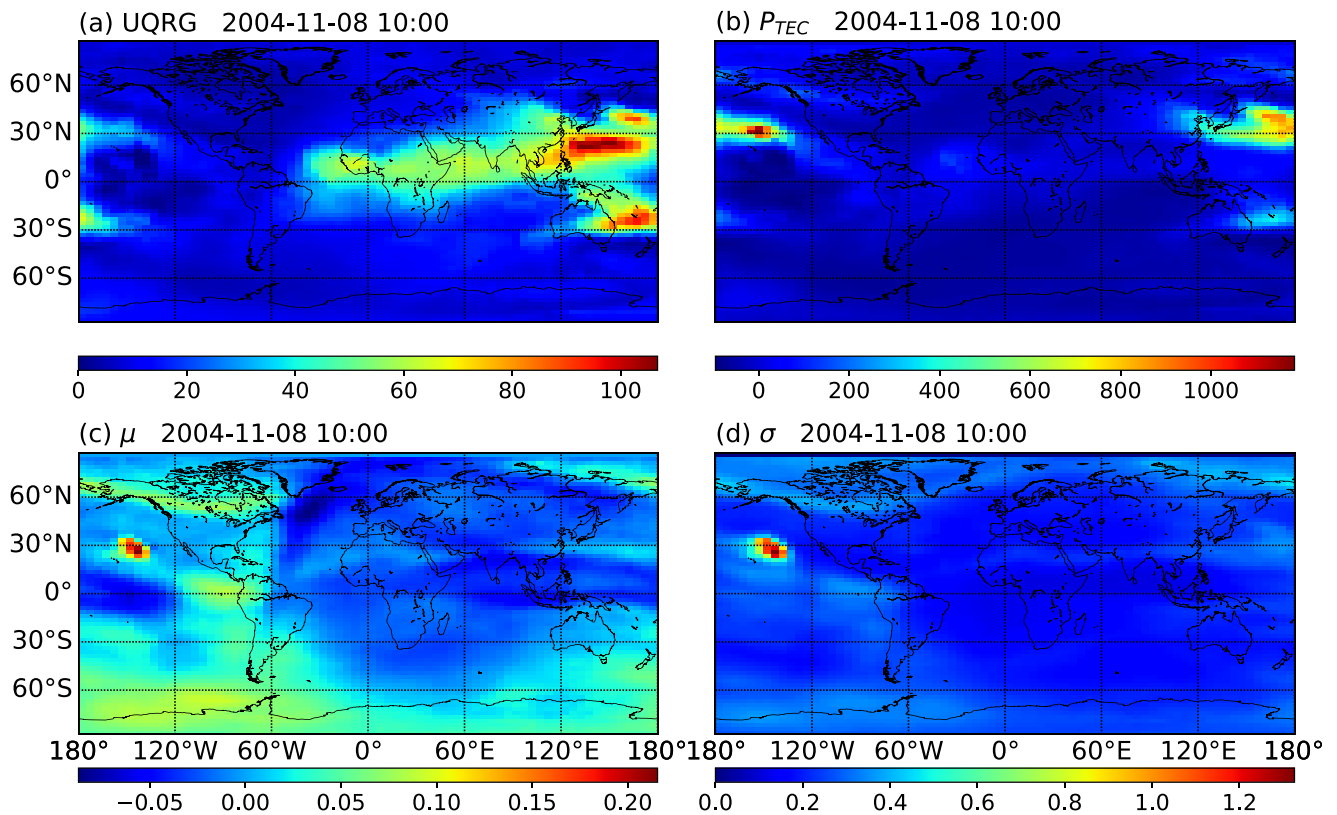


**Figure 5.** The snapshots of 10 UT on November 8, 2004. (a) The snapshot of UQRG VTEC (in TECU) at each grid point. (b) The snapshot of  $P_{TEC}$  value calculated by Equation 1 at each grid point. (c) The snapshot of mean value  $\mu$  of  $P_{TEC}$  at each grid point. (d) The snapshot of standard deviation  $\sigma$  of  $P_{TEC}$  at each grid point.

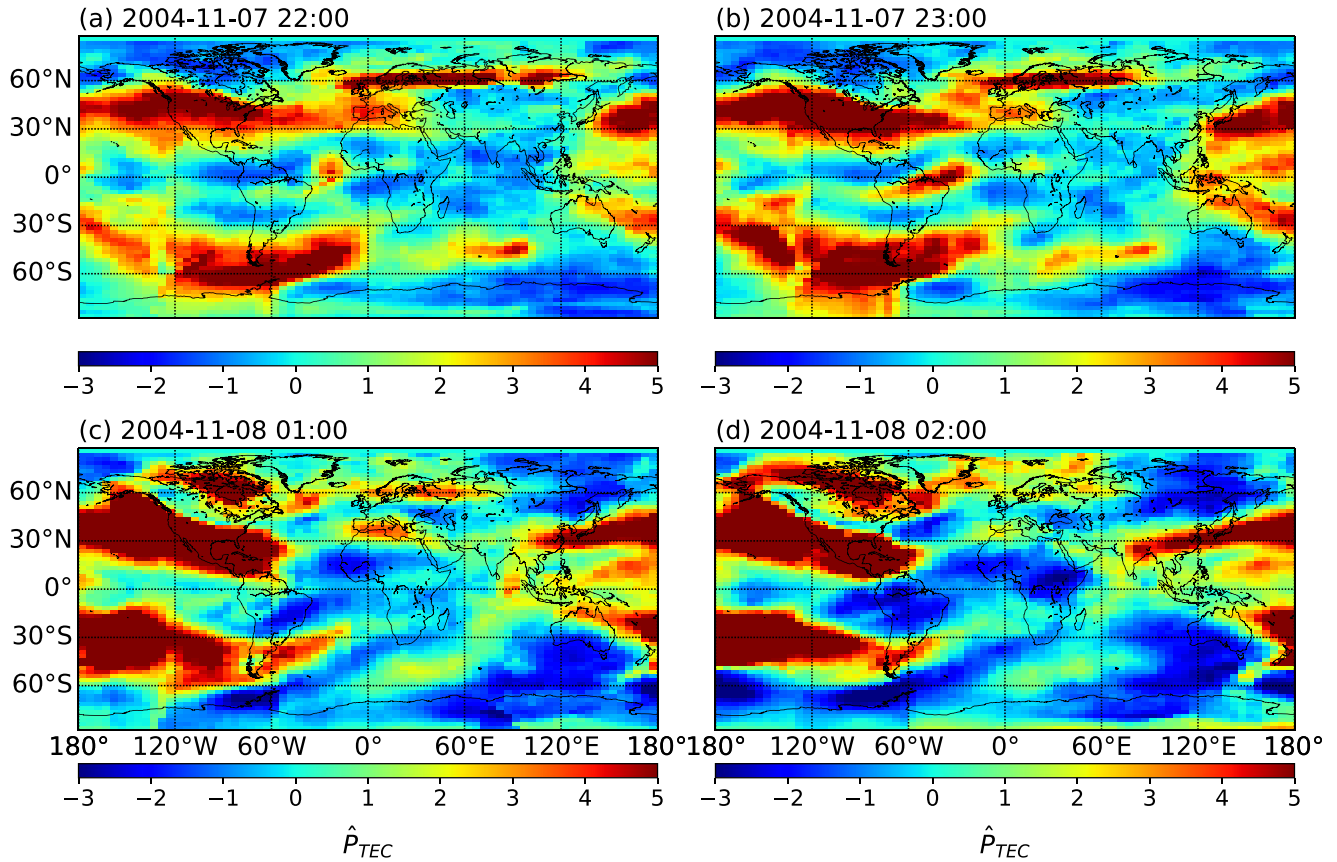


**Figure 6.** The IsUG global map of November 7, 8, 2004.

With a focus on specific regions, Figures 6 and 7 are selected during the severe geomagnetic storm from 7 to 10 November in 2004, which  $G_{TEC}$  (and  $R_{TEC}$ ) have been previously compared and discussed over Japan.

As presented in Figure 4 and previous studies (e.g., Maruyama, 2006; Maruyama et al., 2013; Nishioka et al., 2017), the strong TEC enhancement started from 23 UT of November 7 at Japan. The enhanced TEC is coincident with the movement of severe ionospheric positive storm ( $\hat{P}_{TEC} > 5$ ) at Japan in Figures 6a and 6b. In addition, noticeable TEC enhancement was found in a GNSS station ( $77.9^{\circ}S, 166.8^{\circ}E$ ) located at Antarctica (Sulaiman et al., 2007). And the TEC enhancement around the GNSS station can be also seen in the right bottom corner ( $77.9^{\circ}S, 166.8^{\circ}E$ ) of Figures 6c and 6d.

As shown in Figure 7a–7f, the  $\hat{P}_{TEC}$  started to increase since 14 UT and gradually expanded toward low latitude in Europe. The  $\hat{P}_{TEC}$  reached 2 (moderate positive storm) at 17 UT and 5 (severe positive storm) at 19 UT, which is consistent with the reported TEC variation in Sori et al. (2019).

#### 4. Conclusions

From the distribution of VTEC values during the period 1997–2014 extracted from UQRG GIMs computed on a daily basis by UPC-IonSAT for IGS, the IsUG storm index is derived, extending in a straightforward way the I-scale index on a global level. The IsUG global maps are initially compared with previous studies during the severe geomagnetic storm, with a focus on the regions of Japan, Antarctica, Europe. The variation of IsUG global maps is consistent with the results of previous studies, especially over Japan (Nishioka et al., 2017) and in the Antarctica region where few GNSS stations are available (Maruyama et al., 2013; Sori et al., 2019; Sulaiman et al., 2007). Since the IGS real-time GIMs (RT-GIMs) are availability and the accuracy of RT-GIMs is presently close to the accuracy of the UQRG GIMs, the generation of real-time

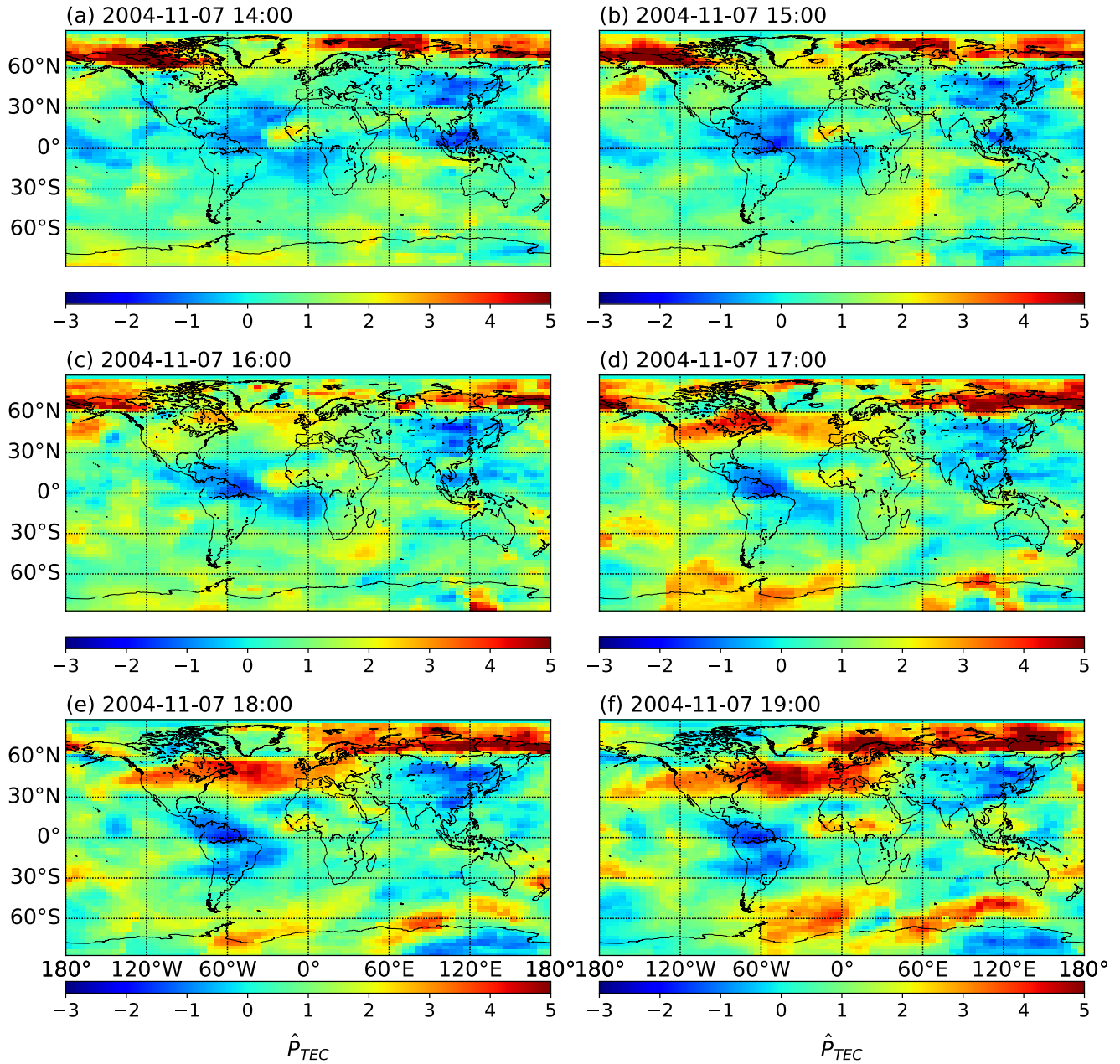


**Figure 7.** The IsUG global map from 14:00 to 19:00 UTC of November 7, 2004.

IsUG might be the next step (Liu, Hernández-Pajares, Yang, et al., 2021; Yang et al., 2021). In addition, the real-time ionospheric storm warning system based on real-time IsUG might be also available for space weather monitoring.

### Data Availability Statement

The UQRG data are openly accessible (<https://cdsis.nasa.gov/archive/gnss/products/ionex>) from Crustal Dynamics Data Information System (Noll, 2010). The Kp index is available ([ftp://ftp.gfz-potsdam.de/pub/home/obs/Kp\\_ap\\_Ap\\_SN\\_F107](ftp://ftp.gfz-potsdam.de/pub/home/obs/Kp_ap_Ap_SN_F107)) from GeoForschungsZentrum (Matzka et al., 2021) and Dst index is accessible (<http://wdc.kugi.kyoto-u.ac.jp/dstdir/>) from World Data Center for Geomagnetism, Kyoto (World Data Center for Geomagnetism et al., 2015).

## Acknowledgments

The first author is grateful for the financial support of the China Scholarship Council (CSC). This research has been done under the partial support of the European Space Agency and European Commission funded eMON-ITOR/MoNEWIC (H2020-ESA-037) project and the European Commission funded PITHIA-NRF (H2020-IN-FRAIA-2018-2020 101007599) project.

## References

- Bremer, J., Cander, Lj. R., Mielich, J., & Stamper, R. (2006). Derivation and test of ionospheric activity indices from real-time ionosonde observations in the European region. *Journal of Atmospheric and Solar-Terrestrial Physics*, 68(18), 2075–2090. <https://doi.org/10.1016/j.jastp.2006.07.003>
- Buonsanto, M. J. (1999). Ionospheric storms—A review. *Space Science Reviews*, 88, 563–601. <https://doi.org/10.1023/a:1005107532631>
- Fagundes, P. R., Cardoso, F., Fejer, B., Venkatesh, K., Ribeiro, B., & Pillat, V. (2016). Positive and negative GPS-TEC ionospheric storm effects during the extreme space weather event of March 2015 over the Brazilian sector. *Journal of Geophysical Research: Space Physics*, 121(6), 5613–5625. <https://doi.org/10.1002/2015ja022214>
- Feltens, J. (2007). Development of a new three-dimensional mathematical ionosphere model at European Space Agency/European Space Operations Centre. *Space Weather*, 5(12), S12002. <https://doi.org/10.1029/2006sw000294>
- Feltens, J., & Schaer, S. (1998). IGS products for the ionosphere. In *Proceedings of the 1998 IGS analysis*. Center Workshop Darmstadt.
- Ghoddousi-Fard, R. (2014). GPS ionospheric mapping at Natural Resources Canada. In *IGS workshop*.
- Gulyaeva, T., & Stanislawska, I. (2008). Derivation of a planetary ionospheric storm index. *Annales Geophysicae*, 26(9), 2645–2648. <https://doi.org/10.5194/angeo-26-2645-2008>
- Gulyaeva, T. L., & Mannucci, A. J. (2020). Echo of ring current storms in the ionosphere. *Journal of Atmospheric and Solar-Terrestrial Physics*, 205, 105300. <https://doi.org/10.1016/j.jastp.2020.105300>
- Hernández-Pajares, M., Juan, J., Sanz, J., & Solé, J. (1998). Global observation of the ionospheric electronic response to solar events using ground and LEO GPS data. *Journal of Geophysical Research*, 103(A9), 20789–20796. <https://doi.org/10.1029/98ja01272>
- Hernández-Pajares, M., Juan, J., & Sanz, J. (1999). New approaches in global ionospheric determination using ground GPS data. *Journal of Atmospheric and Solar-Terrestrial Physics*, 61(16), 1237–1247. [https://doi.org/10.1016/s1364-6826\(99\)00054-1](https://doi.org/10.1016/s1364-6826(99)00054-1)
- Hernández-Pajares, M., Juan, J., Sanz, J., & Colombo, O. L. (2000). Application of ionospheric tomography to real-time GPS carrier-phase ambiguities Resolution, at scales of 400–1000 km and with high geomagnetic activity. *Geophysical Research Letters*, 27(13), 2009–2012. <https://doi.org/10.1029/1999GL012339>
- Hernández-Pajares, M., Juan, J. M., Sanz, J., Orus, R., García-Rigo, A., Feltens, J., & Krankowski, A. (2009). The IGS VTEC maps: A reliable source of ionospheric information since 1998. *Journal of Geodesy*, 83, 263–275. <https://doi.org/10.1007/s00190-008-0266-1>
- Hernández-Pajares, M., Lyu, H., Aragón-Ángel, Á., Monte-Moreno, E., Liu, J., An, J., & Jiang, H. (2020). Polar electron content from GPS data-based global ionospheric maps: Assessment, case studies, and climatology. *Journal of Geophysical Research: Space Physics*, 125(6), e2019JA027677. <https://doi.org/10.1029/2019JA027677>
- Hernández-Pajares, M., Roma-Dollase, D., Krankowski, A., García-Rigo, A., & Orús-Pérez, R. (2017). Methodology and consistency of slant and vertical assessments for ionospheric electron content models. *Journal of Geodesy*, 91, 1405–1414. <https://doi.org/10.1007/s00190-017-1032-z>
- Li, Z., Yuan, Y., Wang, N., Hernandez-Pajares, M., & Huo, X. (2015). SHPTS: Towards a new method for generating precise global ionospheric TEC map based on spherical harmonic and generalized trigonometric series functions. *Journal of Geodesy*, 89(4), 331–345. <https://doi.org/10.1007/s00190-014-0778-9>
- Liu, Q., Hernández-Pajares, M., Lyu, H., & Goss, A. (2021). Influence of temporal resolution on the performance of global ionospheric maps. *Journal of Geodesy*, 95, 34. <https://doi.org/10.1007/s00190-021-01483-y>
- Liu, Q., Hernández-Pajares, M., Yang, H., Monte-Moreno, E., Roma-Dollase, D., García-Rigo, A., et al. (2021). The cooperative IGS RT-GIMs: A reliable estimation of the global ionospheric electron content distribution in real time. *Earth System Science Data*, 13(9), 4567–4582. <https://doi.org/10.5194/essd-13-4567-2021>
- Ma, R., Xu, J., Wang, W., & Lei, J. (2012). The effect of 27 day solar rotation on ionospheric F2 region peak densities (NmF2). *Journal of Geophysical Research*, 117(A3). <https://doi.org/10.1029/2011ja017190>
- Mannucci, A., Wilson, B., Yuan, D., Ho, C., Lindqwister, U., & Runge, T. (1998). A global mapping technique for GPS-derived ionospheric total electron content measurements. *Radio Science*, 33(3), 565–582. <https://doi.org/10.1029/97rs02707>
- Maruyama, T. (2006). Extreme enhancement in total electron content after sunset on 8 November 2004 and its connection with storm enhanced density. *Geophysical Research Letters*, 33(20). <https://doi.org/10.1029/2006gl027367>
- Maruyama, T., Ma, G., & Tsugawa, T. (2013). Storm-induced plasma stream in the low-latitude to midlatitude ionosphere. *Journal of Geophysical Research: Space Physics*, 118(9), 5931–5941. <https://doi.org/10.1002/jgra.50541>
- Matzka, J., Stolle, C., Yamazaki, Y., Bronkalla, O., & Morschhauser, A. (2021). The Geomagnetic Kp index and Derived Indices of Geomagnetic Activity. *Space Weather*, 19(5), e2020SW002641. <https://doi.org/10.1029/2020sw002641>
- Mikhailov, A. V., & Mikhailov, V. V. (1995). A new ionospheric index MF2. *Advances in Space Research*, 15(2), 93–97. [https://doi.org/10.1016/s0273-1177\(99\)80029-5](https://doi.org/10.1016/s0273-1177(99)80029-5)
- Minnis, C., & Bazzard, G. (1960). A monthly ionospheric index of solar activity based on F2-layer ionisation at eleven stations. *Journal of Atmospheric and Terrestrial Physics*, 18(4), 297–305. [https://doi.org/10.1016/0021-9169\(60\)90113-6](https://doi.org/10.1016/0021-9169(60)90113-6)
- Nishioka, M., Tsugawa, T., Jin, H., & Ishii, M. (2017). A new ionospheric storm scale based on TEC and foF2 statistics. *Space Weather*, 15(1), 228–239. <https://doi.org/10.1002/2016sw001536>
- Noll, C. E. (2010). The crustal dynamics data information system: A resource to support scientific analysis using space geodesy. *Advances in Space Research*, 45(12), 1421–1440. <https://doi.org/10.1016/j.asr.2010.01.018>
- Orús, R., Hernández-Pajares, M., Juan, J., & Sanz, J. (2005). Improvement of global ionospheric VTEC maps by using kriging interpolation technique. *Journal of Atmospheric and Solar-Terrestrial Physics*, 67(16), 1598–1609. <https://doi.org/10.1016/j.jastp.2005.07.017>
- Perrone, L., & De Franceschi, G. (1998). Solar, ionospheric and geomagnetic indices. *Annals of Geophysics*, 41(5–6), 843–855. <https://doi.org/10.4401/ag-3824>
- Roma-Dollase, D., Hernández-Pajares, M., Krankowski, A., Kotulak, K., Ghoddousi-Fard, R., Yuan, Y., et al. (2018). Consistency of seven different GNSS global ionospheric mapping techniques during one solar cycle. *Journal of Geodesy*, 92, 691–706. <https://doi.org/10.1007/s00190-017-1088-9>
- Schaer, S., Beutler, G., Rothacher, M., & Springer, T. A. (1996). Daily global ionosphere maps based on GPS carrier phase data routinely produced by the CODE Analysis Center. In *Proceedings of the IGS AC workshop*, Silver Spring, USA, 181–192.
- Schaer, S., Gurtner, W., & Feltens, J. (1998). IONEX: the ionosphere map exchange format version 1. In: *Proceedings of the IGS AC workshop, Germany*, 9.
- Schmölter, E., Berdermann, J., & Codrescu, M. (2021). The delayed ionospheric response to the 27-day solar rotation period analyzed with GOLD and IGS TEC data. *Journal of Geophysical Research: Space Physics*, 126(2), e2020JA028861. <https://doi.org/10.1029/2020ja028861>

- Schreiber, H. (1998). On the periodic variations of geomagnetic activity indices Ap and ap. *Annales Geophysicae*, 16(5), 510–517. <https://doi.org/10.1007/s00585-998-0510-2>
- Sori, T., Shinbori, A., Otsuka, Y., Tsugawa, T., & Nishioka, M. (2019). Characteristics of GNSS total electron content enhancements over the midlatitudes during a geomagnetic storm on 7 and 8 November 2004. *Journal of Geophysical Research: Space Physics*, 124(12), 10376–10394. <https://doi.org/10.1029/2019ja026713>
- Sulaiman, S., Ali, M. A. M., & Yatim, B. (2007). Ionospheric GPS-TEC during the 2004 major storm events at Scott Base station Antarctica. In *2007 IEEE International conference on Telecommunications and Malaysia International conference on Communications* (pp. 289–293). <https://ieeexplore.ieee.org/document/4448648>
- World Data Center for Geomagnetism, Kyoto, Nose, M., Iyemori, T., Sugiura, M., Kamei, T. et al. (2015). *Geomagnetic Dst index*. <https://doi.org/10.17593/14515-74000>
- Yang, H., Monte-Moreno, E., Hernández-Pajares, M., & Roma-Dollase, D. (2021). Real-time interpolation of global ionospheric maps by means of sparse representation. *Journal of Geodesy*, 95, 71. <https://doi.org/10.1007/s00190-021-01525-5>
- Zhang, H., Xu, P., Han, W., Ge, M., & Shi, C. (2013). Eliminating negative VTEC in global ionosphere maps using inequality-constrained least squares. *Advances in Space Research*, 51(6), 988–1000. <https://doi.org/10.1016/j.asr.2012.06.026>





# Bibliography

- Angrisano, A., Gaglione, S., Gioia, C., Massaro, M., and Troisi, S. (2013). Benefit of the NeQuick Galileo Version in GNSS Single-Point Positioning. *International Journal of Navigation & Observation*.
- Bent, R. B., Llewellyn, S. K., Nesterczuk, G., and Schmid, P. E. (1975). The development of a highly-successful worldwide empirical ionospheric model and its use in certain aspects of space communications and worldwide total electron content investigations. *Effect of the ionosphere on space systems and communications*, pages 13–28.
- Buonsanto, M. J. (1999). Ionospheric storms—A review. *Space Science Reviews*, 88(3):563–601.
- Caissy, M., Agrotis, L., Weber, G., Hernandez-Pajares, M., and Hugentobler, U. (2012). Innovation: Coming Soon-The International GNSS Real-Time Service. last access: March 21 2021.
- Ciraolo, L., Azpilicueta, F., Brunini, C., Meza, A., and Radicella, S. (2007). Calibration errors on experimental slant total electron content (TEC) determined with GPS. *Journal of Geodesy*, 81(2):111–120.
- Demyanov, V. and Yasyukevich, Y. V. (2021). Space weather: risk factors for Global Navigation Satellite Systems. *Solar-Terrestrial Physics*, 7(2):28–47.
- Dow, J. M., Neilan, R., and Rizos, C. (2009). The international GNSS service in a changing landscape of global navigation satellite systems. *Journal of Geodesy*, 83(3-4):191–198.
- Elsobeiey, M. and Al-Harbi, S. (2016). Performance of real-time Precise Point Positioning using IGS real-time service. *GPS solutions*, 20(3):565–571.
- ESA Commons (2021). Space weather effects.
- Feltens, J. (2007). Development of a new three-dimensional mathematical ionosphere model at European Space Agency/European Space Operations Centre. *Space Weather*, 5(12).
- Ghoddousi-Fard, R. (2014). GPS ionospheric mapping at Natural Resources Canada. In *IGS workshop, Pasadena*.
- Hernández-Pajares, M., Aragón-Ángel, A., Defraigne, P., Bergeot, N., Prieto-Cerdeira, R., and García-Rigo, A. (2014). Distribution and mitigation of higher-order ionospheric effects on precise GNSS processing. *Journal of Geophysical Research: Solid Earth*, 119(4):3823–3837.

- Hernández-Pajares, M. et al. (2010). Section 9.4 Ionospheric model for radio techniques of Chapter 9 Models for atmospheric propagation delays of IERS Conventions 2010. *IERS Technical Note*, (36).
- Hernández-Pajares, M., García-Rigo, A., Juan, J. M., Sanz, J., Monte, E., and Aragón-Àngel, A. (2012). GNSS measurement of EUV photons flux rate during strong and mid solar flares. *Space Weather*, 10(12).
- Hernández-Pajares, M., Juan, J., and Sanz, J. (1997). Neural network modeling of the ionospheric electron content at global scale using GPS data. *Radio Science*, 32(3):1081–1089.
- Hernández-Pajares, M., Juan, J., and Sanz, J. (1999). New approaches in global ionospheric determination using ground GPS data. *Journal of Atmospheric and Solar-Terrestrial Physics*, 61(16):1237–1247.
- Hernández-Pajares, M., Juan, J., and Sanz, J. (2006). Medium-scale traveling ionospheric disturbances affecting GPS measurements: Spatial and temporal analysis. *Journal of Geophysical Research: Space Physics*, 111(A7).
- Hernández-Pajares, M., Juan, J., Sanz, J., Orus, R., García-Rigo, A., Feltens, J., Komjathy, A., Schaer, S., and Krankowski, A. (2009). The IGS VTEC maps: a reliable source of ionospheric information since 1998. *Journal of Geodesy*, 83(3-4):263–275.
- Hernández-Pajares, M., Juan, J., Sanz, J., and Sole, J. (1998). Global observation of the ionospheric electronic response to solar events using ground and LEO GPS data. *Journal of Geophysical Research: Space Physics*, 103(A9):20789–20796.
- Hernández-Pajares, M., Juan, J. M., Sanz, J., Aragón-Àngel, À., García-Rigo, A., Salazar, D., and Escudero, M. (2011). The ionosphere: effects, GPS modeling and the benefits for space geodetic techniques. *Journal of Geodesy*, 85(12):887–907.
- Hernández-Pajares, M., Lyu, H., Aragón-Àngel, À., Monte-Moreno, E., Liu, J., An, J., and Jiang, H. (2020). Polar Electron Content From GPS Data-Based Global Ionospheric Maps: Assessment, Case Studies, and Climatology. *Journal of Geophysical Research: Space Physics*, 125(6):e2019JA027677.
- Hernández-Pajares, M., Roma-Dollase, D., Krankowski, A., García-Rigo, A., and Orús-Pérez, R. (2017a). Methodology and consistency of slant and vertical assessments for ionospheric electron content models. *Journal of Geodesy*, 91(12):1405–1414.
- Hernández-Pajares, M., Roma-Dollase, D., Krankowski, A., García-Rigo, A., and Orús-Pérez, R. (2017b). Methodology and consistency of slant and vertical assessments for ionospheric electron content models. *Journal of Geodesy*, (doi:10.1007/s00190-017-1032-z):1–10.
- Hu, L., Yue, X., and Ning, B. (2017). Development of the beidou ionospheric observation network in china for space weather monitoring. *Space Weather*, 15(8):974–984.
- Jakowski, N. and Hoque, M. M. (2019). Estimation of spatial gradients and temporal variations of the total electron content using ground-based GNSS measurements. *Space Weather*, 17(2):339–356.

- Kivelson, A. (1995). *Introduction to space physics*. Cambridge university press.
- Klobuchar, J. A. (1987). Ionospheric time-delay algorithm for single-frequency GPS users. *IEEE Transactions on aerospace and electronic systems*, (3):325–331.
- Komjathy, A., Sparks, L., Wilson, B. D., and Mannucci, A. J. (2005). Automated daily processing of more than 1000 ground-based GPS receivers for studying intense ionospheric storms. *Radio Science*, 40(6).
- Li, Z., Wang, N., Hernández-Pajares, M., Yuan, Y., Krankowski, A., Liu, A., Zha, J., García-Rigo, A., Roma-Dollase, D., Yang, H., et al. (2020). IGS real-time service for global ionospheric total electron content modeling. *Journal of Geodesy*, 94(3):1–16.
- Li, Z., Yuan, Y., Wang, N., Hernandez-Pajares, M., and Huo, X. (2015). SHPTS: towards a new method for generating precise global ionospheric TEC map based on spherical harmonic and generalized trigonometric series functions. *Journal of Geodesy*, 89(4):331–345.
- Liu, Q., Hernández-Pajares, M., Lyu, H., and Goss, A. (2021a). Influence of temporal resolution on the performance of global ionospheric maps. *Journal of Geodesy*, 95(34):34.
- Liu, Q., Hernández-Pajares, M., Lyu, H., Nishioka, M., Yang, H., Monte-Moreno, E., Gulyaeva, T., Béniguel, Y., Wilken, V., Olivares-Pulido, G., and Raúl, O.-P. (2021b). Ionospheric Storm Scale Index Based on High Time Resolution UPC-IonSAT Global Ionospheric Maps (IsUG). *Space Weather*, 19(11):e2021SW002853.
- Liu, Q., Hernández-Pajares, M., Yang, H., Monte-Moreno, E., García-Rigo, A., Lyu, H., Olivares-Pulido, G., and Raúl, O.-P. (2022). A new way of estimating the spatial and temporal components of the Vertical Total Electron Content gradient based on UPC-IonSAT Global Ionosphere Maps. *Space Weather*, 20(2):e2021SW002926.
- Liu, Q., Hernández-Pajares, M., Yang, H., Monte-Moreno, E., Roma-Dollase, D., García-Rigo, A., Li, Z., Wang, N., Laurichesse, D., Blot, A., Zhao, Q., Zhang, Q., Hauschild, A., Agrotis, L., Schmitz, M., Wübbena, G., Stürze, A., Krankowski, A., Schaer, S., Feltens, J., Komjathy, A., and Ghoddousi-Fard, R. (2021c). The cooperative IGS RT-GIMs: a reliable estimation of the global ionospheric electron content distribution in real time. *Earth System Science Data*, 13(9):4567–4582.
- Liu, T., Zhang, B., Yuan, Y., and Li, M. (2018). Real-time precise point positioning (rtppp) with raw observations and its application in real-time regional ionospheric vtec modeling. *Journal of Geodesy*, 92(11):1267–1283.
- Mannucci, A., Wilson, B., Yuan, D., Ho, C., Lindqwister, U., and Runge, T. (1998). A Global mapping technique for GPS-derived ionospheric total electron content measurements. *Radio science*, 33(3):565–582.
- Maruyama, T. (2006). Extreme enhancement in total electron content after sunset on 8 November 2004 and its connection with storm enhanced density. *Geophysical research letters*, 33(20).

- Maruyama, T., Ma, G., and Tsugawa, T. (2013). Storm-induced plasma stream in the low-latitude to midlatitude ionosphere. *Journal of Geophysical Research: Space Physics*, 118(9):5931–5941.
- Monte Moreno, E., García Rigo, A., Hernández-Pajares, M., and Yang, H. (2018). TEC forecasting based on manifold trajectories. *Remote Sensing*, 10(7):988.
- Monte-Moreno, E. and Hernández-Pajares, M. (2014). Occurrence of solar flares viewed with GPS: Statistics and fractal nature. *Journal of Geophysical Research: Space Physics*, 119(11):9216–9227.
- Monte-Moreno, E., Hernandez-Pajares, M., Lyu, H., Yang, H., and Aragon-Angel, A. (2021). Estimation of Polar Depletion Regions by VTEC Contrast and Watershed Enhancing. *IEEE Transactions on Geoscience and Remote Sensing*.
- Montenbruck, O. and Rodríguez, B. G. (2020). NeQuick-G performance assessment for space applications. *GPS Solutions*, 24(1):1–12.
- Montenbruck, O., Steigenberger, P., Prange, L., Deng, Z., Zhao, Q., Perosanz, F., Romero, I., Noll, C., Stürze, A., Weber, G., et al. (2017). The Multi-GNSS Experiment (MGEX) of the International GNSS Service (IGS)—achievements, prospects and challenges. *Advances in space research*, 59(7):1671–1697.
- Nishioka, M., Tsugawa, T., Jin, H., and Ishii, M. (2017). A new ionospheric storm scale based on TEC and foF2 statistics. *Space Weather*, 15(1):228–239.
- NovAtel Commons (2021). GNSS segments.
- Orús, R., Hernández-Pajares, M., Juan, J., and Sanz, J. (2005). Improvement of global ionospheric VTEC maps by using kriging interpolation technique. *Journal of Atmospheric and Solar-Terrestrial Physics*, 67(16):1598–1609.
- Orús, R., Hernández-Pajares, M., Juan, J., Sanz, J., and García-Fernández, M. (2002). Performance of different TEC models to provide GPS ionospheric corrections. *Journal of Atmospheric and Solar-Terrestrial Physics*, 64(18):2055–2062.
- Perez, R. O., Parro-Jimenez, J., and Prieto-Cerdeira, R. (2018). Status of NeQuick G after the solar maximum of cycle 24. *Radio Science*, 53(3):257–268.
- Pi, X., Mannucci, A., Lindqwister, U., and Ho, C. (1997). Monitoring of global ionospheric irregularities using the worldwide GPS network. *Geophysical Research Letters*, 24(18):2283–2286.
- Prieto-Cerdeira, R., Orús-Pérez, R., Breeuwer, E., Lucas-Rodríguez, R., and Falcone, M. (2014). Performance of the Galileo single-frequency ionospheric correction during in-orbit validation. *GPS world*, 25(6):53–58.
- Rawer, K., Bilitza, D., and Ramakrishnan, S. (1978). Goals and status of the International Reference Ionosphere. *Reviews of geophysics*, 16(2):177–181.

- Roma-Dollase, D., Hernández-Pajares, M., García Rigo, A., Krankowski, A., Fron, A., Laurichesse, D., Blot, A., Orús-Pérez, R., Yuan, Y., Li, Z., Wang, N., Schmidt, M., and Erdogan, E. (2018a). Looking for optimal ways to combine global ionospheric maps in real-time. In *IGS workshop 2018, Oct 29-Nov2, Wuhan*.
- Roma-Dollase, D., Hernández-Pajares, M., Krankowski, A., Kotulak, K., Ghoddousi-Fard, R., Yuan, Y., Li, Z., Zhang, H., Shi, C., Wang, C., Feltens, J., Vergados, P., Komjathy, A., Schaer, S., García-Rigo, A., and Gómez-Cama, J. M. (2018b). Consistency of seven different GNSS global ionospheric mapping techniques during one solar cycle. *Journal of Geodesy*, 92(6):691–706.
- Sato, H., Jakowski, N., Berdermann, J., Jiricka, K., Heßelbarth, A., Banyś, D., and Wilken, V. (2019). Solar radio burst events on 6 September 2017 and its impact on GNSS Signal Frequencies. *Space Weather*, 17(6):816–826.
- Schaer, S. (1999). *Mapping and predicting the earths ionosphere using the Global Positioning System. 1999. 205p*. PhD thesis, Ph. D. dissertation. University of Bern, Bern, Switzerland.
- Schaer, S., Beutler, G., Rothacher, M., and Springer, T. A. (1996). Daily global ionosphere maps based on GPS carrier phase data routinely produced by the CODE Analysis Center. In *Proceedings of the IGS AC Workshop, Silver Spring, MD, USA*, pages 181–192.
- Schaer, S., Gurtner, W., and Feltens, J. (1998). IONEX: The ionosphere map exchange format version 1.
- Schwenn, R. (2006). Space weather: The solar perspective. *Living Reviews in Solar Physics*, 3(1):1–72.
- Sori, T., Shinbori, A., Otsuka, Y., Tsugawa, T., and Nishioka, M. (2019). Characteristics of GNSS Total Electron Content Enhancements Over the Midlatitudes During a Geomagnetic Storm on 7 and 8 November 2004. *Journal of Geophysical Research: Space Physics*, 124(12):10376–10394.
- Sulaiman, S., Ali, M. A. M., and Yatim, B. (2007). Ionospheric GPS-TEC during the 2004 major storm events at Scott Base station Antarctica. In *2007 IEEE International Conference on Telecommunications and Malaysia International Conference on Communications*, pages 289–293. IEEE.
- Teunissen, P. and Montenbruck, O. (2017). *Springer Handbook of Global Navigation Satellite Systems*. Springer.
- Wang, N., Li, Z., Li, M., Yuan, Y., and Huo, X. (2018). GPS, BDS and Galileo ionospheric correction models: An evaluation in range delay and position domain. *Journal of Atmospheric and Solar-Terrestrial Physics*, 170:83–91.
- Wang, N., Li, Z., Yuan, Y., and Huo, X. (2021). BeiDou Global Ionospheric delay correction Model (BDGIM): performance analysis during different levels of solar conditions. *GPS Solutions*, 25(3):1–13.
- Wang, N., Yuan, Y., Li, Z., Li, Y., Huo, X., and Li, M. (2017). An examination of the Galileo NeQuick model: comparison with GPS and JASON TEC. *GPS solutions*, 21(2):605–615.

- Wikimedia Commons (2021). Comparison of satellite navigation orbits.
- Xiong, B., Wan, W., Yu, Y., and Hu, L. (2016). Investigation of ionospheric tec over china based on gnss data. *Advances in Space Research*, 58(6):867–877.
- Yang, H., Monte-Moreno, E., Hernández-Pajares, M., and Roma-Dollase, D. (2021). Real-time interpolation of global ionospheric maps by means of sparse representation. *Journal of Geodesy*, 95(6):1–20.
- Yang, Y., Mao, Y., and Sun, B. (2020). Basic performance and future developments of BeiDou global navigation satellite system. *Satellite Navigation*, 1(1):1–8.
- Yuan, Y. and Ou, J. (2004). A generalized trigonometric series function model for determining ionospheric delay. *Progress in Natural Science*, 14(11):1010–1014.
- Yuan, Y., Wang, N., Li, Z., and Huo, X. (2019). The BeiDou global broadcast ionospheric delay correction model (BDGIM) and its preliminary performance evaluation results. *NAVIGATION, Journal of the Institute of Navigation*, 66(1):55–69.
- Zhang, B., Ou, J., Yuan, Y., and Li, Z. (2012). Extraction of line-of-sight ionospheric observables from gps data using precise point positioning. *Science China Earth Sciences*, 55(11):1919–1928.
- Zhang, B., Teunissen, P. J., Yuan, Y., Zhang, X., and Li, M. (2019). A modified carrier-to-code leveling method for retrieving ionospheric observables and detecting short-term temporal variability of receiver differential code biases. *Journal of Geodesy*, 93(1):19–28.
- Zhang, H., Xu, P., Han, W., Ge, M., and Shi, C. (2013). Eliminating negative VTEC in global ionosphere maps using inequality-constrained least squares. *Advances in Space Research*, 51(6):988–1000.
- Zhang, Q. and Zhao, Q. (2019). Analysis of the data processing strategies of spherical harmonic expansion model on global ionosphere mapping for moderate solar activity. *Advances in Space Research*, 63(3):1214–1226.